Lift Generation in Soft Porous Media

From Red Cells to Skiing to a New Concept for a Train Track

by

Qianhong Wu

A dissertation submitted to the Faculty in Engineering in partial

fulfillment of the requirements for the degree of Doctor of Philosophy,

The City University of New York

2005

INFORMATION TO USERS

The quality of this reproduction is dependent upon the quality of the copy submitted. Broken or indistinct print, colored or poor quality illustrations and photographs, print bleed-through, substandard margins, and improper alignment can adversely affect reproduction.

In the unlikely event that the author did not send a complete manuscript and there are missing pages, these will be noted. Also, if unauthorized copyright material had to be removed, a note will indicate the deletion.

ProQuest Information and Learning Company
300 North Zeeb Road
P.O. Box 1346
Ann Arbor, MI 48106-1346

This manuscript has been read and accepted for the Graduate Faculty in Engineering in satisfaction of the dissertation requirements for the degree of Doctor of Philosophy.

4/25/05
Date

Professor Sheldon Weinbaum
Chair of Examining Committee

4/25/2005
Date

Professor Mumtaz K. Kassir
Executive Officer

Professor Yiannis Andreopoulos

Professor Latif M. Jiji

Professor John M. Tarbell

Professor Mary R. Albert
Supervisory Committee

The City University of New York

Abstract

LIFT GENERATION IN POROUS MEDIA

FROM RED CELLS TO SKIING TO A NEW CONCEPT FOR A TRAIN TRACK

by

Qianhong Wu

Mentor: Professor Sheldon Weinbaum, Co-mentor: Professor Yiannis Andreopoulos

In a recent paper, Feng and Weinbaum (2000) showed that there is a remarkable dynamic similarity between a red cell gliding on the endothelial surface layer (ESL) that lines our microvessels and a human snowboarding on fresh powder although they differ in mass by 10^{15}. One is able to produce lift forces in each case that are several orders of magnitude greater than classical lubrication theory. In the case of the red cell, Weinbaum et al. (2003) also predicted that the normal force required to compress the core proteins in the ESL is much less than the lift force due to the fluid draining pressure. Frictional drag which is proportional to this force is dramatically reduced.

Herein we shall first present non-linear exact and asymptotic solutions to a Navier-Stokes equation of Brinkman type for a stagnation point flow in a porous medium. The solutions for the two dimensional case are applied to describe the flow in the transverse plane of a ski or snowboard. We then report the first experimental and theoretical study of the pore pressures generated in snow on the time scale of skiing or snowboarding. Using a novel porous cylinder-piston apparatus, we have measured the excess pore pressure that would build up beneath the piston surface and have also measured its subsequent decay due to the venting of the air from the snow at the porous walls of the cylinder. A theoretical model for this pressure relaxation process is then developed using a consolidation theory, which shows good agreement with the experimental data. Based on these studies, we further extend Feng and

Weinbaum theory to a more realistic theoretical model to describe the lift mechanics of downhill skiing or snowboarding. And finally, we employ the concepts deduced from the motion of red cells in capillaries and human skiing or snowboarding to the design of a prototype high speed train track which can support gliding vehicles weighing 50 or more metric tons with extremely low sliding friction. The permeability and elastic properties of this train track are similar to goose down.

Acknowledgements

I would like to express my deepest gratitude to my advisors, Professor Sheldon Weinbaum and Professor Yiannis Andreopoulos for their continuous support, suggestion and encouragement. Before joining CCNY in 1999, I never expected that one day I would enjoy academic research so much. It is Professor Weinbaum, who actually inspired me with his various creative ideas and incisive physical insights. I especially want to thank my advisors for training me comprehensively not only in research, but also in other crucial aspects of academic activities such as writing, proposal preparation, research mentoring and teaching. Due to the novelty of the ideas, we had some difficulties in the beginning with getting our papers published and our proposals approved. Dr. Weinbaum's and Dr. Andreopoulos' support and encouragement really made this work possible.

I am indebted to a large number of people for their assistance in the preparation of this dissertation. Among them are Professor Latif M. Jiji, Professor Jonh M. Tarbell, Professor Mary R. Albert, Professor Stephen C. Cowin and Professor Peter Ganatos for their constructive suggestions on the present study. I would like to thank Dr. Savvas Xanthos, Mr. Mingwei Gong and Mr. Shiyun Xu for their great help in the experiments, Dr. Peng Guo and Mr. Yuefeng Han for very helpful discussions; Ms. Ping Zhao and Mr. Kai Gu for their kind help in the graph preparation; and my colleagues at the City College of New York for providing me with an excellent environment which allows me to do research efficiently. I also want to thank Ms. Yesim Igci and other undergraduate and high school students who worked with me over the past three years.

Financial support from the National Institutes of Health and the Mario Capelloni Dissertation Fellowship are acknowledged.

I am especially grateful to my beloved mother, Xianer Ma, father, Jiantao Wu, and my sisters Lizhu and Lingzhu in China, for their unconditional love and support. It is hard to express in words my deep appreciation to my parents and how I miss my mother at this exciting moment in my life.

I dedicate this research to my parents and to the memory of my mother.

Table of Contents

List of Tables

List of Figures

Chapter 1 Introduction

In a recent study, Feng and Weinbaum (2000), hereafter referred to as F&W, laid the foundation for a new type of lubrication theory that is applicable for porous media whose structure is so compressible that the normal forces generated by the elastic compression of the matrix are negligible compared to the pressure forces generated within the porous layer. This new theory shows that there is an unexpected and remarkable dynamic similarity between the motion of a red cell gliding at < 20 μm/s on a compressed endothelial surface layer (ESL) of sulfated proteoglycans and glycoproteins that line the endothelial cells (EC) of our capillaries and a human skier or snowboarder skiing on soft snow powder even though their difference in mass is of order 10^{15}. At velocities > 20 μm/s the red blood cell rises out of the ESL and there is an intervening thin fluid lubricating layer between the ESL and the RBC membrane. F&W predict that the excess pore pressure generated by a planing surface moving on any compressible porous media scales as $\alpha^2 = h^2/K$, where h is the layer thickness and K is the Darcy permeability; and α is of order 10^2 or larger for both red blood cells gliding on the ESL and humans skiing. Thus, the lift forces generated can be four or more orders of magnitude greater than classical lubrication theory. The huge enhancement in the lift arises from the fact that as the matrix compresses there is a dramatic increase in the lubrication pressure because of the marked increase in the hydraulic resistance that the fluid encounters as it tries to escape from the confining boundaries through the thin compressed porous layer.

In a more recent paper, Weinbaum *et al.* (2003), provide an overview of the various roles of the endothelial surface layer in the microcirculation from a new perspective. Based on the quasi-periodic ultrastructural model proposed in Squire *et al.* (2001), Weinbaum *et al.* show that the flexural rigidity EI of the core proteins in the

bush-like structures comprising the endothelial glycocalyx is sufficiently stiff for these structures to serve as a molecular sieve and a mechanical transducer of fluid shearing stresses. On the other hand, they show that the buckling forces for the core proteins are one to two orders of magnitude smaller than the hydraulic forces generated during the arrest of motion of red blood cells. When the red cell velocity is < 20 μm/s, the sliding friction between the red cell membrane and the endothelial glycocalyx, is proportional to the normal force applied on the solid phase, and, therefore, is greatly reduced.

In the present study, we shall first extend F&W theory by examining the inertia of the escaping air at the lateral edges of a ski or snowboard. A generalized stagnation point flow in a porous medium is studied which provides an approximate model to analyze the effect of air inertia in the cross-sectional plane of ski or snowboard. We then develop a novel experimental and theoretical approach to examine the dynamic lift forces that are generated while compacting both wind packed and fresh snow powder. To our knowledge this is the first investigation of the dynamic properties of snow on the time scale of importance in skiing or snowboarding. Based on these studies, we propose a simplified model to describe the lift mechanics of downhill skiing or snowboarding which treats the relative contributions of both the transiently trapped air and the ice crystal (solid) phase. Finally, we apply the lesson learned from red cell motion in a capillary and human skiing on a compressed snow powder to the design of a high speed vehicle which could ride on a track made of highly compressible porous media. Since the normal force from the solid phase is small one would expect relatively little friction between the gliding surfaces.

1.1 Biological Background

Since the fundamental insights of this study are the outgrowth of the recent discoveries concerning the roles of the endothelial surface layer or glycocalyx in the microcirculation, I shall briefly describe this background.

The endothelial glycocalyx is a negatively charged layer of proteoglycans, glycoproteins and glycosaminoglycans (GAG) that coats the surface of all microvessels, Henry and Duling (1999). This layer has been estimated to vary from 0.1 μm in *in vitro* studies of frog mesentery microvessels, Adamson and Clough (1992), to 0.4 to 0.5 μm in *in vivo* studies of hamster cremaster microvessels, Vink and Duling (1996). Figure 1.1 shows the surface glycocalyx coating the interior surface of a capillary in which the functional diameter of the capillary is significantly reduced by this surface matrix. Squire *et al.* (2001) proposed a quasi-periodic ultrastructural model for the 3D organization of the endothelial surface layer and its linkage to the submembranous cortical cytoskeleton. A schematic of this model is shown in Weinbaum *et al.* (2003), see Figure 1.2, where the bush-like structure of the glycocalyx with its 20nm bi-directional periodicity for the core proteins and 100nm periodicity for the spacing of the core protein clusters is presented. The latter structure is connected to the cortical actin cytoskeleton beneath the endothelial cell membrane.

While the existence of a surface glycocalyx was first identified nearly forty years ago, Luft (1966), its crucial functions have been realized just recently. These are:

(1) A molecular sieve for plasma proteins:

Michel (1997) and Weinbaum (1998) have proposed that the GAG sidechains in this fiber matrix constitute the primary molecular sieve that determines the colloidal osmotic pressure that is felt across the capillary wall. In Hu and Weinbaum (1999) a new microstructural model and interpretation of the classical Starling

equation (1896) for water movement across capillaries is presented. The new model predicts the driving forces for water exchange are the hydrostatic and oncotic pressure differences across the thin surface glycocalyx rather than the global difference in these pressures between plasma and tissue, as had universally been believed for over a century. This prediction is clearly verified by the experiments in Hu et al. (2000) for frog microvessls and Adamson et al. (2004) for rat microvessels in which the tissue is back loaded with albumin at the same concentration as the lumen. These experiments demonstrate that at high filtration rates the proteins on the lumen side of the tight junction (TJ) strand are washed out and nearly the full oncotic pressure $\sigma_f \pi_L$ is felt across the ESL in the case of frog microvessels, and ~70 percent of $\sigma_f \pi_L$ in the case of rat microvessels, although the tissue oncotic pressure is isotonic with respect to the luminal oncotic pressure. The *in vitro* study of Starling's hypothesis in a cultured monolayer of bovine aortic endothelial cells (Pang and Tarbell, 2003) also supports the studies in capillaries showing transient reabsorption that decays to steady-state filtration at longer times.

(2) A highly compressible porous hydrodynamic interface in the motion of red and white cells in capillaries:

The surface glycocalyx provides a protective lubricating layer which prevents adhesive molecular interaction between proteins in the red cell membrane and their ligands in the plasmalemma membrane of the endothelial cell. The 8μm red cell is able to survive 10^5 passages through the microcirculation during a typical lifetime of 120 days. This highly flexible cell is able to deform and squeeze through capillaries which are 5 to 6 μm diameter without rupturing either the membranes of the endothelial cells or its own plasmalemma. A remarkable feature of this longevity is that the red cell can travel at velocities that approach 100 times its diameter a second

and pass at much lower velocities through muscular sphincters of a few μm diameter at the entrance to arterioles where opposing membranes would touch were it not for the huge repulsive forces predicted in F&W. In contrast, an expert downhill skier moves at velocity which is about ten times his or her height per second due to gravitational forcing. In this context the red cell is perhaps the world's most efficient skier.

From a structural standpoint the endothelial glycocalyx is a remarkable resilient fibrous material. When a red cell starts from rest it exhibits a striking pop out phenomenon. At rest the bending moments in the red cell's membrane cytoskeleton are sufficient to fully crush the glycocalyx, much like a skier standing in fresh powder. As the red cell picks up speed it rises through the glycocalyx and at velocities in excess of 20 μm/s it rises out of the glycocalyx and approaches an equilibrium position which is 0.1~0.2 μm above the edge of the glycocalyx whose outer border in Vink and Duling (1996) is indicated by the edge of a fluorescent FITC dextran layer. In contrast to snow, the glycocalyx appears to be completely resilient and returns to its equilibrium position in a fraction of a second after the passage of the cell. This restoration is due to a finite bending rigidity of the core proteins of the endothelial glycocalyx. In Weinbaum et al (2003), the flexural rigidity EI of the vertical fibers has been determined by an approximate viscoelastic model.

The theory in F&W predicts rather remarkably that the value of the permeability parameter α for a red cell is of the order of 100, the same order as for a human skier whose mass is 10^{15} times larger, and that the repulsive pressures generated within the glycocalyx are four orders of magnitude greater than predicted by classical lubrication theory. These repulsive forces we now believe are the secret to the long life of the red cell since it prevents the adhesive interactions that would lead

to red cell hemolysis. When the motion of red cells is arrested, Weinbaum *et al.* (2003) predict that the hydraulic force due to the draining of fluid trapped in the endothelial surface layer is at least 20 times greater than the elastic restoring forces exerted by the core proteins and, in addition, the draining time is extended greatly by the decrease in Darcy permeability of the surface matrix due to its compression. This is an additional safety factor preventing the adhesive interaction in the opposing membranes.

Zhao *et al.* (2001) proposed that a white blood cell can tip-toe across the endothelial surface layer just like a Jesus Christ lizard can run across water. The secret is that the major resistance to microvilli tip penetration arises from the viscous resistance of the glycocalyx, instead of the buckling force from core proteins, since the latter is weak in supporting normal compression.

(3) Mechanotransduction

The other vital function of the surface glycocalyx is to provide a mechanotransduction mechanism via which fluid shear stresses can be communicated to the cortical cytoskeleton of the cell in initiating intracellular signaling, as proposed by Weinbaum *et al.* (2003). Although the shear stress at the edge of the endothelial surface layer is greatly attenuated by the matrix, the bending moment applied at the tip of the core proteins is transmitted with little attenuation to the cortical cytoskeleton beneath the membrane due to the finite flexural rigidity of the core proteins. Furthermore, the bending arm provided by the core proteins leads to an amplification of the stress acting on the actin cortical scaffold and increases their deformation. Thi *et al.* (2004) performed a series of experiments to test this hypothesis and see if the glycocalyx layer was directly involved in the reorganization of the actin cortical cytoskeleton and the redistribution of various linker proteins in response to fluid shear. Rat fat-pad endothelial cells were exposed to fluid shear stress with an intact or

compromised ESL. They observed that a fluid shear stress of 10 dyn/cm^2 with a duration of 5 h disrupts the dense peripheral actin bands (DPABs) and promotes migration of vinculin to cell borders in the case of endothelial cells with an intact glycocalyx. In marked contrast, such reorganization was completely abolished when the ESL was compromised. The glycocalyx core protein fibers were also shown to amplify the effect of fluid shear stress and produce a sufficient disjoining force on the adherens junction to unzipper the VE-caderins bonds and initiate a disruption of the DPABs. This behavior is explained in the terms of a 'bumper car'model proposed in Thi *et al.* (2004).

1.2 Organization of the thesis

In the present study, we would like to apply the lessons learned from the red cell motion in a capillary to develop an experimental and theoretical approach to verify and extend the lubrication theory for highly compressible porous media developed by F&W. We would also apply the ideas of lift generation in porous media to the design of a high-speed train track that can support a train weighing 50 or more metric tons with extremely low friction. The permeability and mechanical properties of this track are similar to goose down. The outline of this dissertation is as follows:

In Chapter 2, I shall present non-linear exact and asymptotic solutions to a Navier-Stokes equation of Brinkman type proposed by Joseph *et al.* (1982) for the flow in the stagnation-point laminar boundary layer on a cylinder or sphere if fibers of increasing concentration are uniformly added to a porous medium surrounding these blunt bodies. Although one can not perform a rigorous averaging of the $(\mathbf{u}\cdot\nabla)\mathbf{u}$ term, one is able to gain useful insight into the transition in behavior that occurs between the classical solutions of Hiemenz (1911) and Homann (1936) for the two-

dimensional and axisymmetric stagnation-point boundary layers and the local expansion of the Brinkman solution for the flow past a cylinder or sphere in the stagnation regions as the Darcy permeability is decreased. In this analysis, a new fundamental dimensionless parameter emerges, $\beta = \upsilon/KA$, where A is the characteristic velocity gradient $4U/D$ imposed by the external flow, υ is the kinematic viscosity and K, the Darcy permeability. β denotes the ratio of the square of two lengths, the classical boundary layer thickness for a high Reynolds number flow $D/(2\mathrm{Re}_D^{1/2})$ and the fiber-interaction layer thickness $K^{1/2}$. The exact solutions of the non-linear Brinkman equation for the stagnation-point flow presented herein show the structure of a new type of boundary layer that evolves as β varies from zero, the classical limit of the Hiemenz and Homann solutions, to $\beta >> 1$, the classical Brinkman limit where inertial effects are negligible. Using asymptotic analysis we shall show that when $\beta >> 1$ the classical boundary layer thickness decreases as $\beta^{-1/2}$. Because of the introduction of the Darcy term, the pressure field differs greatly from the classical stagnation-point flow. The pressure does not increase monotonically along the stagnation streamline, and for $\beta >> 1$ there is a pressure minimum that approaches the origin as $\beta^{-1/2}$.

In Chapter 3, a new experimental and theoretical approach is presented to examine the dynamic lift forces that are generated in the compression of both fresh snow powder and wind-packed snow. At typical skiing velocities of 10 to 30 m/s the duration of contact of a ski or snowboard with the snow will vary from 0.05 to 0.2 s depending on the length of the planing surface and its speed. No one, to our knowledge, has previously measured the dynamic behavior of snow on this short of a time scale and, thus, there are no existing measurements of the excess pore pressure that can build up in snow on this time scale. Using a novel porous cylinder-piston

apparatus, we have measured the excess pore pressure that would build up beneath the piston surface and have also measured its subsequent decay due to the venting of the air from the snow at the porous walls of the cylinder. In further experiments, in which the air is slowly and continuously drained to avoid a build up in pore pressure, we have been able to separate out the force exerted by the ice crystal phase as a function of its instantaneous deformation. A theoretical model for the pore pressure relaxation in the porous cylinder is then developed using consolidation theory. Dramatically different dynamic behavior is observed for two different snow types, one giving a steady continuous relaxation of the excess pore pressure and the other leading to a piston rebound with negative pore pressure. An intriguing new feature of the rebound is the apparent debonding of sintered ice crystals after maximum compression. This behavior is well described by introducing a debonding coefficient where the debonding force is proportional to the expansion velocity of the medium. The experimental and theoretical approach presented herein and the previous generalized lubrication theory for compressible porous media developed in F&W, have laid the foundation for understanding the detailed dynamic response of soft porous layers to rapid deformation.

In Chapter 4, a simplified mathematical model is derived to describe the lift mechanics of downhill skiing and snowboarding, where the lift contribution due to both the transiently trapped air and the compressed solid phase (snow crystals) are determined, respectively. To our knowledge, this is the first time that anyone has attempted to realistically estimate the relative contribution of the transiently trapped air to the total lift in skiing and snowboarding. The model uses Shimizu's empirical relation (1970) to predict the local variation in Darcy permeability due to the compression of the solid phase. We present numerical solutions for snowboarding and

asymptotic analytic solutions for skiing for two typical snow types, fresh and wind-packed snow for the case where there are no edging or turning maneuvers. Our model predicts that approximately 50% of the total lift force is generated by the trapped air in the case of fine-grained, wind-packed snow for snowboarding and 40% for skiing. For highly permeable fresh snow the lift contribution from the pore air pressure drops to < 20%. The forces and moments on the skier or snowboarder are used to predict the angle of the attack of the planing surface, the penetration depth at the leading edge and the shift in the center of pressure with velocity for each snow condition. This new theory is an extension of the series of studies on lift generation in highly compressible porous media developed by F&W and Wu *et al.* (2004a, 2005b).

In chapter 5, motivated by the fundamental new insights gleaned from the motion of red cells gliding on the endothelial glycocalyx of capillaries and humans skiing on fresh snow powder, we propose the design of confined planar lifting surfaces with greatly enhanced lift and no lateral leakage of pore pressure. These surfaces move on highly compressible porous media where the lift forces are six orders of magnitude greater than classical lubrication theory and the drag due to sliding friction of the solid phase is also greatly reduced. These insights are used to formulate a new concept for a high speed train track capable of supporting a 50 ton train car on a porous medium whose permeability and elastic properties closely resemble those of goose down.

In chapter 6, I shall briefly summarize the thesis and suggest future applications.

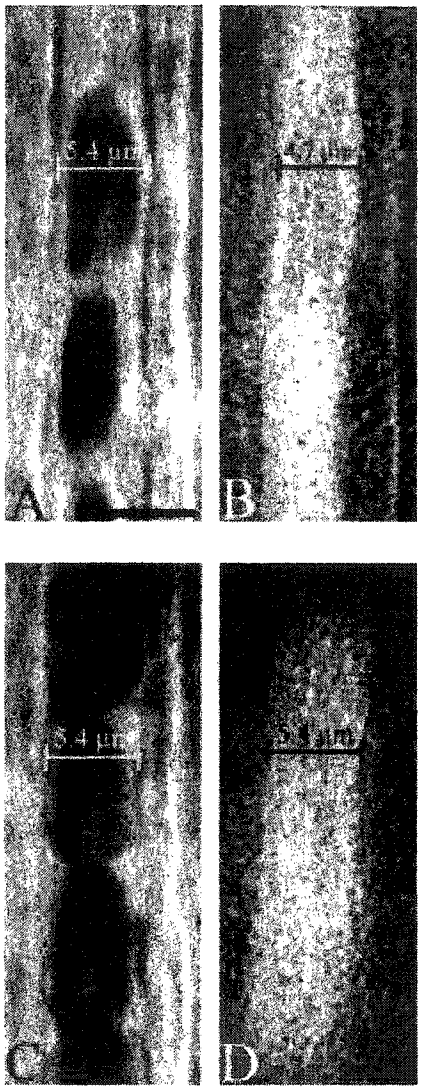

Figure 1.1 Digitized images of a capillary segment before (A and B) and after (C and D) continuous exposure to epi-illumination for 5 minutes. Before epifluorescent treatment, RBC width (A) and the width of the FITC-dextran column (B) were significantly smaller than the anatomic capillary diameter. Treatment of the capillary with epi-illumination increased the width of RBCs (C) and the FITC-dextran column (D), without a significant effect on the anatomic capillary diameter. (from Vink and Duling 1996)

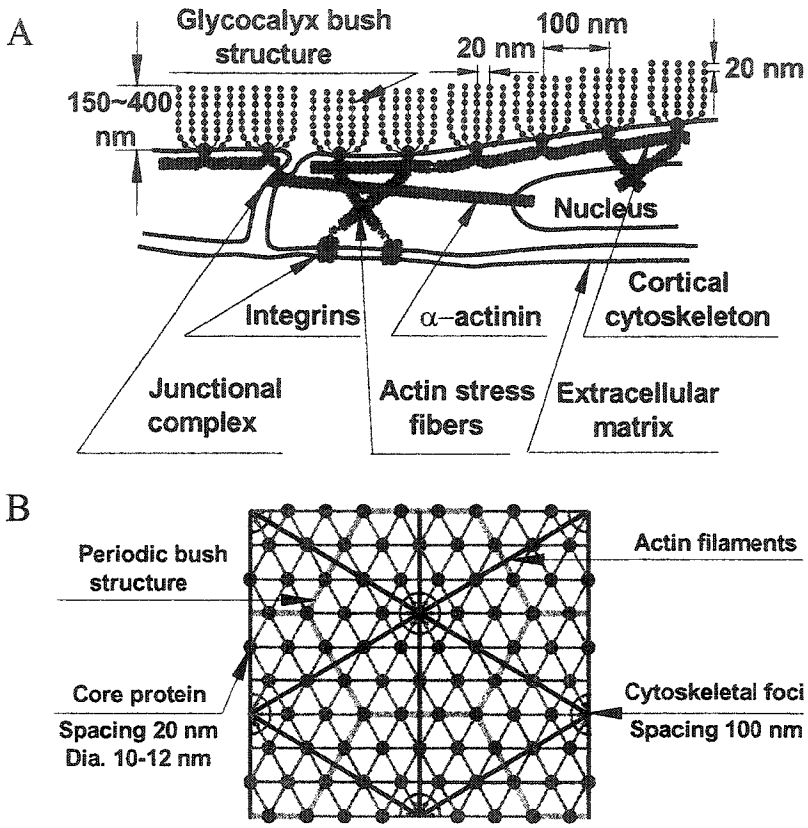

Figure 1.2 (A) Sketch of Endothelial surface glycocalyx (not to scale) showing core protein arrangement and spacing of scattering centers along core proteins and their relationship to actin cortical cytoskeleton as proposed in Squire *et al.* (2001). (B) En face view of idealized model for core protein clusters and cluster foci and their relationship to hexagonal actin lattice in cortical cytoskeleton. (from Weinbaum *et al.* 2003)

Chapter 2 Stagnation-point Flows in a Porous Medium

2.1 Introduction

In this chapter, we explore the transition in flow from the classical solutions of Hiemenz (1911) and Homann (1936) for the two-dimensional and axisymmetric stagnation-point boundary layers to the local solution of the Brinkman equation (1947) in the stagnation region of a cylinder or sphere as fibers of increasing concentration are uniformly added to the medium surrounding these blunt bodies and the inertia of the fluid is dissipated by the viscous resistance of the fibers. This study has been motivated by a host of biological problems that have arisen in the past decade in which the Brinkman equation has been applied to describe transport problems and problems in mechano-transduction where flow is either impinging on cells or flowing past cells that are either imbedded in an interstitial matrix or whose surface is covered by a matrix like layer at their apical surface. These applications include such diverse flow phenomena as the flow through the endothelial glycocalyx in the motion of red cells through capillaries (Wang and Parker, 1995; Damiano, 1998; Secomb *et al.*, 1998; Feng and Weinbaum, 2000), the flow past muscle cells in the artery wall (Tada and Tarbell, 2002), the flow through brush border microvilli in the proximal tubule (Guo *et al.*, 2000), the flow through fenestral pores in the capillary wall and the internal elastic lamina of arteries (Feng and Weinbaum, 2001) and the transmission of fluid shear stress to the intracellular actin cytoskeleton of the endothelial cells (Weinbaum *et al.*,2003). Another application of special interest to the authors was the air flow beneath a ski or snowboard described in F&W where the escape of air at the lateral margins is governed by the flow through the porous snow layer in the cross-

sectional plane of the planing surface. Traditional applications of the Brinkman equation can be found in several recent textbooks (Nield and Bejan, 1999; Vafai, 2000; Ingham and Pop, 2002).

As was pointed out by Joseph *et al.* (1982), the self consistent non-linear Navier-Stokes equation of Brinkman type that would govern the flow around a sphere in the presence of a swarm of other spheres or fibers is

$$\rho(\mathbf{u}\cdot\nabla)\mathbf{u}+\nabla P=\mu\nabla^2\mathbf{u}-\frac{\mu}{K}\mathbf{u}-\frac{c\rho}{K^{1/2}}|\mathbf{u}|\mathbf{u}, \tag{2.1}$$

where the last two terms on the right hand side of (2.1) describe the non-linear Darcy-Forchheimer resistance of the surrounding porous medium. Here μ is the fluid viscosity, K is the Darcy permeability, $\mathbf{u}$ is the local macroscopic velocity, ρ is the density of the fluid, and c is the Forchheimer constant, which has been experimentally measured for different porous media. Typical values of c range from 0.05 to 0.5, and a representative value for many materials is 0.1, (Beavers and Sparrow, 1969; Schwartz and Probstein, 1969; Givler and Altobelli, 1994). The last two terms can also be combined and a velocity-dependent permeability defined. In treating porous media flows in the past much more attention has been focused on the non-linearity introduced by the inertia associated with the pores of the matrix described by the $|\mathbf{u}|\mathbf{u}$ term rather than the inertia described by the $(\mathbf{u}\cdot\nabla)\mathbf{u}$ term, which gives rise to the convective boundary layer. The latter boundary layer has been extensively treated, but only in the absence of fibers.

The origin of a non-linear $|\mathbf{u}|\mathbf{u}$ term dates back to Dupuit (1863), but is now associated with Forchheimer (1901). Forchheimer also proposed a term proportional to U^3 that, more recently, was shown by Mei and Auriault (1991) to be the first inertial correction to the Stokes drag. As emphasized in Joseph *et al.* (1982), the origin of the $|\mathbf{u}|\mathbf{u}$ term arises from the pressure drag due the wake of the fibers. In the

same way that proper averaging of the viscous term in the Navier-Stokes equations gives rise to the linear Darcy term, Joseph *et al.* argue that proper averaging of the $(\mathbf{u}'\cdot\nabla)\mathbf{u}'$ term, where $\mathbf{u}'$ is the local microscopic velocity of the flow past the fibers, should give rise to a quadratic drag law. Available experimental evidence, Macdonald *et al.* (1979) and Givler and Altobelli (1994), appears to support this hypothesis although the detailed averaging of the microscopic velocity $\mathbf{u}'$ in the $<(\mathbf{u}'\cdot\nabla)\mathbf{u}'>$ term has been rigorously accomplished only for restricted flows past arrays of spheres and cylinders, (Hill *et al.*, 2001; Hill *et al.*, 2002). Hill *et al.* show that as $\mathrm{Re}_a = \rho U a/\mu$, where a is the particle/pore size, increases there is a transition from U^3 to U^2 behavior and that the U^3 behavior suggested by Mei and Auriault has a transition at Re~2.6. In the present chapter we shall limit our consideration to flows where the non-linear Forchheimer term is neglected but the linear Darcy term retained. The simplified Eq. (2.1) that results permits exact solutions which are a generalization of the classical solutions for a 2-*D* or axisymmetric stagnation-point flow. This requires that the *Re* based on the Brinkman length $K^{1/2}$, $\rho U K^{1/2}/\mu < 1$. Thus, we seek solutions where $\mathrm{Re}_D = \rho UD/\mu$, based on the body diameter D, is $>> 1$, but Re_a, based on pore or fiber dimensions, is $<< 1$.

The classical Brinkman (1947) equation is a Stokes equation in which a distributed body-force term, $\mu/K\mathbf{u}$, describing a Darcy flow is added to describe the distributed force exerted by the fibers in the porous media. When the Brinkman equation is non-dimensionalized, a single dimensionless parameter appears, D^2/K, where D is the body diameter. Thus, $K^{1/2}$ has the dimensions of length and is the characteristic thickness of the fiber-interaction layer in the Brinkman limit. If one considers Eq. (2.1) without the $|\mathbf{u}|\mathbf{u}$ term ($\rho U K^{1/2}/\mu < 1$), one finds that only one new fundamental dimensionless parameter emerges, $\beta = \upsilon/KA$, and Eq. (2.1) can be

solved exactly. Here υ is the kinematic viscosity, and A is the characteristic macroscopic velocity gradient on the length scale D. Since $A = 4U/D$, the new dimensionless parameter can be written as $D^2/(4\mathrm{Re}_D K)$. One notes that this new parameter β is the ratio of the square of two lengths, the classical boundary-layer thickness for a high-Reynolds-number flow $D/(2\mathrm{Re}_D^{1/2})$ and the fiber-interaction layer thickness $K^{1/2}$. The exact solutions of Eq. (2.1) for the stagnation-point flow presented herein show the structure of a new type of boundary layer that evolves as β varies from 0, the classical limit of the Hiemenz and Homann solutions, to $\beta >> 1$, the classical Brinkman limit where inertial effects are negligible. Using asymptotic analysis, we shall show that when $\beta >> 1$ the classical boundary layer thickness decreases as $\beta^{-1/2}$. As a practical matter, large β behavior is achieved for $\beta > 5$.

Darcy flow and inviscid irrotational flow both satisfy a potential flow equation. The streamlines in Darcy flow are identical to inviscid irrotational flow streamlines for the same flow geometry. The outer solutions for the flow past a cylinder or a sphere are identical and the local parameter A describing the macroscopic velocity gradient at the outer edge of the boundary layer, in the vicinity of the stagnation-point, is the same. The difference is only in the pressure field. A uniform outer flow at infinity in Darcy flow has a pressure gradient, whereas a potential inviscid flow satisfies the Bernoulli equation with a uniform pressure at infinity. It is, therefore, particularly instructive to examine the behavior of the pressure field as a function of the new parameter β. In the classical stagnation-point flow, $\beta = 0$, there is a monotonic pressure recovery along the stagnation-point streamline with a pressure maximum at the stagnation-point. Viscous dissipation and the resulting pressure loss is not sufficient to offset the inertial pressure recovery. In a porous medium stagnation-point flow the pressure can either increase or decrease as one approaches

the origin along the stagnation streamline, depending on the magnitude of the viscous loss due to the Darcy term. When $\beta < 1$, there is a monotonic pressure recovery, and for $\beta >> 1$, there is a pressure minimum within the fiber-interaction boundary layer that approaches the origin as $\beta^{-1/2}$.

The classical Brinkman equation can be derived either by a renormalization of the Stokes equations in a periodic microscopic domain or by averaging the Stokes equations for flow in a random assemblage of spherical particles (Howells, 1974; Tam, 1969; Lundgren, 1972). Recently, Howells studied flow through randomly distributed fibers by a renormalization technique and recovered the Brinkman equation at leading order. A more complete description of the validity of the Brinkman equation can be found in Howells (1998) and Feng *et al.* (1998). Eq. (2.1) can not be derived by these averaging procedures, since one can not write that $< (\mathbf{u}' \cdot \nabla)\mathbf{u}' > = (\mathbf{u} \cdot \nabla)\mathbf{u}$. However, in the very dilute fiber limit ($\beta = 0$) this term is clearly correct and for $\beta > 5$ the non-linear convective acceleration term becomes vanishingly small and the Brinkman limit is achieved. For β of O(1), the solutions provide results that are qualitatively instructive but whose accuracy is hard to evaluate. When $\beta = 1$, the fiber-interaction length $K^{1/2}$ is of the same order as the convective boundary layer thickness and, as pointed out by Saffman (1971), K will depend on the local velocity gradient. Despite these limitations the present exact and asymptotic solutions present a useful guide as to how a fiber matrix will modify velocity and pressure profiles in a stagnation-point boundary layer. The results could be of practical importance in fiberglass filters, sintered metallic meshes, and "open pore" polyurethane foams that are relatively rigid and of high porosity, in addition to the snowboarding application which motivated this study.

The authors' initial interest in examining the effect of inertia in Brinkman type flows was the escape of air at the lateral edges of a ski or snowboard. The flow in the plane transverse to the long axis of the ski or snowboard can be viewed, to a first approximation, as a stagnation point flow with boundary layers adjacent to both the bottom surface of the ski and the packed base on which the fresh snow rests. The key insight that a similarity solution might exist for the flow in the transverse direction was gleaned from the solutions for the pressure field beneath the snowboard shown in Figure 13 of F&W. One observes that the transverse pressure profiles are parabolic at any axial location, the same as one finds for a classical two-dimensional stagnation-point flow. This suggested that at least in the limit $h^2/K >> 1$, Brinkman stagnation-point flows might separate in the same manner as classical stagnation-point flows. As we shall see, this is indeed the case.

2.2 Formulation

2.2.1 Two-dimensional stagnation-point flow in a porous medium

As shown in Figure 2.1, we consider a flow with locally uniform vertical velocity w, whose magnitude varies with the coordinate z, which approaches along the z-axis and impinges on a flat wall in the plane $z=0$. The flow divides into two streams on the wall creating a combined convective-fiber interaction boundary layer which we shall show is of uniform thickness in the y- direction. The governing equation for this flow is a non-linear Brinkman equation (2.1) in which we have assumed that the Reynolds number based on the characteristic length $K^{1/2}$ and upstream velocity U, $\rho U K^{1/2}/\mu < 1$ so that the $|\mathbf{u}|\mathbf{u}$ term can be neglected compared to the Darcy term. For two-dimensional flow, the simplified Brinkman equation (2.1) can be written as

$$v\frac{\partial v}{\partial y}+w\frac{\partial v}{\partial z}=-\frac{1}{\rho}\frac{\partial P}{\partial y}-\frac{\upsilon}{K}v+\upsilon(\frac{\partial^2 v}{\partial y^2}+\frac{\partial^2 v}{\partial z^2}), \tag{2.2a}$$

$$v\frac{\partial w}{\partial y}+w\frac{\partial w}{\partial z}=-\frac{1}{\rho}\frac{\partial P}{\partial z}-\frac{\upsilon}{K}w+\upsilon(\frac{\partial^2 w}{\partial y^2}+\frac{\partial^2 w}{\partial z^2}). \tag{2.2b}$$

Here $\upsilon = \mu/\rho$. Eqs. (2.2a) and (2.2b) differ from the equations for classical stagnation-point flow in that there is an additional term which is due to the Darcy force, and from the classical Brinkman equation in that the convective acceleration terms are non-vanishing. In addition, from continuity we required

$$\frac{\partial v}{\partial y}+\frac{\partial w}{\partial z}=0. \tag{2.3}$$

The equations are most conveniently solved by introducing the stream function $\psi(y, z)$ defined by

$$v=\frac{\partial \psi}{\partial z}, \qquad w=-\frac{\partial \psi}{\partial y}, \tag{2.4a, b}$$

which satisfies the continuity equation (2.3) automatically.

Substituting ψ into the momentum equation (2.2a) and (2.2b), and eliminating P by cross differentiation, we obtain

$$-\psi_y(\psi_{yyz}+\psi_{zzz})+\psi_z(\psi_{yyy}+\psi_{yzz})=-\frac{\upsilon}{K}(\psi_{yy}+\psi_{zz})+\upsilon(\psi_{zzzz}+2\psi_{yyzz}+\psi_{yyyy}). \tag{2.5}$$

At $z = 0$, the planar boundary, no slip conditions require

$$w\big|_{z=0}=-\psi_y=0, \qquad v\big|_{z=0}=\psi_z=0. \tag{2.6a, b}$$

For large z, the flow has a uniform downward velocity that decreases linearly with z outside the wall boundary layer:

$$w\big|_{z\to\infty}=-\psi_y=-Az, \tag{2.7}$$

where A is the velocity gradient in the outer flow. The stream function ψ_∞ for this outer flow is

$$\psi_\infty = Ayz. \tag{2.8}$$

Because of the symmetry of the flow with respect to the z-axis and the nature of the velocity boundary conditions, it is evident that the stream function within the fiber-interaction boundary layer has the form

$$\psi = AyG(z). \tag{2.9}$$

When Eq. (2.9) is substituted into Eq. (2.5), one obtains the ordinary differential equation:

$$G_{zzz} + \frac{A}{\upsilon}(GG_{zz} - G_z G_z) - \frac{1}{K}G_z = 0. \tag{2.10}$$

Eq. (2.10) must satisfy the no-slip boundary conditions (2.6a) and (2.6b):

$$G_z(0) = 0, \qquad G(0) = 0, \tag{2.11a, b}$$

whereas as $z \to \infty$ the stream function should match the outer solution $\psi = Ayz$. Thus,

$$G\big|_{z\to\infty} = Az. \tag{2.12}$$

Eq. (2.10), though non-linear, is an exact differential, which upon integration becomes

$$G''' + \frac{A}{\upsilon}\left[GG'' - G'^2\right] - \frac{1}{K}G' = c'. \tag{2.13}$$

where c' is an integration constant that can be determined by evaluating the left hand side of (2.13) as $z \to \infty$ using Eq. (2.12):

$$c' = -\frac{A}{\upsilon} - \frac{1}{K}. \tag{2.14}$$

Thus, Eq. (2.13) becomes

$$G_{zzz} + \frac{A}{\upsilon}(GG_{zz} - G_z^2 + 1) - \frac{1}{K}(G_z - 1) = 0. \tag{2.15}$$

It is desirable to introduce the new dimensionless variables, η, ξ, g and ψ^*, as follows:

$$\eta = (\frac{A}{\upsilon})^{\frac{1}{2}} z, \qquad \xi = (\frac{A}{\upsilon})^{\frac{1}{2}} y, \tag{2.16a, b}$$

$$g(\eta) = (\frac{A}{\upsilon})^{\frac{1}{2}} G, \qquad \psi^* = \frac{\psi}{\upsilon}. \tag{2.16c, d}$$

Substituting eqs. (2.16a, c) into Eq. (2.15), we obtain a dimensionless equation for the function $g(\eta)$:

$$g_{\eta\eta\eta} + g g_{\eta\eta} + (1 - g_\eta^{\,2}) - \beta(g_\eta - 1) = 0, \tag{2.17}$$

where

$$\beta = \frac{\upsilon}{KA}. \tag{2.18}$$

The dimensionless velocity components are given by

$$v^* = \frac{v}{v_\infty} = \frac{AyG_{\cdot}}{Ay} = g_\eta(\eta), \quad w^* = \frac{w}{w_\infty} = \frac{-AG}{-Az} = \frac{g(\eta)}{\eta}. \tag{2.19a, b}$$

where v_∞ and w_∞ are the outer solutions for the horizontal and vertical velocity, respectively.

From Eqs. (2.11a, b) and (2.12), the boundary conditions are

$$g\big|_{\eta=0} = 0, \quad g_\eta\big|_{\eta=0} = 0, \qquad g_\eta\big|_{\eta\to\infty} = 1. \tag{2.20}$$

Eq. (2.17) is the non-linear Brinkman equivalent of the classical ordinary differential equation for a two-dimensional viscous stagnation-point flow. It contains two additional terms that are multiplied by a new dimensionless parameter $\beta = \upsilon/(KA)$.

The constant A describing the velocity scale is determined by examining the local behavior of the outer solution in the vicinity of the stagnation-point. Since the Darcy flow past a circular cylinder is a potential flow, the velocity field and streamline pattern is the same as the inviscid flow past a circular cylinder. Thus, the

coefficient A is exactly the same as the local solution for the outer flow for the classical stagnation-point flow past a circular cylinder:

$$A = 2\frac{U}{R}. \tag{2.21}$$

Here U is the uniform velocity far upstream of the cylinder, and R is the cylinder radius.

From (2.21) and the definition of β one obtains

$$\beta = \frac{\upsilon D}{4KU} = \frac{1}{4}\frac{D^2}{K}\frac{1}{\mathrm{Re}_D} = \frac{\delta^2}{K}. \tag{2.22}$$

Here Re_D is the cylinder Reynolds number based on its diameter D and $\delta = D/(2\mathrm{Re}_D^{1/2})$ is the characteristic thickness of the classical viscous boundary layer at the forward stagnation-point. Therefore, β is the ratio of the square of two lengths, the classical stagnation-point boundary layer thickness and the fiber-interaction layer thickness. In the limit $\beta = 0$ one obtains the classical solution for a viscous stagnation-point (Hiemenz flow), whereas in the limit $\beta >> 1$ the fiber-interaction layer controls the boundary layer and the effective boundary layer thickness is greatly decreased.

To determine the pressure field, we substitute the expressions for the velocity components Eqs. (2.19a, b) into Eqs. (2.2a) and (2.2b) and obtain

$$\frac{1}{\rho\upsilon A}P_y = G_{zzz} + \frac{A}{\upsilon}(GG_{zz} - G_z^2) - \frac{1}{K}G_z, \tag{2.23a}$$

$$\frac{1}{\rho\upsilon A}P_z = -G_{zz} - \frac{A}{\upsilon}GG_z + \frac{1}{K}G_z. \tag{2.23b}$$

From (2.13) and (2.14), the right hand side of (2.23a) is equal to the integration constant c' in (2.13). Non-dimensionalizing the resulting equations using (2.16), one obtains

$$\frac{\partial p}{\partial \xi} = -(1+\beta)\xi, \tag{2.24}$$

$$\frac{\partial p}{\partial \eta} = -g_{\eta\eta} - g_\eta g + \beta g. \tag{2.25}$$

where, p, the dimensionless pressure is given by

$$p = \frac{P}{\mu A}. \tag{2.26}$$

One observes from Eq. (2.24) that the streamwise pressure gradient is constant across the fiber-interaction boundary layer.

If the pressure at the origin (0, 0) is p_0, the pressure distribution can be readily obtained by integrating (2.24) and (2.25):

$$p(\xi,\eta) = -g_\eta - \frac{g^2}{2} + \beta\int_0^\eta g d\eta - (1+\beta)\frac{\xi^2}{2} + p_0. \tag{2.27}$$

The pressure distribution along the wall, $\eta = 0$, is given by

$$p(\xi,0) = p_0 - (1+\beta)\frac{\xi^2}{2}. \tag{2.28}$$

Since we are interested in the centerline pressure distribution p_c, we apply (2.27) at $\xi = 0$:

$$p_c(\eta) = -g_\eta - \frac{g^2}{2} + \beta\int_0^\eta g d\eta + p_0. \tag{2.29}$$

The dimensionless normal pressure gradient is independent of ξ and given by

$$\frac{dp_c(\eta)}{d\eta} = -g_{\eta\eta} - g_\eta g + \beta g. \tag{2.30}$$

Eq. (2.30) will be used to locate the position of minimum pressure in the boundary layer.

2.2.2 Axisymmetric stagnation-point

Similarly, it is possible to obtain an exact solution of the simplified non-linear Brinkman equation (2.1) without the $|\mathbf{u}|\mathbf{u}$ term for an axisymmetric stagnation-point

flow corresponding to Homann's (1936) classical solution for a viscous flow. This solution will apply in the neighborhood of a stagnation-point on a blunt body of revolution such as sphere.

We employ cylindrical coordinates (r, ϕ, z), assume that the stagnation-point is at the origin and that the flow is in the direction of the negative z-axis, with a velocity U. The axisymmetric stream function $\psi(r, \phi)$ for outer solution is of the form:

$$\psi_\infty = \frac{1}{2} A r^2 z. \tag{2.31}$$

The boundary conditions are

$$v_r\big|_{z=0} = 0, \quad v_z\big|_{z=0} = 0, \quad v_r\big|_{z\to\infty} = v_{r\infty} = \frac{A}{2} r. \tag{2.32a, b, c}$$

A similarity solution for the stream function satisfying Eq. (2.1) is now sought in the form:

$$\psi = \frac{A}{2} r^2 G(z). \tag{2.33}$$

Introducing the dimensionless variable:

$$\xi = \left(\frac{A}{\upsilon}\right)^{\frac{1}{2}} r, \tag{2.34}$$

combined with the dimensionless variables η and g defined in Eqs. (2.16a, c), one can rewrite Eq. (2.33) in the form:

$$\psi^* = \psi\left(\frac{\sqrt{A}}{\sqrt{\upsilon^3}}\right) = \frac{1}{2}\xi^2 g(\eta). \tag{2.35}$$

Following a similar procedure to that already used in section 2.2.1, one finds that $g(\eta)$ satisfies the following dimensionless differential equation:

$$g_{\eta\eta\eta} + g g_{\eta\eta} + \frac{1}{2}(1 - g_\eta^{\,2}) - \beta(g_\eta - 1) = 0, \tag{2.36}$$

where $\beta = \upsilon/(KA)$. The corresponding boundary conditions are the same as (2.20). Here A is determined from a local expansion of the outer solution in the vicinity of the stagnation-point, which has the same form as Eq. (2.21), except that in the axisymmetric case R is the radius of the sphere.

Equations (2.17) and (2.36) can be rewritten in a form to include both axisymmetric and two-dimensional stagnation-point flows in a porous medium:

$$g_{\eta\eta\eta} + g g_{\eta\eta} + \frac{1}{n}(1 - g_\eta^{\,2}) - \beta(g_\eta - 1) = 0, \tag{2.37}$$

where, n = 1 describes the two-dimensional case and n = 2 the axisymmetric one.

The dimensionless equations for the pressure gradient corresponding to (2.24) and (2.25) are

$$\frac{\partial p}{\partial \xi} = -(1 + 2\beta)\frac{\xi}{4}, \tag{2.38}$$

$$\frac{\partial p}{\partial \eta} = -g_{\eta\eta} - g_\eta g + \beta g, \tag{2.39}$$

where p is defined as in (2.26).

The integration of Eqs. (2.38) and (2.39) yields

$$p(\xi,\eta) = -g_\eta - \frac{g^2}{2} + \beta\int_0^\eta g\,d\eta - (1 + 2\beta)\frac{\xi^2}{8} + p_0, \tag{2.40}$$

where p_0 is the pressure at origin (0, 0). The centerline pressure is the same as for the two-dimensional case, Eq. (2.29).

2.2.3 Large β limit

To explore the large β limit, we rewrite Eq. (2.37) as

$$\frac{1}{\beta} g_{\eta\eta\eta} + \frac{1}{\beta} g g_{\eta\eta} + \frac{1}{n\beta}(1 - g_\eta^{\,2}) - (g_\eta - 1) = 0. \tag{2.41}$$

Inspection of Eq. (2.41) reveals that when $\beta >> 1$, $1/\beta$ is a small dimensionless parameter, which multiplies both the highest derivative term $g_{\eta\eta\eta}$ and the non-linear terms $gg_{\eta\eta}+ (1-g_{\eta}^{2})/n$. As will be shown in the Result and Discussion sections, the solution $g_{\eta} = 1$ is close to the exact solution for $g_{\eta}(\eta)$ except in the fiber-interaction boundary layer near $\eta = 0$ where g_{η} changes quickly from 0 to 1. At the same time, one also notices that the function $g(\eta)$ is not rapidly varying near $\eta = 0$, so Eq. (2.41) can be solved using a straightforward perturbation method. Allowing for the abrupt change of g_{η} across the velocity boundary layer, we stretch the coordinate system as

$$\zeta = \sqrt{\beta}\eta, \tag{2.42}$$

and seek a straightforward expansion in the form:

$$g(\zeta,\beta) = g_0(\zeta) + \frac{1}{\beta^{1/2}} g_1(\zeta) + \frac{1}{\beta} g_2(\zeta) + \frac{1}{\beta^{3/2}} g_3(\zeta) + \frac{1}{\beta^{2}} g_4(\zeta) + \cdots. \tag{2.43}$$

Equating coefficients of like powers of $\beta^{-1/2}$, one solves Eq. (2.41) subject to the boundary conditions (2.20) and obtains:

$$g = \frac{1}{\beta^{1/2}}(e^{-\sqrt{\beta}\eta} - 1 + \sqrt{\beta}\eta) + \frac{1}{\beta^{3/2}}\left[\frac{n-1}{6n} e^{-2\sqrt{\beta}\eta} - \left(\frac{\beta\eta^2}{4} + \frac{n+4}{4n}\sqrt{\beta}\eta + \frac{7n+8}{12n}\right) e^{-\sqrt{\beta}\eta} + \frac{5n+10}{12n}\right] + O\left(\frac{1}{\beta^{5/2}}\right). \tag{2.44}$$

To leading order, an asymptotic approximation to Eq. (2.44) which is uniformly valid for all η in the limit $\beta >> 1$ is:

$$g \approx \frac{1}{\sqrt{\beta}}(e^{-\sqrt{\beta}\eta} - 1) + \eta. \tag{2.45}$$

Results (2.45) can also be derived by expanding Brinkman's classic solution for the flow past around a sphere, in the vicinity of its forward stagnation-point.

As noted previously, in the limit of largeβ, the last two terms $(g_\eta - 1)$ in Eq. (2.41) are dominant for all η except when η is small, where the first term $(g_{\eta\eta\eta}/\beta)$ can not be eliminated for $\eta << 1$ because it is the highest derivative term in the equation. In contrast, the nonlinear terms $gg_{\eta\eta}/\beta + (1-g_\eta^2)/n\beta$ are higher order in an expansion in powers of $\beta^{-1/2}$. This suggests that in the large β limit, the non-linear convection terms in Eq. (2.41) can be neglected and that to lowest order a uniformly valid expansion can be obtained by solving the reduced equation

$$g_{\eta\eta\eta} - \beta(g_\eta - 1) = 0. \tag{2.46}$$

Eq. (2.46) subject to boundary conditions (2.20) has an analytical solution which is identical to (2.45). This confirms our expectation that in the large β limit convective inertial effects are negligible.

Substituting (2.45) into Eq. (2.27), one obtains the large β approximation for the pressure distribution for a two-dimensional stagnation-point flow in a porous medium:

$$p(\xi,\eta) = -\frac{\beta}{2}\xi^2 + \frac{\beta}{2}\eta^2 - \sqrt{\beta}\eta + p_0. \tag{2.47}$$

The corresponding pressure distribution for the axisymmetric case is given by:

$$p(\xi,\eta) = -\frac{\beta}{4}\xi^2 + \frac{\beta}{2}\eta^2 - \sqrt{\beta}\eta + p_0. \tag{2.48}$$

Note that in the large β limit the centerline pressure distribution is the same for an axisymmetric and two-dimensional flow and is given by:

$$p_c(\eta) = \frac{\beta}{2}\eta^2 - \sqrt{\beta}\eta + p_0. \tag{2.49}$$

2.3 Results

Eq. (2.37) and boundary conditions (2.20) are a non-linear, two-point boundary-value problem that must be solved numerically. We have used a standard shooting method combined with a fourth-order Runge-Kutta scheme. The solutions for a two-dimensional stagnation-point flow are given in Figures 2.2 and 2.3. Figure 2.2 shows how the dimensionless stream function, $g(\eta)$ changes as a function of β and Figure 2.3 shows the corresponding horizontal velocity profiles $g'(\eta)$. The velocity profiles obtained from the asymptotic solutions (2.44) and (2.45) are also shown. Since the solutions for the axisymmetric case look qualitatively the same, we have provided detailed numerical tables where the solutions can be compared in detail for β = 0, 1, 10, 100, see Table 2.1.

In Figure 2.4 we have plotted the centerline pressure distribution p_c given by Eq. (2.29) for the case of two-dimensional flow. The asymptotic solution for p_c, Eq. (2.49), is also plotted for comparison. The results for the axisymmetric case differ only in magnitude, and, as noted in Eq. (2.49), become identical for $\beta >> 1$. The detailed comparison for $p_c - p_0$ is shown in the final columns of Table 2.1, where p_0 is the dimensionless pressure at the stagnation-point (0, 0). The x-axis in Figure 2.4 is the scaled normal coordinate η / η_0^*, where η_0^* is the value of η^* at the boundary layer edge in Hiemenz flow, β =0 (η_0^* = 2.4 if v/v_∞ = 0.99). The y-axis is the scaled centerline pressure p_c / p_{c0}^*, where p_{c0}^* is the dimensionless pressure at the boundary layer edge, η_0^* = 2.4, for a classical Hiemenz flow, β = 0. One notes that for a classical stagnation-point flow, β = 0, there is a monotonic pressure recovery along the stagnation-point streamline with a pressure maximum at the stagnation-point. The viscous dissipation and resulting pressure loss is not sufficient to offset the inertial pressure recovery. However, in a porous medium stagnation-point flow, the pressure can either increase or decrease as one approaches the origin along the stagnation

streamline, depending on the magnitude of the viscous loss due to the Darcy term and, hence, the value of β. There is a maximum value of β for which there is a monotonic pressure recovery. This transition is analyzed in the Discussion section below. In general, for $\beta > 1$, there is a pressure minimum within the fiber-interaction boundary layer that approaches the origin as $\beta^{-1/2}$.

2.4 Discussion

2.4.1 Boundary layer thickness δ

The dimensionless horizontal velocity profile is given by Eq. (2.19a). It is customary to define the thickness δ of the boundary layer as the location where $v/v_\infty =$ 99%. Let the value of η at this location be denoted by η^*. Thus, the boundary layer thickness is

$$\delta \approx \eta^* \sqrt{\frac{\upsilon}{A}}. \tag{2.50}$$

The key feature in the present solution is the emergence of a new fundamental dimensionless parameter, $\beta = \upsilon/KA$. In general, the value of η^* in (2.50) will decrease as β increases, since the presence of the fibers causes a thinning of the classical viscous boundary layer thickness. This thinning is shown in Figure 2.5 where η^* is observed to decrease from $\eta^* = 2.40$ at $\beta = 0$ to 0.5 at $\beta = 100$.

In the limit of large β, one anticipates that the boundary layer thickness will become independent of the effective Reynolds number A/υ since inertial effects are small, see Eq. (2.46). In this limit the characteristic thickness of the fiber-interaction layer $\delta^* = K^{1/2}$ and the boundary layer thickness δ should be proportional to one

another and, hence, their ratio approaches a constant value. Since $\delta^* = K^{1/2} = (\upsilon / \beta A)^{1/2}$ and δ is given by (2.50),

$$\frac{\delta}{\delta^*} = \sqrt{\beta}\eta^*. \tag{2.51}$$

Figure 2.6 shows the variation of δ/δ^* as a function of β. One observes that δ/δ^* approaches a limiting value of 4.5 for $\beta >> 1$. η^* and hence δ from (2.50) are both proportional to $\beta^{-1/2}$. Thus for $\beta >> 1$, the boundary layer thickness scales as the fiber-interaction layer thickness $K^{1/2}$, and both decrease as $\beta^{-1/2}$.

2.4.2 Pressure distribution

The outer solution for a stagnation-point flow in a porous medium without inertia is a Darcy flow, whereas outer solution for a classical stagnation-point flow is an inviscid irrotational flow. Both satisfy a potential flow equation. For the same boundary conditions, the streamlines in Darcy flow without inertia are identical to those in inviscid irrotational flow. The outer solutions for the flow past a cylinder and a sphere are identical, and the local parameter A describing the macroscopic velocity gradient at the outer edge of the boundary layer in the vicinity of the stagnation-point is also the same. The difference is in the pressure field. A potential inviscid flow satisfies the Bernoulli equation with an inertial pressure recovery along the stagnation streamline, while a Darcy flow can have either a pressure recovery or pressure drop along this streamline, depending on the value of β, due to the viscous dissipation of the fibers. Eq. (2.27) for two-dimensional flow, and Eq. (2.40) for axisymmetric flow, show that as $\eta \to \infty$, $g \to \eta$, and the pressure distribution is parabolic with respect to both η and ξ. This pressure distribution is a function of β. From Eqs. (2.25) and (2.39) one observes that for $\eta >> 1$, $\partial p/\partial \eta < 0$ and there is a pressure recovery in the outer

flow for $\beta < 1$, whereas for $\beta > 1$ viscous dissipation negates this pressure recovery and $\partial p/\partial \eta > 0$. This behavior is readily observed in Figure 2.4 where the pressure outside the boundary layer is described by the portion of the curves to the right of the dashed vertical lines. $\beta = 1$ is the transition from pressure recovery to pressure loss.

The location of the minimum in the pressure profiles in Figure 2.4 is obtained by letting $dp_c/d\eta = 0$ in Eq. (2.30),

$$-g_{\eta\eta} - gg_{\eta} + \beta g = 0. \tag{2.52}$$

Eq. (2.52) must be solved numerically for the general case. However, for large β the second term in Eq. (2.52) is O ($\beta^{-1/2}$) smaller than the other two terms and (2.52) reduces to

$$g_{\eta\eta}/g = \beta. \tag{2.53}$$

Substituting Eq. (2.45) into (2.53) one finds that for $\beta >> 1$, $\eta_{min} = \beta^{-1/2}$.

The dashed vertical lines in Figure 2.4 indicate the location of the boundary layer edge corresponding to different values of β. One finds that the pressure at the boundary layer edge increases as β increases from 0 to 100, assuming that p_0, the pressure at the stagnation-point, is a fixed reference value.

2.4.3 Behavior in large β limit

Eqs. (2.44) and (2.45) are asymptotic solutions for $g(\eta)$ for a stagnation-point flow in a porous medium in the limit $\beta >> 1$. These solutions provide convenient analytic expressions from which the η velocity profiles $g'(\eta)$ can be obtained for large β. Eq. (2.45) applies if inertial effects are negligible and Eq. (2.44) provides an improved approximation that provides good accuracy for β greater than approximately 5. Figure 2.3 shows the comparison of the asymptotic and numerical

solutions for these velocity profiles for β = 5, 10 and 100 for a two-dimensional stagnation-point flow. For β = 100 the numerical and asymptotic solutions are indistinguishable on the scale shown, and for β = 5 and 10 the maximum deviation in the velocity profile obtained from the lowest order Eq. (2.45) is eight and four percent respectively. The higher order approximation given by Eq. (2.44) is accurate to less than two percent for all η for β = 5. However, Eq. (2.44) deteriorates rapidly for smaller β and should not be used for $\beta < 3$ (results not shown).

The asymptotic centerline pressure distribution $p_c(\eta)$ for the two-dimensional and axisymmetric stagnation-point flow in the limit $\beta >> 1$ is identical to $O(\beta^{1/2})$ and is given by Eq. (2.49). The comparison with the numerical solution, Eq. (2.29) for the two-dimensional case in Figure 2.4, shows good agreement for $\beta > 5$. The differences between the two-dimensional and axisymmetric pressure profiles for smaller β are given in Table 2.1.

2.5 Limitations

It is clear that the solutions presented herein, although they approach the correct limiting behavior for $\beta << 1$ and $\beta > 5$, provide only a rough quantitative prediction of the behavior for β of O(1). For $\rho UK^{1/2}/\mu < 1$Under certain conditions the non-linear Forchheimer term can be neglected. If the $|\mathbf{u}|\mathbf{u}$ term were included the simple separation of the x- and r-dependence in the solutions for the 2-*D* and axisymmetric would not be possible, and one would not be able to obtain the relatively simple exact solutions described herein. Fortunately, the criterion for the neglect of the Forchheimer term is relatively straightforward. One requires that $cRe_K^{1/2} < 1$, where *c*, the Forchheimer constant, has been experimentally measured for

different porous media. Typical values range from 0.05 to 0.5, and a representative value for many materials is 0.1, e.g. the measured value for the polyurethane foam used in Givler and Altobelli (1994) was 0.11. For this value of c the present solutions provide a reasonable description of the Brinkman limit for $\mathrm{Re}_K^{1/2} < 5$.

The interpretation of the meaning of a Reynolds number based on pore dimensions becomes questionable when one goes to very dilute fiber systems. In the Brinkman limit, Tsay and Weinbaum (1991) have shown that $K^{1/2}$ is also representative of the fiber spacing. The concept of pores is problematic if the characteristic macroscopic length is of the same order as $K^{1/2}$. In the present analysis, $\beta = 1$ implies that the classical stagnation-point boundary layer thickness is comparable to the characteristic length defined by the Darcy permeability. As pointed out by Saffman (1971), effective medium theory was never intended to describe flows where macroscopic velocity gradients occur on the length scale $K^{1/2}$. Since the fiber diameter $d << D$, the body diameter, one can readily have a situation where $\mathrm{Re}_D >> 1$, but $\mathrm{Re}_d < 1$. Essentially the fibers serve as line sources of viscous dissipation, an effect which is linear in the velocity, but the interaction between these line sources is not properly described. The Stokes solution breaks down in the far field of the fibers where inertia must be considered. In the present application this inertia is described by the $(\mathbf{u}\cdot\nabla)\mathbf{u}$ term in which the effect of the fibers is to decrease the local average macroscopic velocity $\mathbf{u}$ due to a distributed Darcy viscous dissipation. In principal one would like to locally average the $(\mathbf{u}\cdot\nabla)\mathbf{u}$ term in a region surrounding the fibers. This perhaps could be done for a periodic fiber array using an approach similar to Hill *et al.* (2001), where a lattice Boltzman approach is applied to more dense fiber arrays.

Despite these serious limitations the present analysis provides a qualitative intuitive description of the transition of a convective stagnation-point boundary layer

to a Brinkman fiber-interaction boundary layer as the newly defined dimensionless parameter β increases. This type of transition has not been studied before even in an approximate sense. One of the more interesting results is the change in the character of the pressure field along the stagnation streamline. The pressure distribution along this streamline changes character as the value of the parameter β increases, going from a flow with inertial recovery to one with monotonic dissipation as β passes through unity.

2.6 Applications

In this section we briefly return to some of the applications mentioned in the introduction. In biological applications we are frequently interested in the flow past cells modeled either as spheres or cylinders imbedded in a tissue matrix; e.g., the flow past smooth muscle cells in the artery wall or chondrocytes in collagenous tissue. To evaluate β, we assume typical cell dimensions are 10 μm and a representative Reynolds number based on cell diameter falls in the range $10^{-4} < \mathrm{Re} < 10^{-2}$. Thus, $D/\mathrm{Re}^{1/2}$ is > 100 μm. $K^{1/2}$ is roughly of the order of the fiber spacing, which is typically 10 nm or less. Therefore, β is $> 10^4$ in nearly all cellular level applications. This is the reason that the classical Brinkman equation is commonly used in cellular level flow phenomena involving either mechanotransduction or transport. In the other limit, $\beta < 1$, one has a variety of mechanical applications where small particles are imbedded in fiber materials or coarse metallic foams as described in Givler and Altobelli (1994). The validity of the governing equation has to be examined carefully in these applications for reasons discussed in the previous section.

The application which was the immediate catalyst for this study is the flow in a compressed porous snow layer beneath a snowboard or ski. As described in the

Introduction, the flow in the plane transverse to the long axis of the snowboard can be viewed, to a first approximation, as a stagnation-point flow with boundary layers adjacent to both the bottom surface of the snowboard and the packed base on which the fresh snow rests. In this case the upstream uniform velocity U can be treated as the downward vertical velocity of the snowboard $U_x dh/dx$, where h is the local depth of the compressed snow layer, and U_x is the velocity of the snowboard in the forward direction. The flow in the y direction describes the escape of air from beneath the snow board. The velocity gradient A in the outer flow is then expressed as U/h, and the new dimensionless parameter β is given by:

$$\beta = (\frac{h^2}{K})\frac{1}{\mathrm{Re}_h} = \frac{\alpha^2}{\mathrm{Re}_h}. \tag{2.54}$$

where $\alpha = h/K^{1/2}$ and

$$\mathrm{Re}_h = \frac{U_x h \dfrac{dh}{dx}}{\upsilon}, \tag{2.55}$$

is a Reynolds number based on the vertical compression velocity of the snowboard and the local compressed snow layer thickness.

The essential features of this flow are characterized by the range of β that one anticipates for typical skiing conditions. F&W show that the value of the dimensionless permeability parameter α in the classical Brinkman equation varies between 100 and 400. This value is determined by the planing angle of the snowboard, its velocity, and satisfying the constraint that the integrated lift force beneath the snowboard supports the weight of a 70 kg human, see Figure 15 in F&W. When in equilibrium the weight of the skier will compress the snow powder until the value of α is just sufficient to support this weight, for a given speed and planing angle. For U_x = 10 m/s, $\upsilon = 10^{-5}$ m^2/s, a compressed powder layer of thickness h = 10 cm, and dh/dx

= 0.02, Re_h is typically 2000, but could be as large as 5000 for larger values of U_x and dh/dx. For the above values of α and this range of Reynolds number, β varies between 2 and 80. The flow in the transverse plane thus varies from values of β at the upper end of the range where inertia is not negligible, to $\beta > 5$ where it is insignificant. These results justify the use of the Brinkman equation in F&W, where inertial effects were neglected and a classical Brinkman equation used. The foregoing estimates do not apply to groomed artificial or hardened snow, where the solid or crystal phase supplies the major fraction of the lift.

Table 2.1 Dimensionless function g, its derivatives g′, g″ and centerline pressure distribution $p_c - p_0$ at different values of β (β = 0, 1, 10, 100) for both planar (2–D) and axisymmetric (A–S) stagnation-point flow. p_0 is the dimensionless pressure at the stagnation-point

β=0								
	2-D				A-S			
η	g	g'	g''	p_c-p_0	g	g'	g''	p_c-p_0
0	0.000	0.000	1.233	0.000	0.000	0.000	0.928	0.000
0.2	0.023	0.227	1.034	-0.221	0.018	0.176	0.828	-0.171
0.4	0.088	0.414	0.846	-0.412	0.069	0.331	0.728	-0.329
0.6	0.187	0.566	0.675	-0.578	0.149	0.467	0.630	-0.473
0.8	0.312	0.686	0.525	-0.729	0.254	0.583	0.535	-0.611
1	0.459	0.778	0.398	-0.877	0.381	0.681	0.444	-0.749
1.2	0.622	0.847	0.294	-1.034	0.526	0.761	0.360	-0.895
1.4	0.797	0.897	0.211	-1.208	0.685	0.826	0.285	-1.056
1.6	0.980	0.932	0.147	-1.406	0.855	0.876	0.219	-1.237
1.8	1.169	0.957	0.100	-1.634	1.034	0.914	0.164	-1.444
2	1.362	0.973	0.066	-1.895	1.220	0.942	0.118	-1.682
2.2	1.558	0.984	0.042	-2.191	1.411	0.962	0.083	-1.953
2.4	1.755	0.991	0.026	-2.525	1.605	0.976	0.056	-2.259
2.6	1.954	0.995	0.016	-2.897	1.801	0.985	0.037	-2.602
2.8	2.153	0.997	0.009	-3.309	1.998	0.991	0.023	-2.983
3.6	2.952	1.000	0.001	-5.351	2.796	0.999	0.003	-4.902
4.4	3.752	1.000	0.000	-8.033	3.595	1.000	0.000	-7.604
β=1								
	2-D				A-S			
η	g	g'	g''	p_c-p_0	g	g'	g''	p_c-p_0
0	0.000	0.000	1.585	0.000	0.000	0.000	1.360	0.000
0.2	0.029	0.279	1.217	-0.270	0.025	0.244	1.085	-0.236
0.4	0.107	0.491	0.913	-0.474	0.094	0.437	0.856	-0.422
0.6	0.222	0.649	0.669	-0.618	0.197	0.589	0.664	-0.560
0.8	0.364	0.763	0.479	-0.715	0.327	0.705	0.506	-0.658
1	0.525	0.843	0.335	-0.779	0.477	0.793	0.378	-0.726
1.2	0.699	0.899	0.228	-0.819	0.643	0.858	0.276	-0.772
1.4	0.883	0.937	0.151	-0.844	0.820	0.905	0.197	-0.802
1.6	1.073	0.961	0.098	-0.859	1.004	0.938	0.136	-0.821
1.8	1.267	0.977	0.061	-0.868	1.194	0.961	0.092	-0.833
2	1.463	0.987	0.038	-0.872	1.388	0.976	0.060	-0.840
2.2	1.661	0.992	0.022	-0.875	1.584	0.985	0.038	-0.844
2.4	1.860	0.996	0.013	-0.877	1.782	0.991	0.024	-0.846
2.6	2.060	0.998	0.007	-0.877	1.980	0.995	0.014	-0.848
2.8	2.259	0.999	0.004	-0.878	2.180	0.997	0.008	-0.848
3.6	3.059	1.000	0.000	-0.878	2.979	1.000	0.001	-0.849
4.4	3.859	1.000	0.000	-0.878	3.779	1.000	0.000	-0.849

Table 2.1 (Continued)

β=10								
	2-D				A-S			
η	g	g'	g''	p_c-p_0	g	g'	g''	p_c-p_0
0.00	0.000	0.000	3.392	0.000	0.000	0.000	3.292	0.000
0.10	0.015	0.289	2.446	-0.267	0.015	0.282	2.390	-0.260
0.20	0.055	0.498	1.755	-0.443	0.054	0.486	1.731	-0.433
0.30	0.113	0.647	1.252	-0.515	0.110	0.634	1.249	-0.505
0.40	0.183	0.753	0.889	-0.484	0.179	0.740	0.898	-0.478
0.50	0.262	0.828	0.628	-0.355	0.257	0.817	0.643	-0.354
0.60	0.348	0.881	0.441	-0.129	0.342	0.871	0.458	-0.134
0.70	0.438	0.918	0.308	0.191	0.431	0.910	0.325	0.178
0.80	0.531	0.944	0.214	0.604	0.523	0.937	0.229	0.584
0.90	0.626	0.962	0.148	1.110	0.618	0.957	0.161	1.081
1.00	0.723	0.974	0.102	1.707	0.715	0.970	0.112	1.670
1.10	0.821	0.983	0.070	2.395	0.812	0.980	0.078	2.349
1.20	0.920	0.988	0.047	3.174	0.910	0.986	0.054	3.119
1.30	1.019	0.992	0.032	4.043	1.009	0.991	0.037	3.980
1.40	1.118	0.995	0.021	5.003	1.109	0.994	0.025	4.930
2.00	1.717	1.000	0.002	12.65	1.707	0.999	0.002	12.53
2.60	2.317	1.000	0.000	23.54	2.307	1.000	0.000	23.37
β=100								
	2-D				A-S			
η	g	g'	g''	p_c-p_0	g	g'	g''	p_c-p_0
0.00	0.000	0.000	10.08	0.000	0.000	0.000	10.042	0.000
0.02	0.002	0.183	8.244	-0.131	0.002	0.182	8.220	-0.131
0.04	0.007	0.332	6.744	-0.272	0.007	0.331	6.728	-0.271
0.06	0.015	0.454	5.516	-0.372	0.015	0.453	5.506	-0.372
0.08	0.025	0.554	4.511	-0.433	0.025	0.553	4.505	-0.432
0.10	0.037	0.636	3.688	-0.453	0.037	0.634	3.686	-0.452
0.15	0.073	0.781	2.227	-0.328	0.073	0.779	2.231	-0.328
0.20	0.114	0.868	1.343	0.046	0.114	0.867	1.348	0.045
0.25	0.159	0.921	0.809	0.668	0.159	0.920	0.814	0.666
0.30	0.206	0.952	0.487	1.540	0.206	0.952	0.491	1.535
0.35	0.254	0.971	0.292	2.659	0.254	0.971	0.296	2.653
0.40	0.303	0.983	0.175	4.026	0.303	0.983	0.178	4.018
0.50	0.402	0.994	0.063	7.502	0.401	0.994	0.064	7.490
0.60	0.501	0.998	0.022	11.97	0.501	0.998	0.023	11.95
0.70	0.601	0.999	0.008	17.43	0.601	0.999	0.008	17.41
0.80	0.701	1.000	0.003	23.87	0.701	1.000	0.003	23.85
1.00	0.901	1.000	0.000	39.74	0.901	1.000	0.001	39.71

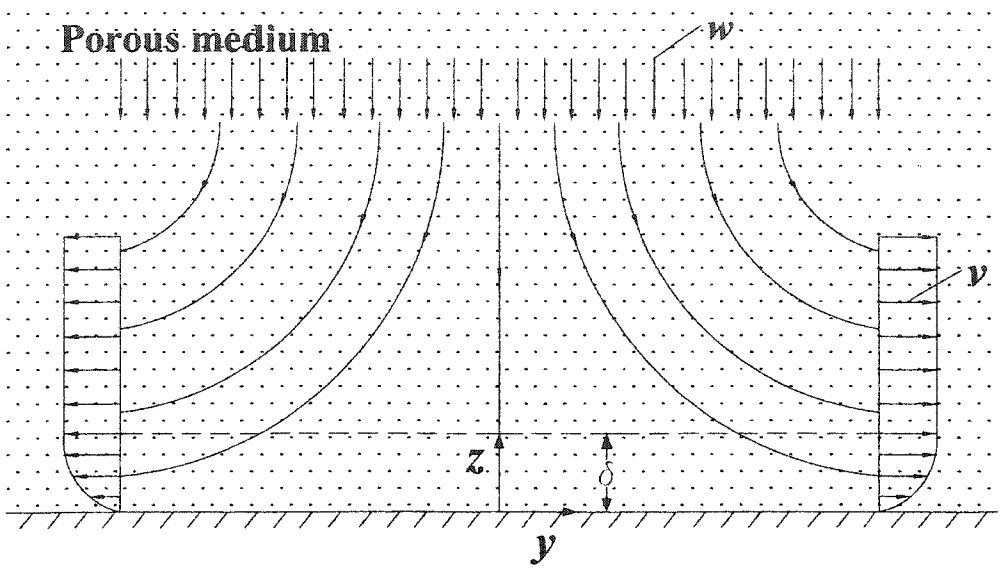

Figure 2.1 Schematic diagram for flow in the vicinity of a two-dimensional stagnation-point.

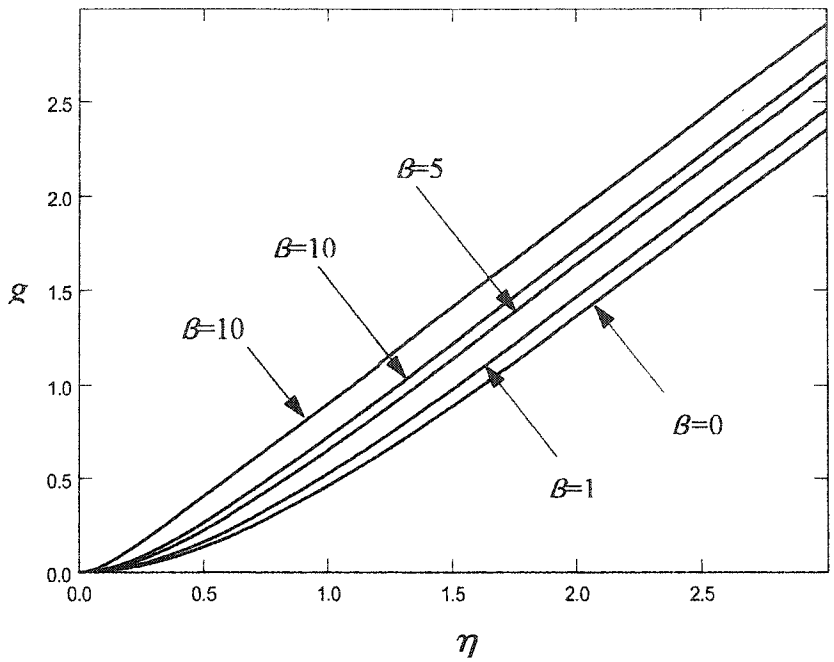

Figure 2.2 Dimensionless function g in Eq. (2.17) for two-dimensional stagnation-point flow in a porous medium for different values of β.

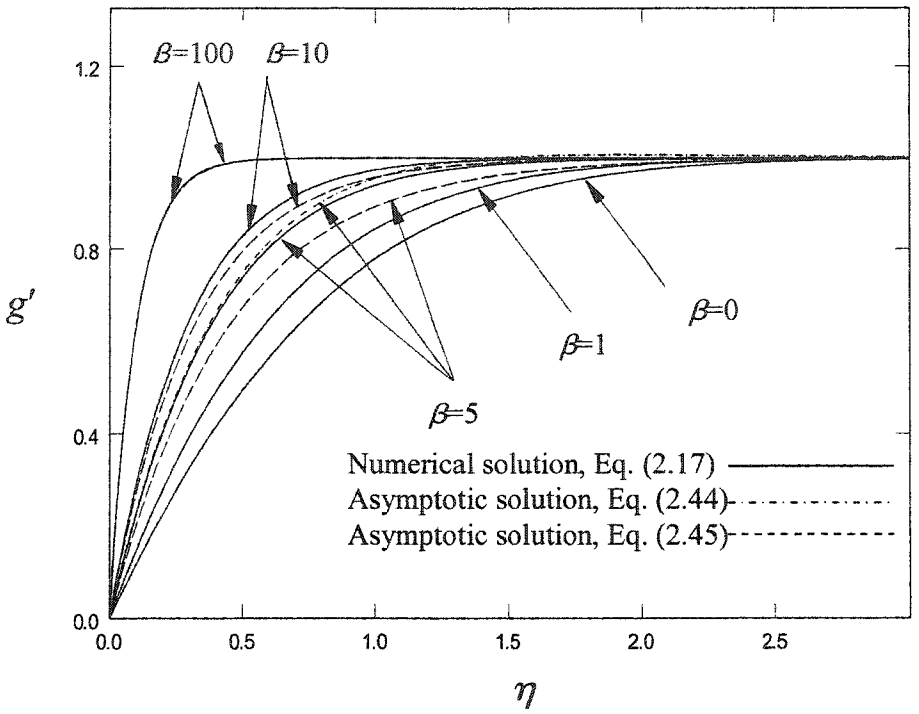

Figure 2.3 Numerical solutions for the dimensionless horizontal velocity profile g′, Eq. (2.19a), for 2-D stagnation-point flow in a porous medium at different values of β. Also shown, dash–dotted and dashed curves, are the asymptotic profiles for large β obtained from Eqs. (2.44) and (2.45), respectively.

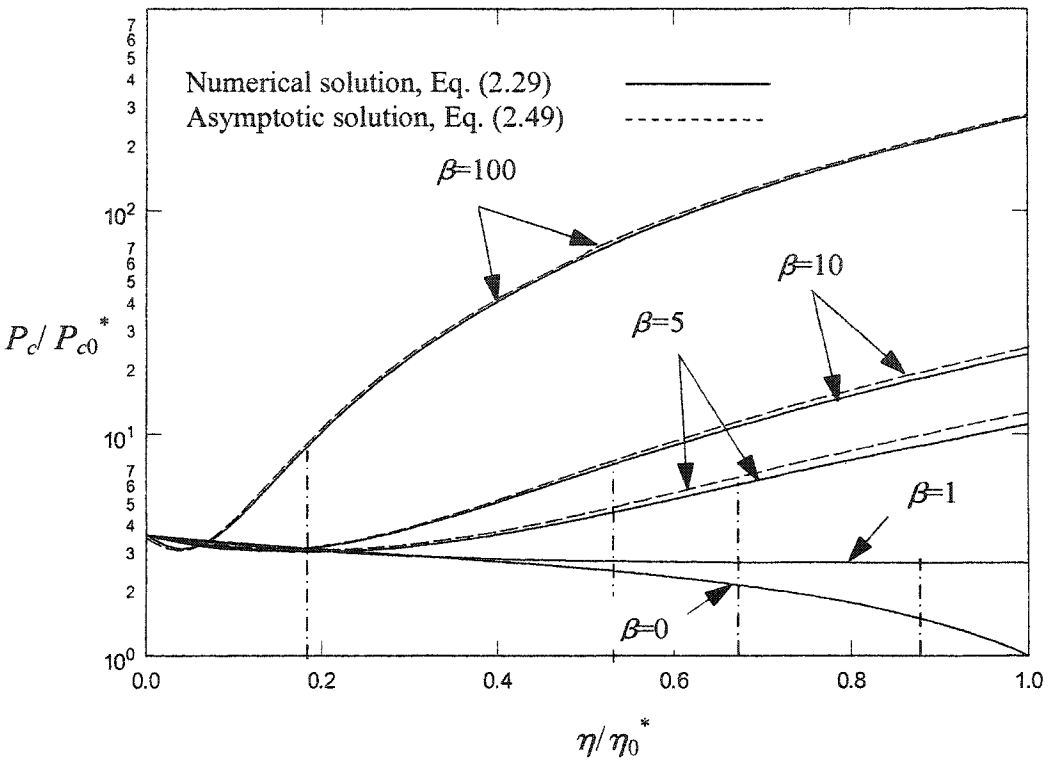

Figure 2.4 Centerline pressure distribution, Eq. (2.29), for two-dimensional stagnation-point flow in a porous medium at different values of β and its comparison with the asymptotic solution, Eq. (2.49), for β = 5, 10 and 100. The x-axis is the scaled normal coordinate η / η_0^*, where η_0^* is the boundary layer thickness for the classical Hiemenz flow, $\beta = 0$. The y-axis is the scaled centerline pressure p_c / p_{c0}^*, where p_{c0}^* is the dimensionless pressure at the boundary layer edge for the classical Hiemenz flow, $\beta = 0$.

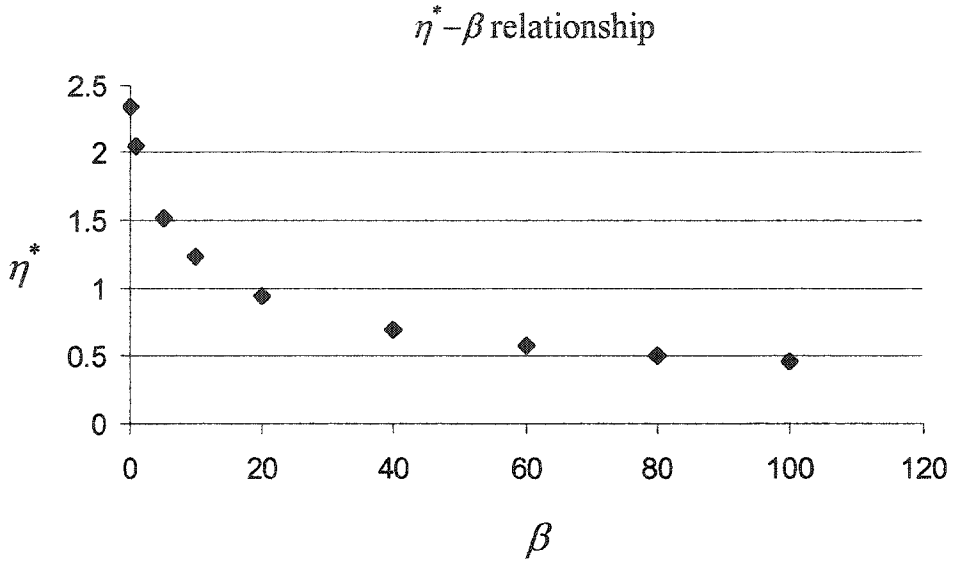

Figure 2.5 The relationship between the dimensionless boundary layer thickness η^* and the parameter β (two-dimensional case).

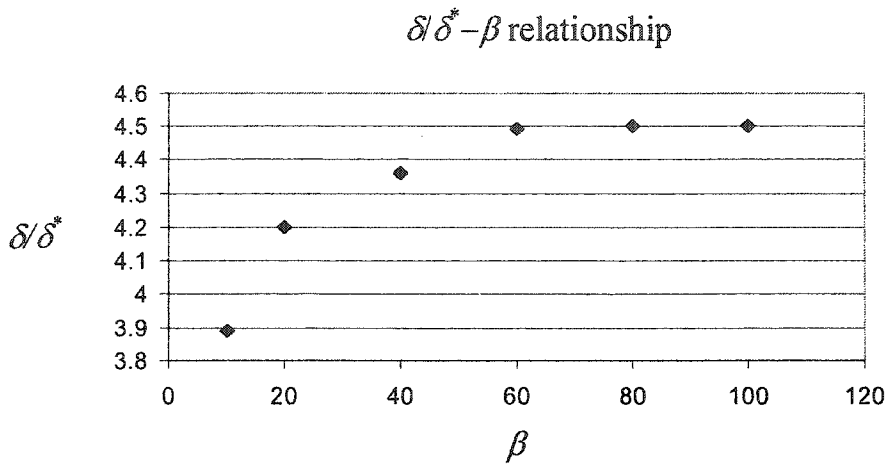

Figure 2.6 The relationship between δ/δ^* and the parameter β. Here $\delta^* = K^{1/2}$ and $\delta/\delta^* = \eta^*\beta^{1/2}$, Eq. (2.51)

Chapter 3 Dynamic compression of highly compressible porous media with application to snow compaction

3.1 Introduction

In this chapter we shall examine the dynamic compaction of a snow layer whose thickness is typical of the snow blanket that is left after a single snow fall in many regions of the United States. The study is motivated by the desire to understand the dynamic pore pressures that might build up in a new snow layer on the time scale of skiing or snowboarding. This is roughly 0.05 to 0.20 s. A specially designed porous-walled cylinder-piston apparatus has been constructed to examine the build up and decay of the excess pore pressure in two basic snow types, fresh and wind blown older snow on these time scales. The idealized experimental apparatus is not intended to realistically reproduce the boundary conditions that one encounters in these applications. In skiing or snow boarding one also needs to consider the permeability of the base layer on which the latest snow fall rests, shear forces in the snow at the edge of the planform and the lateral displacement and momentum of the displaced snow especially during turns and maneuvering. However, this initial study does qualitatively and quantitatively explore the time variation of the various dynamic forces that one encounters when one suddenly drops a weighted planar surface on a snow layer before it is supported by the pressure bulb that develops in the ice crystal phase once quasi-steady longer time settling is achieved (Shoop and Alger, 1998). To our knowledge this is the first study of snow compaction on this time scale.

This research is in large measure the outgrowth of the lubrication theory presented in F&W for flow in highly compressible porous media. The initial

application of F&W theory was the interaction of our red cells with the endothelial lining of our blood vessels. F&W predict that adhesive proteins in the opposing membranes of the red cell and endothelial cell would be in constant contact were it not for the large pressure (lift) forces generated within the matrix layer that prevent opposing membranes from touching; the excess pore pressure generated by a planing surface moving on a compressible porous media scales as $\alpha^2 = h^2/K$, and there is a remarkable hydrodynamic similarity between the motion of a red cell gliding over the compressed endothelial glycocalyx that lines our capillaries and a human skier or snowboarder skiing on fresh powder even though their difference in mass is of order 10^{15}. In this Chapter, we shall develop a novel experimental and theoretical approach for the dynamic compaction of snow to provide the first rigorous verification of the F&W theory, since the dimensions of the red cells are obviously too small to obtain the detailed pressure measurements that would be needed for this assessment.

The theoretical approach developed herein, as far as we are aware, has never been applied before to snow. It is based on consolidation theory first proposed by Terzaghi (1943) and later refined in the more general theory of Biot (1941, 1957) for two and three dimensional compression of a porous medium. Our experiments indicate that the time scale of the buildup in pore pressure of the air after dropping the piston varies between 0.05 s and 0.1 s depending on the permeability of the snow and that the decay time can be as long as 5 times longer than this if the maximum pore pressure is sufficient to bear the entire weight of the piston. However, the critical frequency for the propagation of pressure waves in a porous medium of infinite depth appears to be of the order 100 kHz if one employs the present data in the theory by Albert (1993) and Johnson (1982). Thus, the imposition of the pressure field through the fast compressive wave and the multiple reflections of this wave occur on a much

shorter time scale than the viscous phenomena we are investigating. Both the buildup and the drainage of the pore pressure within the cylinder exhibit a time-dependent quasi-steady behavior that is governed by Darcy's law, the instantaneous supporting force of the ice crystal structure and the conservation of mass for both the air and the solid phase. The weight of the piston is balanced by its inertia, the time varying integrated pressure force of the transiently trapped air and the supporting force of the ice crystals. The latter is determined from a separate experiment in which small weights are gradually added to a light weight piston and the compression of the snow measured as a function of the applied force until the full weight of the piston in the dynamic experiment is achieved. One finds that the maximum compression depends on the microstructure of the snow, but if the compression is scaled relative to the maximum compression and the force relative to the maximum force, the dimensionless empirical relation is nearly independent of the type of snow. The theoretical model is, therefore, able to predict the time-dependent variation of each force if one can estimate the change in permeability of the snow as a function of its compression. Shimizu's (1970) empirical relation is used for this purpose.

Whereas there is an extensive literature on the behavior of snow during uniaxial compression, see reviews by Shapiro *et al.* (1997) and Mellor (1964, 1977), these studies largely address the compaction of snow and its creeping behavior on much longer time scales, minutes and hours, than of interest herein. On this time scale a pressure bulb forms in the ice crystal structure and the weight is entirely supported by the solid phase. The mechanics of the initial nearly instantaneous compaction was of little interest to these authors since they were primarily concerned with the load bearing capacity of snow as a more permanent supporting structure and the changing microstructure of the snow as a function of aging and load application. In sharp

contrast, in skiing on unpacked snow (not piste snow or prepared, already compressed surfaces), one is interested in the short-lived initial compression and the changing distribution of the load between the excess pore pressure and the compression of the solid phase before creep begins.

The present study should not be confused with the propagation of shockwaves or plastic waves inside snow (Johnson, 1991, Wakahama, G. and Sato, A, 1977). For example, Johnson (1991) has developed a simple momentum model to compute the pressure attenuation of a shock wave in snow using prescribed pressure-density curves. This theory is applied to large amplitude compaction waves following explosions, whose amplitude is several orders of magnitude larger than the excess pore pressure developed during skiing, which is several kPa. Wakahama and Sato (1977) studied the plastic wave propagation inside snow when it is pushed very fast by a moving body, while in the present study the compaction speed is much slower (the maximum velocity of the falling piston is at most 1/10 of that in Wakahama and Sato (1977)).

Theoretical models used to predict the permeability of snow (see summary in Jordan *et al.*, 1999) have had only limited success. A principle difficulty is that ice crystals can take on a variety of shapes from planar dendritic (hexagonal) to columnar within each snow classification (Arons and Colbeck, 1995). The shape of newly formed snow crystals depends strongly on temperature. Studies of ice crystals in natural clouds (Ono, 1970) have shown that there are at least two basic transitions as the temperature is lowered. The primary transition, from plane hexagonal to needle-type columnar, occurs at −3.5°C and the second transition, from needle or sheath-type columnar back to a stellar or the more complex planar dendritic form, occurs at approximately −10°C. The dimensions of the various ice crystals are summarized in the classic paper by Auer and Veal (1970). Because of the great variety of shapes, ice

crystals are often described by a general parameter that is the surface area to mass ratio or specific surface area (SSA) (Fassnacht *et al.*, 1999).

There are, however, some semi-empirical or empirical relationships to predicate the snow permeability. The most widely used formula for relating permeability to crystal size and snow density is the empirical expression of Shimizu (1970):

$$K = 0.077 \exp(-0.0078\rho_s) d^2, \tag{3.1}$$

where d is the mean diameter of the snow particles. After scaling the experimental data as a function of the crystal diameter d, Jordan *et al.* (1999) demonstrated that the porosity dependence of K follows Shimizu's equation given by (3.1) rather closely. In this study, the Darcy permeability of the undeformed snow sample, K_0, is obtained from the published data of Jordan *et al.* (1999), while its variation with compression follows Shimizu's empirical relationship (3.1). As shown later in this chapter, our predictions for K_0 are very close to those measured by Albert *et al.* (2000) for similar snow conditions.

We shall present our experimental study in Section 3.2, and the theoretical model for the dynamic compression process in Section 3.3. This will be followed by a Results and Discussion Section 3.4 in which we compare our experimental data and theoretical predications and interpret the behavior observed for the two different snow types. Finally, in Section 3.5 we conclude the chapter by discussing the limitations of the present study and the modifications required to describe human skiing or snowboarding.

3.2 Experiments

3.2.1 Methods

3.2.1.1 Dynamic compression experiments

In order to obtain critical insights into the behavior of soft porous media in response to rapid compaction, a new experimental apparatus was designed, fabricated and tested in the field. A schematic of the apparatus is shown in Figure 3.1. It consists of a cylindrical sidewall which is porous and is attached to a solid base plate. A light piston that can carry additional fixed weights can slide freely along the inner surface of the cylindrical porous sidewall and provide a uniform loading to the porous media. The apparatus is designed so that there is no leakage of snow through the porous sidewall or through the clearance gap between the piston and the cylinder. Rigimesh was used to form the desired cylindrical surface, which filtered out all particles with size greater than 0.120 mm. Rigimesh is an arrangement of several screens sintered together for more rigidity. The mesh provides a negligible airflow resistance. This was evident in tests without snow, which indicated no pressure buildup during a free fall of the piston with a weight. This apparatus has not been designed to realistically reproduce the boundary conditions that one encounters in human skiing or snowboarding, where the undeformed snow near the edges of the compressed snow layer provides additional resistance and a permeable snow base is present.

Four high-frequency-response sub-miniature pressure transducers fabricated by Kulite Semiconductor Products (model XCS-062-5-D), were installed on the apparatus to measure the time-dependent pore-pressure distribution inside the snow layer and its spatial variation under rapid compression. One transducer was fixed at

the center of the piston; two were installed on the piston at distances $R/3$ and $2R/3$ away from the center, respectively, where R is the radius of the piston; and the fourth was installed in the snow along the centerline of the cylinder at an adjustable height. The inner diameter of the transducer is 1mm, which is small enough to ensure good spatial resolution of the local pressure measurement. The pressure transducers were powered by a 9-V battery and calibrated in a small portable pressure chamber with controllable pressure. The electrical outputs were filtered and amplified by EC&G pre-amplifiers and signal conditioners and then collected with an Iotech 488/8 data acquisition system of 16 bits resolution (an Iotech Filter 488/8 and an ADC488/8SA). Finally the signals were transferred to a computer for further processing. Pressure was measured relative to the ambient pressure.

Our instrumented apparatus can not only measure the transient pore pressure response to rapid deformation, but also its spatial variation. The latter is needed to address the question as to whether the snow beneath the piston is relatively uniformly compressed. This non-uniformity in density can be observed with the pressure distribution measurement along the vertical centerline of our porous cylinder- piston apparatus.

The apparatus was filled with snow up to a height of ~10 cm by using a flat surface snow shovel. Excessive snow was removed by using a long sharp steel blade so that a uniform height/depth of snow was reached in all radial positions of the apparatus. The piston was weighted and then released under gravity to compress the snow. The tolerance between the piston and the cylinder wall is large enough to allow the piston to drop with little friction between the sliding surfaces. The air leakage through this narrow gap is negligible compared to the porous side wall. Setting up the equipment and apparatus and initial tests lasted several hours. The apparatus worked

as expected. No snow leakage was observed through the cylindrical sidewall of the container or through its clearance with piston. The pressure transducers also functioned as expected in the field measurements without problems.

The depth of the snow layer before and after the compression, and its mass were measured to determine the initial and final snow density and porosity.

3.2.1.2 Static compression experiments

When the theory in F&W was first developed, it was intended to apply to highly compressible porous media in the limit where the structure is so compressible that the normal forces generated by the compression of the solid phase are negligible compared to the pore-pressure forces generated within the porous media. This is true for alpine skiing on fine-grained less permeable (wind-packed) snow at velocities greater than 20 m/s for a ski length of 2 m. As will be seen later in this chapter, at speeds typical of alpine skiing, the duration of contact time of the ski with the snow is so short (less than 0.1 s) that the lift forces generated by the air in the compressed snow layer provide a major component of the lift force.

However, in our dynamic compression experiment, the piston is always in contact with snow. As the air inside the snow drains through the porous sidewall, the resistant force of the snow crystals increases until it finally supports the entire load. To gain insight into the mechanical properties of the solid phase in the absence of piston inertia and excess pore pressure, we have measured the quasi-steady force generated when the snow is subject to incrementally increasing compressive forces. The load is added gradually to the piston so that the air in the pores could freely escape without elevating the pore pressure in contrast to the dynamic experiments in which the air in the pores is temporarily trapped before it escapes. This has also made

it possible to separate out the inertial effect associated with the acceleration and deceleration of the piston. The time interval between the load increments is long enough to allow air to escape (>1 s) but short enough to avoid bonding of the snow crystals until the final deformation is achieved and the motion is arrested. The apparatus described in the previous section for the dynamic crushing of porous media was used to determine the relation between applied quasi-static stress and displacement. This will enable us to obtain realistic estimates of the stress that is applied by the solid phase as the compression proceeds. The deformation of the snow sample was measured immediately after load application. Thus, creep deformation was excluded.

3.2.2 Snow sample characterization

The experiments were carried out in March 2002 and 2003 at Hunter Mountain in upstate NY, near the village of Tannersville. Two different types of snow samples were tested.

3.2.2.1 Wind-packed snow

Natural snow, two days old, was used in the March 2002 experiments. It was fine-grained wind-packed snow. This could be attributed to the low temperature (−10°C), the windy weather condition, and the deposition of snow. The ice crystals took a needle-type shape typical of low-temperature, windy-weather conditions. The snow sample had a relatively low porosity ($\phi_0 = 0.6$) and inferred Darcy permeability, similar to that shown in Figure 6 of Jordan *et al.* (1999).

3.2.2.2 Fresh snow

The most recent experiments were carried out in March 2003 at the same location as the experiments in the year previous. Natural freshly fallen snow was used in these experiments. The weather conditions were mild, breezy and the ambient temperature was −4° C. The snow was quite soft and fluffy and the ice crystals had a typical hexagonal shape. The fresh snow is characterized by relatively high porosity (ϕ_0 = 0.8) and Darcy permeability, similar to that shown in Figure 6 of Jordan *et al.* (1999).

3.2.3 Experimental results

3.2.3.1 Dynamic compression experiments

3.2.3.1.1 Wind-packed snow

Six dynamic compression experiments were performed with wind-packed snow. Figure 3.2a shows a representative time-dependent trace of the pressure signals at the center of the piston during the dynamic compression process using a piston mass of 5.9 kg. This is equivalent to an average normal stress of 456.6 Pa applied on the bottom surface of the piston. As can be seen from this figure, the pore pressure inside the snow powder becomes greater than the applied normal stress very quickly. This clearly indicates that air is transiently trapped before it escapes as the theory in F&W suggests. The compression ratio, $\Delta h/h_0$, in this experiment was = 0.22, with initial height h_0 = 11.43 cm. The pore air pressure rises rapidly, reaches its maximum value of 744 Pa within about 0.15 s and then falls back to zero within 1 s. At the end of the experiment the applied normal force is supported by the normal stress in the solid

phase at its new equilibrium, and the porosity of the snow sample after compaction is 0.47.

The time scale of compression is in the same range as the characteristic time of skiing (0.05 to 0.2 s) if one assumes a ski or snowboard length between 1.6 m and 2 m and a downhill speed between 10 m/s and 30 m/s. This initial experiment was performed on the first design of the apparatus in which there was only a single central pressure transducer.

3.2.3.1.2 Fresh snow

Twelve dynamic snow compression experiments with fresh snow were performed with a load of 10 kg, which is equivalent to an average normal stress of 778.2 Pa applied on the bottom surface of the piston. The signals were further processed by using a digital Butterworth low-pass filter design. Figures 3.2b and 2c show the time-dependent pressure signals during a representative test. In Figure 3.2b, signals obtained from the three equally spaced pressure transducers on the piston are shown, where ch#9 refers to the pressure transducer at the center of the piston, ch#1 and ch#2 refer to the pressure transducers on the piston at distances $R/3$ and $2R/3$ away from the center, respectively. Figure 3.2c shows signals obtained from the pressure transducers along the centerline of the cylinder, where ch#10 is the pressure transducer mounted along the centerline, 4.25 cm above the base of the cylinder. The transducers ch#9, ch#1 and ch#2 capture the radial pressure distribution, while ch#9 and ch#10 describe the pressure distribution vertically.

As shown in Figures 3.2b and 2c, the pore pressure builds to its peak value within ~0.1 s, and then relaxes on a time scale (~0.1 s) that is significantly shorter than the wind-packed snow experiment (~1 s). The peak value of pressure at the

center of the piston was 300 Pa, roughly 45% of the average normal pressure applied on the bottom surface of the piston. There is no extended pressure relaxation phase for the fresh snow because the dimensions of the piston are too small and the value of K too large for the excess pore pressure to support the full piston weight. One also notices that a sub-atmospheric vacuum pressure is created before the pore pressure finally returned to atmospheric pressure. In this experiment the compression ratio, $\Delta h/h_0 = 0.17$ and $h_0 = 8.29$ cm. The initial porosity was 0.8, which is typical for fresh snow, (Jordan *et al.*, 1999).

3.2.3.2 Static compression experiments

Static experiments were performed on the same type of snow samples using the same apparatus immediately following the dynamic compression experiment in the field. We observed that a small load increment (~0.5 kg), would not compress the snow sample, whereas, a medium increment (~ 2 kg), could. This is because the bonding between the snow crystals creates a threshold for the resistance to compression.

Figure 3.3 shows a typical incremental loading curve sequence for a static compression test on natural fresh snow with an initial porosity of 0.8. Both the applied load F and the displacement Δh have been non-dimensionalized by their corresponding maximum values. The data for the incremental loading experiments in Yong and Fukue (1977) on natural, medium-coarse-grained snow with an initial porosity of 0.6 are also plotted for comparison. They were obtained by applying loads incrementally to a snow sample under drained conditions, over a period of two and a half minutes, until a final load intensity of 0.5 kg/cm^2 was reached. As can be seen

from this figure, the current static experimental results are quite similar to the Yong and Fukue data.

The results in Figure 3.3 indicate that the supporting force from the solid phase of the snow sample increases with increasing deformation. This is due to the fact that the inter-granular contacts of the snow crystals become increasingly greater following the initial instantaneous compression. In our porous cylinder-piston experiments, with either wind-packed snow (load = 5.9 kg) or fresh snow (load = 10 kg), the maximum surface displacements were < 22% of the undeformed height of the snow layer. This is considerably less than the deformation that would be achieved for large applied loads on our low density snow where the maximum density could be as high as 0.875. This experimentally determined force-displacement profile was used to estimate the increasing force that the solid snow phase would exert on the falling piston during the dynamic snow compression experiments. This force will be used in our theoretical model to predict the time-dependent evolution of pore pressure.

3.3 Theoretical model

In this section we develop a theoretical model to predict the pore pressure distribution during the dynamic compression of snow. The motion of the falling piston is modeled by applying Newton's law. As shown in Figure 3.1, the piston is released from rest and starts falling toward a solid planar surface. The distance between the piston and the ground is assumed to be uniform in the radial direction so that the displacement, Δh, is independent of r and varies only with time. Balance of forces acting on the piston requires that

$$m\frac{d^2h}{dt^2} = -mg + F_{air} + F_{snow}, \tag{3.2}$$

where m is the mass of the piston, F_{air} is the integral of the dynamic pore pressure on the piston and F_{snow} is the resistance force due to the solid phase, the snow's inter-granular contact. This model is similar to Terzaghi's consolidation theory (Terzaghi, 1943), which has been applied in both soil mechanics and biomechanics to describe the decay of pore pressure in porous media. An approximation for F_{snow} was obtained from the static compression experiment described in the previous section, where the porous media is compressed slowly so that the trapped air has enough time to escape and the entire load is supported by the solid phase. The resistance-deformation relation in Figure 3.3 can be written in the form:

$$\frac{F_{snow}}{F_{\max}} = f(\frac{\Delta h}{\Delta h_{\max}}). \tag{3.3}$$

The dynamic pore pressure force $F_{air}(t)$ is obtained by integrating the time-dependent pressure acting over the piston:

$$F_{air}(t) = \int_0^R 2\pi r P(r,h,t)dr, \tag{3.4}$$

where R is the radius of the cylinder, and $P(r, h, t)$ is determined by solving for the instantaneous pore pressure distribution inside the snow sample.

The flow in this device is time-dependent, but the instantaneous flow is approximately described by a quasi-steady axisymmetric flow within the cylinder which satisfies Darcy's law:

$$\mathbf{q} = -\frac{K}{\mu}\nabla P, \tag{3.5}$$

where μ is the fluid viscosity, K is the Darcy permeability, $\mathbf{q}$ is the specific flux vector with components q_r, q_θ, q_z in the cylindrical coordinates (r, θ, z). In a consolidating porous medium, where the porous matrix undergoes deformation during the process of transient fluid flow, $\mathbf{q}$ is the relative specific flux with respect to the solid grains. In

the present application, the displacement of the solid particle is less than 22% of the ~10 cm thickness of the snow layer. In contrast, the characteristic discharge distance for the air is equal to the radius of the cylinder, which is 20 cm. As a result, the ice crystal velocity is negligible compared to the air velocity and $\mathbf{q}$ is approximated by the absolute flux with respect to a fixed coordinate system. Thus, we take

$$\mathbf{q} = \phi \mathbf{V}_l, \tag{3.6}$$

where $\mathbf{V}_l$ is the local absolute velocity vector (velocity of air within the pores) and ϕ is the porosity,

$$\phi = U_v / U_i, \tag{3.7}$$

where U_i is the volume of the porous medium, and U_v is the volume of void space within U_i. Relationship (3.6) is sometimes called the Dupuit-Forchheimer's equation (Bear, 1972). If the snow layer is assumed to be homogenous with a thickness h at any time t, and initially $h = h_0$, $\phi = \phi_0$, one obtains from (3.7)

$$\phi = 1 - \frac{h_0}{h}(1 - \phi_0). \tag{3.8}$$

From continuity we require that

$$\nabla \cdot (\rho \mathbf{q}) + \frac{\partial(\rho\phi)}{\partial t} = 0, \tag{3.9}$$

where ρ is the density of the air. Equation (3.9) describes the transient deformation of a consolidating medium. In our dynamic compression experiments, the pressure under the piston never exceeds 3 *kPa* above ambient pressure. Thus, the pressure change with respect to ambient pressure is only about 3%, the Mach number is <<1, and thus the air can be treated as incompressible. In fact, the isothermal compressibility defined as $\tau_t = -(1/v)(\partial v/\partial P) = -(1/h)(\partial h/\partial P)$ is of the order of 10^{-4} Pa^{-1} in the current application. Equation (3.9) then reduces to

$$\nabla \cdot \mathbf{q} + \frac{\partial \phi}{\partial t} = 0. \tag{3.10}$$

From (3.5) and (3.10), one obtains

$$\nabla^2 P - \frac{\mu}{K}\frac{\partial \phi}{\partial t} = 0. \tag{3.11}$$

After substituting for ϕ by using (3.8), (3.11) can be written in axisymmetric cylindrical coordinates as

$$\frac{1}{r}\frac{\partial}{\partial r}(r\frac{\partial P}{\partial r}) + \frac{\partial^2 P}{\partial z^2} + \frac{\mu}{K}\frac{h_0(\phi_0 - 1)}{h^2}\frac{dh}{dt} = 0. \tag{3.12}$$

Using quasi-static and homogeneous assumptions, one finds that the source term, corresponding to the last term on the left-hand side of (3.12) is a function of time only. It is desirable to introduce new dimensionless variables, P', r', z', h' and t', as follows:

$$P' = \frac{P}{P_c}, \quad r' = \frac{r}{R}, \quad z' = \frac{z}{h_0}, \quad h' = \frac{h}{h_0}, \quad t' = \frac{t}{t_c}, \tag{3.13a, b, c, d}$$

where

$$t_c = \frac{\mu R^2(\phi_0 - 1)}{P_c K}, \quad P_c = \frac{mg}{\pi R^2}. \tag{3.13e, f}$$

Substituting (3.13) into equation (3.12), we obtain a dimensionless equation for $P'(r', z', t')$:

$$\frac{1}{r'}\frac{\partial}{\partial r'}(r'\frac{\partial P'}{\partial r'}) + 4\beta^2\frac{\partial^2 P'}{\partial z'^2} + \frac{1}{h'^2}\frac{dh'}{dt'} = 0, \tag{3.14}$$

where $\beta = R/2h0$.

At the base planar boundary, $z = 0$, the no-penetration condition requires that

$$q\big|_{z=0} = 0 \Rightarrow \frac{\partial P'}{\partial z'}\Big|_{z'=0} = 0. \tag{3.15a}$$

At $z = h(t)$, the lower surface of the piston, the no penetration condition requires that the flow have a uniform downward average velocity dh/dt:

$$q\big|_{z=h} = \frac{dh}{dt} = -\frac{K}{\mu}\frac{\partial P}{\partial z} \Rightarrow \frac{\partial P'}{\partial z'}\Big|_{z'=h'} = -\frac{1}{4\beta^2(\phi_0 - 1)}\frac{dh'}{dt'} \tag{3.15b}$$

Because of the symmetry of the flow with respect to the z axis and the nature of the pressure boundary conditions, it is evident that

$$\frac{\partial P'}{\partial r'}\Big|_{r'=0} = 0, \tag{3.15c}$$

$$P'\big|_{r'=1} = 0. \tag{3.15d}$$

The boundary value problem (14-15) for the quasi-static pressure distribution inside the snow layer depends on two parameters, β and ϕ_0, and has the solution:

$$P'(r',z',t') = \sum_{k=1}^{\infty} a_k J_0(\lambda_k r') \cosh\frac{\lambda_k}{2\beta} z' + \frac{1}{4h'^2}\frac{dh'}{dt'}(1 - r'^2), \tag{3.16}$$

where

$$a_k = \frac{-\dfrac{1}{2\beta(\phi_0 - 1)}\dfrac{dh'}{dt'}\displaystyle\int_0^1 r' J_0(\lambda_k r')dr'}{\lambda_k \sinh(\dfrac{\lambda_k}{2\beta}h')\displaystyle\int_0^1 r' J_0{}^2(\lambda_k r')dr'}, \tag{3.17}$$

and

$$J_0(\lambda_k) = 0. \tag{3.18}$$

Applying (3.13) in (3.4), one rewrites the dynamic pore pressure force $F_{air}(t)$ acting on the piston in dimensionless form:

$$F_{air}{}'(t') = \frac{F_{air}(t)}{mg} = 2\int_0^1 P'(r',h',t')r'dr', \tag{3.19}$$

Substituting (3.16) into (3.19), $F_{air}'(t')$ is given by

$$F_{air}{}'(t') = \left\{ -\frac{1}{\beta(\phi_0 - 1)} \sum_{k=1}^{\infty} \frac{\left[\displaystyle\int_0^1 r J_0(\lambda_k r')dr'\right]^2}{\lambda_k \displaystyle\int_0^1 r' J_0{}^2(\lambda_k r')dr'} \coth(\frac{\lambda_k}{2\beta}h') + \frac{1}{8h'^2} \right\} \frac{dh'}{dt'}. \tag{3.20}$$

In (3.13e), the Darcy permeability K of the snow sample is also a function of compression. One employs Shimizu's equation given by (3.1) to predict this relationship (Shimizu, 1970). During the compression process, the density of the snow layer changes due to the motion of the upper boundary. For a snow layer with an initial uniform density, ρ_{s0}, the deformation-dependent average snow density, $\rho_s(h)$, is expressed as

$$\frac{\rho_s(h)}{\rho_{s0}} = \frac{h_0}{h}. \tag{3.21}$$

If the mean diameter of the ice crystal, d, remains the same and the Darcy permeability of the undeformed snow is K_0, one obtains from (3.1) and (3.21),

$$K = 0.077 \exp\left[\frac{h_0}{h} \ln \frac{K_0}{0.077 d^2}\right] d^2. \tag{3.22}$$

Employing dimensionless variables (3.13), one substitutes (3.3), (3.19) and (3.20) back into (3.2), and obtains

$$\gamma \frac{d^2 h'}{dt'^2} - \left\{ -\frac{1}{\beta(\phi_0 - 1)} \sum_{k=1}^{\infty} \frac{\left[\int_0^1 r J_0(\lambda_k r') dr'\right]^2}{\lambda_k \int_0^1 r' J_0^{\,2}(\lambda_k r') dr'} \coth\left(\frac{\lambda_k}{2\beta} h'\right) + \frac{1}{8h'^2} \right\} \frac{dh'}{dt'} - f\left(\frac{1 - h'}{1 - h_f'}\right) + 1 = 0, \tag{3.23}$$

where $\gamma = \left(t_g / t_c\right)^2$, $t_g = \sqrt{h_0 / g}$ and h_f' is the final position of the piston. γ is the square of the ratio of two time scales, the gravitational time scale t_g and the viscous draining time scale t_c. Since γ is very small one anticipates that the leading term in (3.23) is important at very short times and after that the movement of the piston is governed by the remaining terms on the right hand side of (3.3). This is a singular perturbation problem in which a small parameter multiplies the highest order derivative term. At $t = 0$,

$$h'|_{t'=0}=1, \qquad \frac{dh'}{dt'}|_{t'=0}=0. \tag{3.24a, b}$$

The differential equation (3.23) was solved numerically subject to the initial conditions given by (3.24a, b). Once $h'(t)$ was obtained, the pore pressure distribution was found by substituting our numerical result for $h'(t)$ into (3.16).

3.4 Results and discussions

3.4.1 Wind-packed snow

For the wind-packed snow sample, the initial porosity ϕ_0 was 0.6, the initial thickness, h_0, of the snow layer before compaction was 11.43 cm, and the final thickness, h_f, after compaction was $0.78h_0$. The applied load was 5.9 kg, the mean diameter of the snowflake, d, was estimated to be 0.42 mm based on the measurements in Jordan *et al.* (1999). For solid-volume fractions > 0.2, the dynamic viscosity, μ, of the trapped air inside the snow, is not simply the air viscosity at the same temperature. However, it is reasonable to assume that μ is unchanged in the experiment with value of $\mu = 1.667 \times 10^{-5}$ N·s/m^2, while K varies with compression. Using these parameter values in (3.23), one obtains the time-dependent displacement and velocity of the piston for different values of initial Darcy permeability K_0. The results are plotted in Figures 3.4a and 4b, respectively. The initial values of K_0 are varied between 0.25×10^{-9}m^2 and 1.0×10^{-9}m^2, which are typical values for wind-packed snow (Jordan *et al.*, 1999, Albert et al., 2002, Albert and Shultz, 2002, Albert, Shultz and Perron, 2000). The inverse of K is a measure of the resistance that the air encounters as it flows through the porous media, or equivalently, the damping force of the trapped air that acts on the piston. One expects as K_0 decreases it will take longer

for the air to escape since it encounters an increased resistance. Thus, the velocity of the falling piston decreases due to the increased air damping force. As can be seen from Figure 3.4, our theoretical prediction for the motion of the piston captures these features.

We have computed the time-dependent pore pressure P/P_{max} at the location of the central pressure transducer on the underside of the piston after it is released from rest for different values of permeability K_0 and compared with experimental data. A comparison between theoretical results and experimental data are shown in Figure 3.5. The solid curves in this figure are our theoretical model predictions for the time-dependent decay of the excess pore pressure. The pressure relaxation time is seen to increase as K_0 decreases. The curve that provides the best fit to the experimental data corresponds to an initial Darcy permeability, K_0, of 5.0×10^{-10} m^2. Although the choice of K_0 varies substantially with the snow sample, this value of K_0 is typical of the measurements in wind-packed fine snow (Jordan *et al.*, 1999, Albert *et al.*, 2002, Albert and Shultz, 2002, Albert, Shultz and Perron, 2000). For example, the measurements by Albert, Shultz and Perron (2000) for wind blown snow in the top 0-20 cm indicate a K_0 of 5-9×10^{-10} m^2, whereas our best fit in Figure 3.5 indicates K_0 between 5 and 7.5×10^{-10} m^2 for similar snow conditions, which is very close to Albert et al's published data.

We observed a rapid rise in pore pressure and then a decay that occurs on a time scale of roughly 0.7 s (see Figure 3.5). In contrast, the length of time that a 1.5 m snowboard traveling at 15 m/s would be in contact with a given patch of snow would be 0.1 s. It is clear from the figure that after 0.1 s the excess pore pressure has only started to relax. One expects that much of the weight of the snowboarder would be supported by the air that is still trapped in the partially compressed snow layer.

These dynamic compression experiments in wind-packed snow demonstrate that a sudden compression of wind-packed snow with limited porosity can generate peak pore pressures which are substantially larger than the average applied normal stress (see Figure 3.2a). The lumped parameter model based on the consolidation theory developed herein can reproduce the major features of the experimental data. The theoretical model provides further insight into the relative importance of the individual forces during the compression process. This is summarized in Figure 3.6 which shows the time variation of the three forces that appear in (3.2) normalized by the applied weight, *mg*. The summation of all normalized forces at any time must equal unity. In the initial stages of the compression, the force due to the pore pressure builds up very quickly and is counterbalanced solely by the inertial force of the piston. Close to P_{max} the piston achieves its maximum downward velocity, the inertial force vanishes and the solid phase force starts to increase. As noted earlier in (3.23), the highest derivative term which describes the inertia, is multiplied by a small parameter γ. This term is only important for short times of order $\sqrt{\gamma t_c}$. The solid phase force continues to increase until it fully supports the piston weight when the air pore pressure is completely vented. The good agreement between the measured and predicted pore pressure relaxation in Figure 3.5 would not have been possible if the experimentally measured relation, given by (3.3), for the force exerted by the solid phase were not reasonably accurate.

It is evident from Figure 3.6 that at t = 1.5 s, the snow has been compressed up to only ~ 40% of its final deformation. At this point the pore pressure supplies more than 80% of the total lift, the solid phase about 20% and the inertial force is negligible. Although the present experiments do not realistically reproduce the boundary conditions that one encounters in skiing or snowboarding, the contact time of a 1.5 m

snowboard moving at 15 m/s with the snow layer underneath, is in the range where the pore pressure is the dominant lifting force. The time scales for the motion of the piston in these experiments are more representative of a snowboard than a ski because of the piston dimensions. For skis the relaxation time will be significantly shorter since its narrow width will allow trapped air to escape laterally. Consequently, the solid phase is expected to carry a substantially greater portion of the load under a ski than under a snowboard.

From (3.14) in the previous section, one finds that the pressure relaxation in the porous cylinder–piston device depends on the parameter, $\beta = R/2h_0$. β denotes the weight-bearing area to ventilation-perimeter-area ratio. In Figure 3.7, one plots the theoretical predictions for the time-dependent pressure distribution, P', at the center of the piston for different values of β, where $h_f/h_0 = 0.78$, $K_0 = 5.0\times10^{-10}$ m^2. It can be seen from this figure, for $\beta > 1$, increase of β will increase the peak value of pressure and lengthen the pressure relaxation time. This is because the ventilation area is too small and the trapped air can not escape easily. However, it is also observed in this figure that for $\beta < 1$, increase in β will decrease the duration of pore pressure relaxation. This is because for $\beta << 1$, the air only vents in the vicinity of the piston and the full height of the snow column does not contribute to the drainage of the air. Thus one has a different venting behavior in either the small or large β limit with a transition that occurs at roughly $\beta = 1$.

3.4.2 Fresh snow

For the fresh snow sample, the initial porosity, ϕ_0 was 0.8, the thickness, h_0, of the snow layer before compaction was 8.29 cm, and the final thickness, h_f, after

compaction was $0.83h_0$. The applied mass was 10 kg. Using the data in Figure 6 of Jordan *et al.* (1999), we estimated the mean diameter, d, of the ice crystal to be 1mm, and the undeformed Darcy permeability, K_0, to be $\sim 10^{-8}$ m^2 for this sample. The solid fraction, $(1-\phi_0)$, was 0.2. Since fresh snow is more porous and its Darcy permeability is 20–30 times greater than wind-packed snow, one expects that the piston will be poorly damped by the trapped air in its downward descent as noted earlier in Figures 3.2b and 2c. The peak value of pressure at the center of the piston during the compaction process is only about 45% of the average normal pressure applied on the bottom surface of the piston, and vacuum pressure is created before the pore pressure finally returns to atmospheric level, indicating a rebound of the piston.

It is widely recognized that snow is a collection of ice grains interconnected in an intricate three-dimensional structure. The grain bonds between sintered snow crystals play an important role in determining the mechanical properties of snow, which are structure-dependent. During the rapid compression, the bonds between the snow grains are broken abruptly and one would not expect a significant damping effect from the snow crystals. The constitutive equation (3.3) obtained from the static experiment has no memory effect and predicts the resistance force from the snow sample quite closely. However, as the piston rebounds over a relatively longer time period after its maximum compression, the partially sintered snow sample is aerated and experiences an expansion process, during which the relative motion between the ice grains has to overcome this bonding effect and an additional damping force from the debonding of the sintered snow crystals is applied. Intuitively, one expects that this damping force is linearly proportional to velocity since this is the rate at which bonds are being broken. Thus, we approximate this debonding force by $\eta(dh/dt)mg$, where η, the debonding coefficient, is determined by requiring that the theoretical

prediction for the piston rebound process fits our experimental data once K_0 is determined from the downward phase of the piston motion. During the rebound this damping effect from the solid phase is much greater than that of the trapped air due to the much slower velocity of the piston.

Based on the above analysis, we divide the dynamic compression process and its rebound into two consecutive motions: first, a compression ending at Δh_{max} and second, a rebound to the final equilibrium position. For the compression phase, the only unknown parameter is the value of the initial Darcy permeability K_0, and for the rebound phase, the only unknown is the snow damping parameter η.

Figure 3.8 shows the time-dependent pressure P at the center of the piston for different values of initial Darcy permeability K_0 for the compression phase, and its comparison with the experimental data (ch#9 in Figure 3.2). These values of K_0 are typical for fresh snow (Jordan *et al.*, 1999). Since $1/K$ reflects the distributed Darcy resistance of the solid as the air flows through, it is expected that the pore pressure will decrease as K_0 increases. We note from this figure that $K_0 = 1.7\times10^{-8}$ m^2 provides a best fit to the experimental data. As can be seen from the figure, the pressure relaxation time for fresh snow (~0.1s) is significantly shorter than that for the wind-packed snow (~0.7 s), since the former has much higher K_0 (1.7×10^{-8} m^2) and lower solid fraction (0.2).

The theoretical predictions for the time-dependent displacement and velocity of the piston before the start of the rebound are plotted in Figures 3.9a and 9b, respectively, for the same values of K_0 as in Figure 3.8. We observe the same behavior as for wind-packed snow, i.e. the higher the initial permeability, the less the aerodynamic damping and the larger the value of Δh_{max}.

During the rebound $K_0 = 1.7\times10^{-8}$ m^2, and the dependence of K on deformation follows Shimizu's relationship, given by (3.1). The only unknown parameter is the debonding coefficient, η. Figure 3.10 shows the theoretical predications for the time-dependent pressure at the center of the piston (ch#9 in Figure 3.2) for different values of η and their comparison with the experimental data. We observe in this figure that for small values of η (e.g. $\eta = 1$ s/m), the damping force is insufficient to dissipate the inertia of the piston and the theory predicts oscillations; for large values of η (e.g. $\eta = 20$ s/m), the damping force from the debonding of the snow crystals is too large and the theoretical predictions for the pore air pressure are lower than the experimental data. The value of η that provides a best fit to the experimental data is $\eta = 15$ s/m.

Figures 3.11a and b show the theoretical predictions for the time-dependent displacement and velocity of the piston for the same values of η as in Figure 3.10. From these figures we conclude that for small values of η, oscillations are predicted due to insufficient damping, whereas for large values of η, the increased debonding force significantly decelerates the piston and increases its rebound time.

We next examine the pressure distribution in the radial direction beneath the piston surface. These results are plotted in Figure 3.12, where the theoretical predictions are compared with the experimental data at t = 1.40 s, when the peak pressure is achieved. As can be seen from this figure, the theoretical results for $K_0 = 1.7\times10^{-8}$ m^2 and $\phi_0 = 0.8$ show excellent agreement with the experimental data, and that the pressure distribution in the r direction is very close to parabolic. This is not surprising since the pressure gradient in the radial direction is dominant, and a simple plug-flow model would predict a parabolic pressure distribution in this direction.

The pressure distribution along the centerline of the cylinder (not shown here) was also computed at t = 1.40 s, when the peak value of pressure is achieved. This indicates that the pressure gradient in the z direction is quite small. This result is not unexpected since the air can only escape in the r direction where the pressure drop is much larger. The theoretical prediction for the peak value of pressure at z = 4.25 cm is 276 Pa, very close to the experimental value (280 Pa) at the same position. The small pressure difference along the centerline of the cylinder also negates the possibility of non-uniform compression and the pressure wave propagation on the time scale of interest.

Figure 3.13 shows the time-dependent variation of the scaled inertial, pore pressure, solid phase and debonding forces for the compression of fresh snow. In contrast to Figure 3.6, it is obvious that fresh snow is too porous to trap air efficiently and the damping effect from the pore air pressure is insufficient to dissipate the piston inertia on the rebound. The damping force from the debonding of the sintered crystals is required to balance the piston inertia. The fast relaxation time for the pore air pressure (0.1s) is also attributed to the high permeability and porosity of the fresh snow.

3.5 Concluding remarks

In this chapter we have developed a novel experimental and theoretical approach for examining the dynamic lift forces that are generated during the initial compaction of both fresh snow powder and wind-packed, older snow in a layer whose thickness is typical of a snow blanket that is left after a single snow fall in urban environment. Our dynamic experiments provide the first measurements of the excess pore pressure that builds up inside a snow layer after a sudden compression and its

subsequent decay due to the venting of the air from the snow at the edges of the cylinder. The spatial distribution of the pore pressure was also measured. In the static experiments, we have been able to separate out the force exerted by the solid phase (snow) as a function of its instantaneous deformation. The theoretical consolidation model provides excellent agreement with the experimental results if the initial Darcy permeability K_0 is chosen in the right range and the debonding effects of the sintered snow crystals are considered in the piston rebound. To our knowledge, this is the first time that such forces have been considered.

As described previously, there are at least four oversimplifications encountered in applying the present experiments to describe skiing: i) the resistance of the surrounding snow at the lateral edges of the skis is neglected; ii) most skiing conditions involve a fresh snow layer on a packed base, which consists of re-crystallized snow having a permeability that is 20-30 times smaller than fresh snow powder (Jordan, 1999); iii) the shear forces at the lateral edges of the skis have been neglected, though studies examining the deformation of the snow at the edge of a compression surface suggest this force is small (Shoop and Alger, 1998); iv) the inertia of the snow that is thrust out the sides of the skis during maneuvering turns has not been considered. However, the present study does qualitatively and quantitatively explore the time variation of the various dynamic forces that one encounters when one suddenly drops a weighted planar surface on a snow layer before it is supported by the pressure bulb that develops in the ice crystal phase once quasi-steady longer time settling is achieved. It confirms the basic physics in F&W that on the time scale of importance for skiing or snowboarding on fine-grained wind-packed snow, the pressure of the transiently trapped air provides a significant fraction of the total lift even for small compressions. For skiing or snowboarding on fresh snow, the solid

phase will carry a substantially greater portion of the load since the excess pore pressure will be insufficient to carry most of the load.

While the lubrication theory developed in F&W illustrates the striking similarity between a red cell gliding over the endothelial surface layer (ESL) that lines our capillary, and a human skiing, it does not provide a rigorous basis for evaluating its accuracy or limitations for the red cell, since its dimensions are obviously too small to obtain the detailed pressure measurements that would be needed for proper assessment. When the motion of a red cell is arrested, the time scale for the drainage of the fluid from the endothelial surface layer was determined by the observation that the gap between the red cell and endothelial cell membranes nearly vanishes in ~0.5 s (Weinbaum et al., 2003). This characteristic time is very close to the pressure relaxation time that we found in the present dynamic compression study with wind-packed snow. The experimental and theoretical approach presented in this chapter thus provides an intriguing analog for the drainage of the ESL following red blood cell arrest.

One limitation in the present study is that the Darcy permeability of the snow was not measured in parallel experiments with the same snow sample to verify the theoretically predicted value of K_0. However, very recently we carried out some measurements to determine the effects of compression on permeability of snow samples by using the apparatus described in Albert, Shultz and Perron (2000). Although the results of these experiments are not directly applicable to the present study, they clearly demonstrated that K_0 is reduced by an amount that varies from 17% to 50% for a 20% compression of various snow samples.

Another point of interest is the damping effect from the solid phase of fresh snow powder following maximum compression. This damping effect has been

attributed to the breaking of ice crystal bonds during piston rebound and has been modeled by a force that is proportional to the instantaneous velocity of the piston by introducing a debonding coefficient η. This damping force can also be determined by applying an accelerometer to the piston. As observed in (3.2), there are the three contributing forces, the inertial force, the pore air pressure and the snow force, whose summation is equal to mg at any time during the compression process. The pore air pressure has already been measured in the dynamic experiment; the snow force without the bond breakage effect was also measured in the static experiment. The accelerometer gives the measurement of the piston acceleration, which provides the magnitude of the inertial force. If the summation of these three measured forces is not equal to mg during the rebound, the imbalance can be attributed to the debonding force of the sintered ice crystals.

The phenomena of pore pressure increase due to sudden compression on soft porous media and that of slow pressure venting due to viscous effects which are described in the present work is a new concept. The application to snow compaction and the potential application to human skiing were chosen for their novelty. In a further study, the authors have applied this idea in the design of a future generation train that can glide on a soft porous track whose mechanical properties are similar to goose down (Wu, Andreopoulos and Weinbaum, 2004a). The key insight in the latter application is that one can greatly enhance the lift and reduce the drag due to friction in the solid phase if the lateral loss of pore pressure at the side walls of the track could be eliminated.

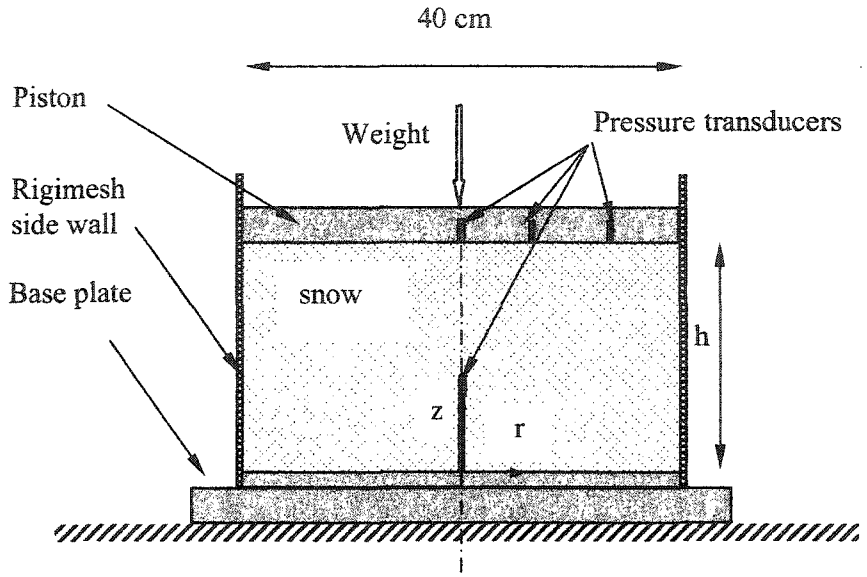

Figure 3.1 Schematic of dynamic snow compression apparatus

(a)

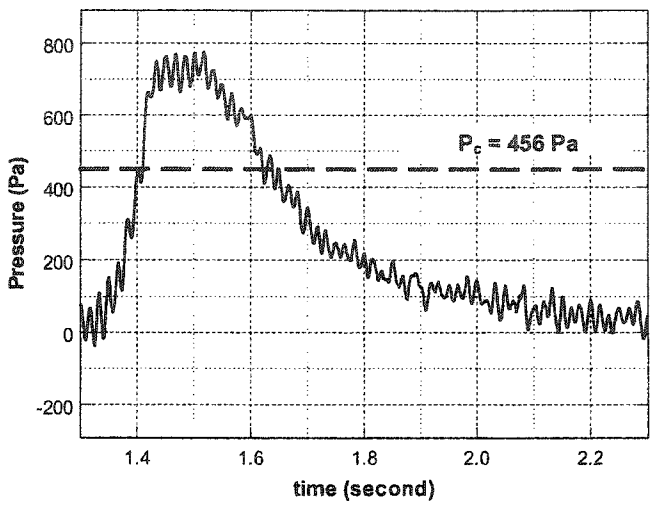

(b)

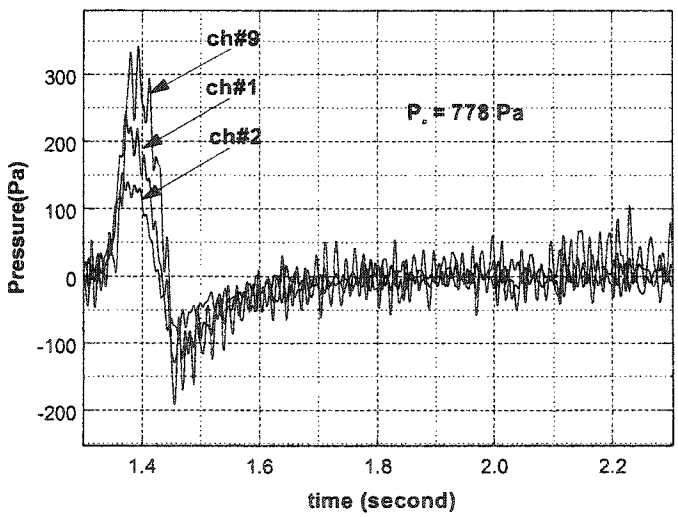

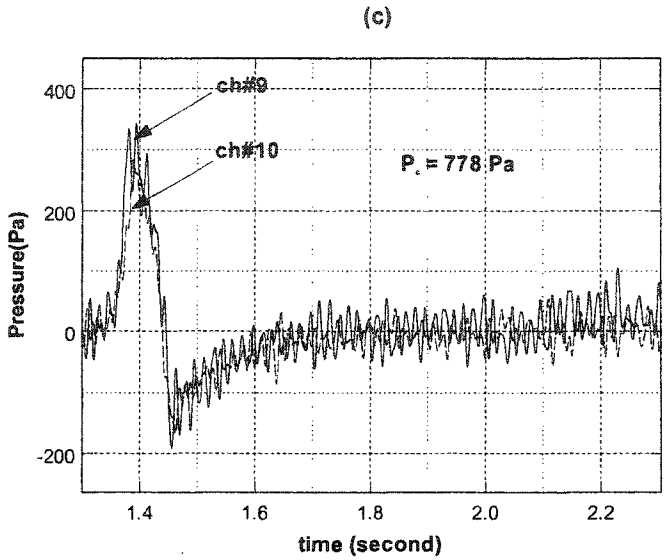

Figures 3.2 Time-dependent pressure signals obtained from the dynamic compression experiments, (a) wind-packed snow, load = 5.9 kg, equivalent to average normal stress of 456.6 Pa, $h_0 = 11.43$ cm, $h_f/h_0 = 0.78$, $P_{max} = 744$ Pa, signals are from the central pressure transducer on the piston; (b) fresh snow, $h_0 = 8.29$ cm, $h_f/h_0 = 0.83$, load = 10 kg, equivalent to average normal stress of 778.2 Pa, signals are from the three equally spaced pressure transducers on the piston, ch#9 refers to the pressure transducer at the center of the piston, ch#1 and ch#2 refer to the pressure transducers on the piston at distances R/3 and 2R/3 away from the center, respectively, where R is the radius of the piston; (c) fresh snow, $h_0 = 8.29$ cm, $h_f/h_0 = 0.83$, load = 10 kg, signals are from the pressure transducers along the centerline of the cylinder where ch#10 is the pressure transducer mounted along the centerline with 4.25 cm above the base of the cylinder

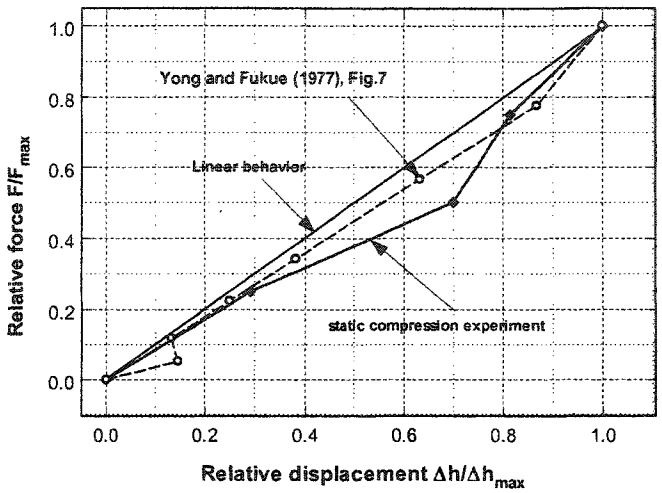

Figure 3.3 Force/displacement relation obtained in the quasi-static compression experiment with snow.

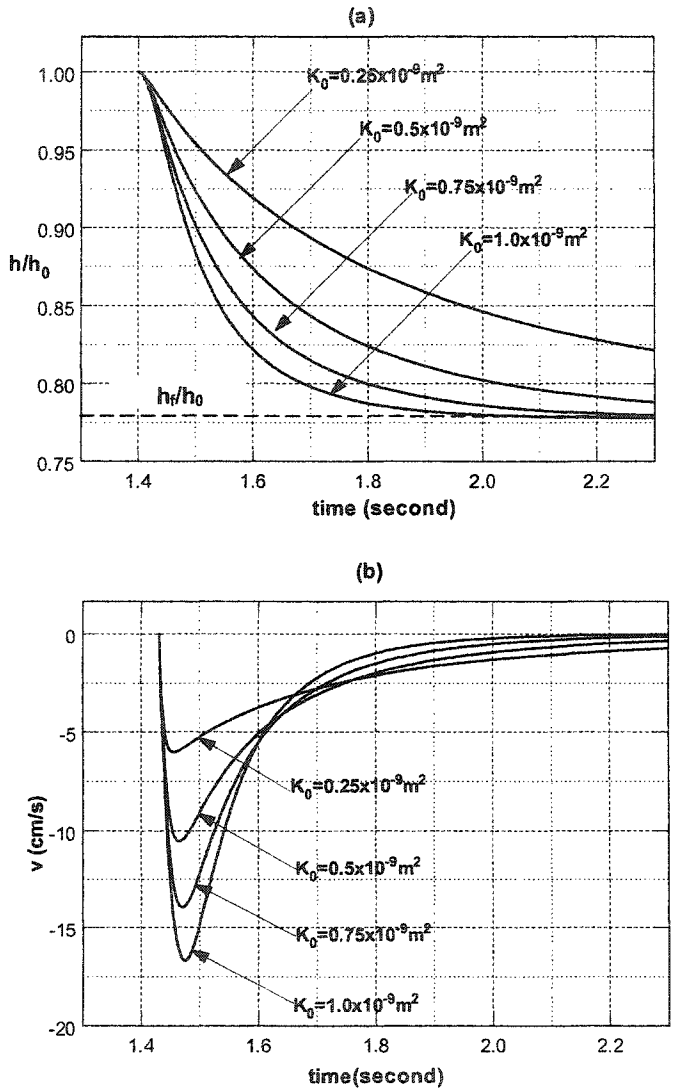

Figure 3.4 Theoretical predictions for the time-dependent (a) displacement h/h_0 and (b) velocity of the piston for different values of initial Darcy permeability K_0 of wind-packed snow, where the initial thickness of the snow layer, $h_0 = 11.43$ cm, the initial snow porosity, $\phi_0 = 0.6$. The dashed line in (a) denotes the measured thickness of the snow layer after the compaction, $h_f/h_0 = 0.78$.

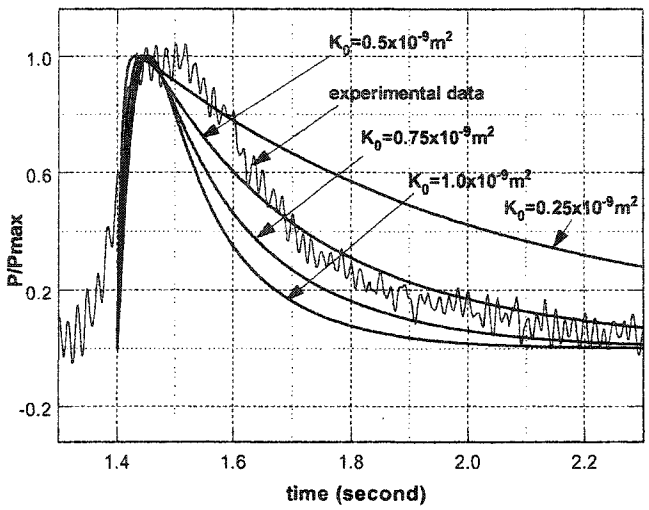

Figure 3.5 Comparison between the theoretical predictions of the time-dependent pressure and the experimental data for various values of the initial Darcy permeability K_0. The test sample was wind-packed snow with initial thickness, $h_0 = 11.43$ cm, $h_f/h_0 = 0.78$, applied mass m = 5.9 kg, $P_{max} = 744$ Pa.

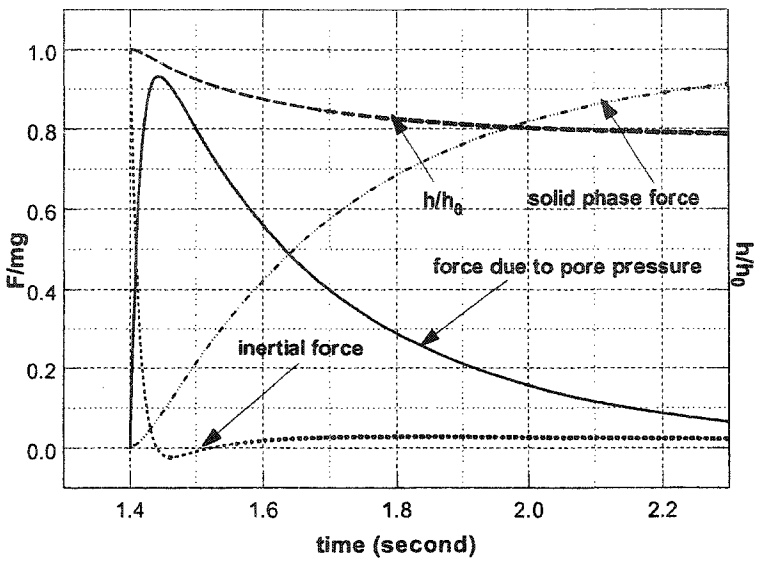

Figure 3.6 Time-dependent forces during dynamic compression of wind-packed snow.

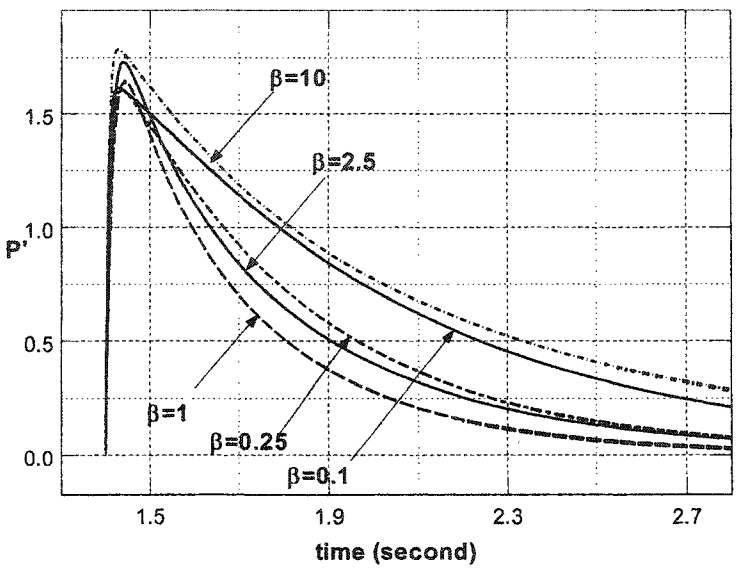

Figure 3.7 Theoretical predictions for the time-dependent pressure distribution, P', at the center of the piston for different values of β, where $h_f/h_0 = 0.78$, $K_0 = 5.0\times10^{-10}$ m^2.

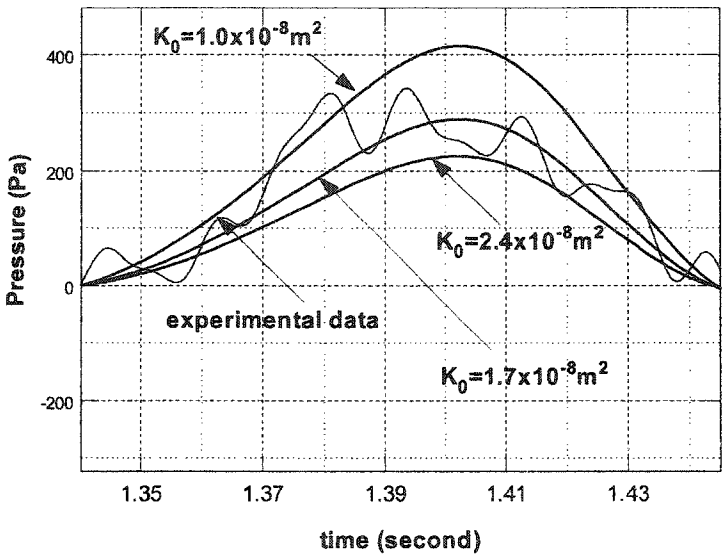

Figure 3.8 Theoretical predictions for the time-dependent pressure at the center of the piston and its comparison with the dynamic experimental data. The initial values of snow permeability, K_0 are 1.0×10^{-8} m^2, 1.7×10^{-8} m^2 and 2.4×10^{-8} m^2 respectively. The initial porosity $\phi_0 = 0.8$, the initial thickness $h_0 = 8.29$ cm, $h_f/h_0 = 0.83$, load = 10 kg.

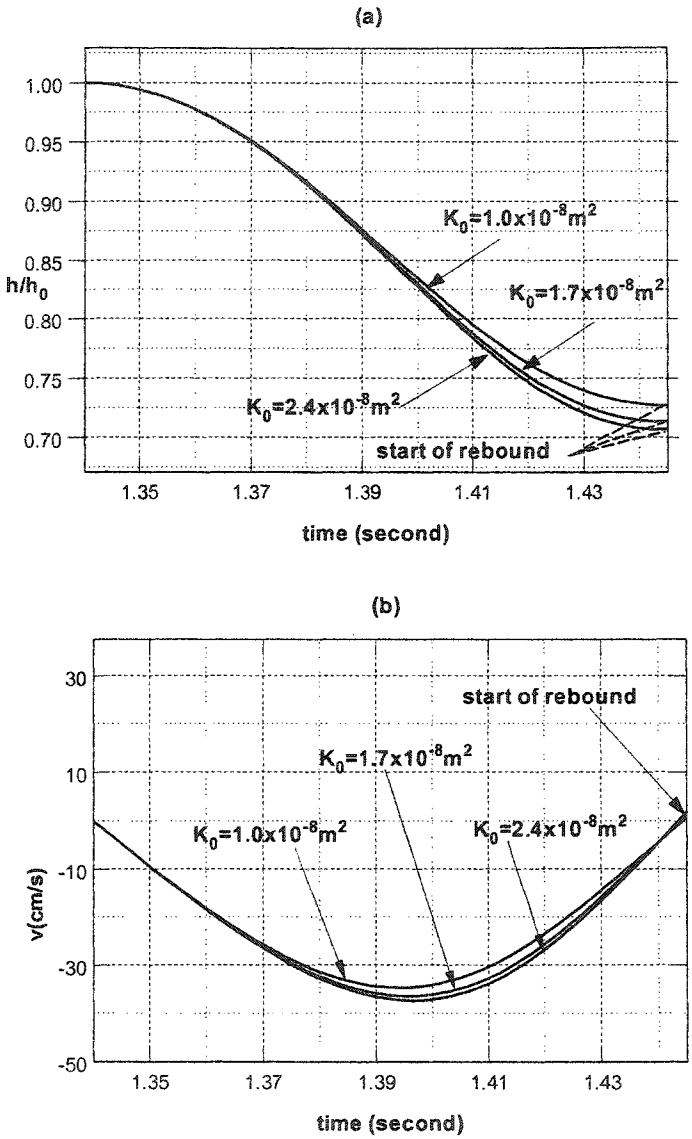

Figure 3.9 Theoretical prediction for the time-dependent (a) displacement and (b) velocity of the piston before the start of the rebound, which reveals the dependence of the piston motion on different values of the initial Darcy permeability K_0 during the dynamic compression with fresh snow. The initial porosityϕ_0 = 0.8, the initial thickness h_0 = 8.29 cm, h_f/h_0 = 0.83, load = 10 kg.

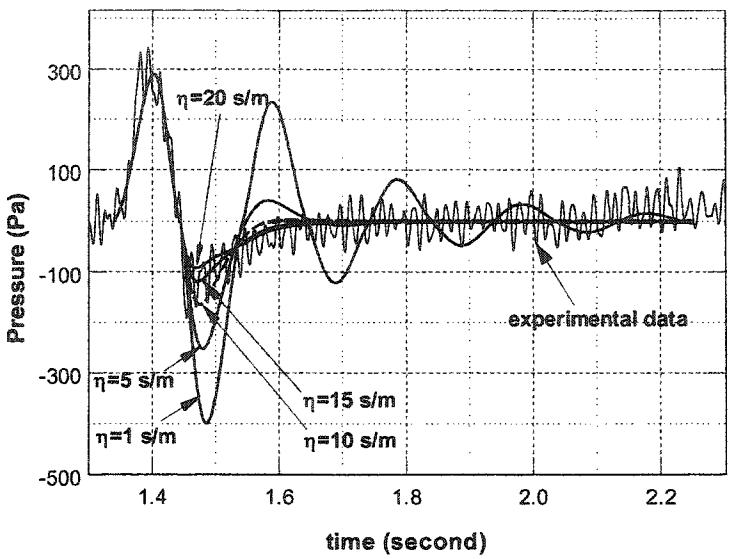

Figure 3.10 Theoretical predictions of the time-dependent pressure at the center of the piston and its comparison with the dynamic experimental data for fresh snow. The initial values of snow permeability, $K_0 = 1.7\times10^{-8}$ m^2 and the debonding coefficient η were chosen as η = 1 s/m, 5 s/m, 10 s/m, 15 s/m and 20 s/m, respectively. The initial porosity $\phi_0 = 0.8$, the initial thickness $h_0 = 8.29$ cm, $h_f/h_0 = 0.83$, load = 10 kg.

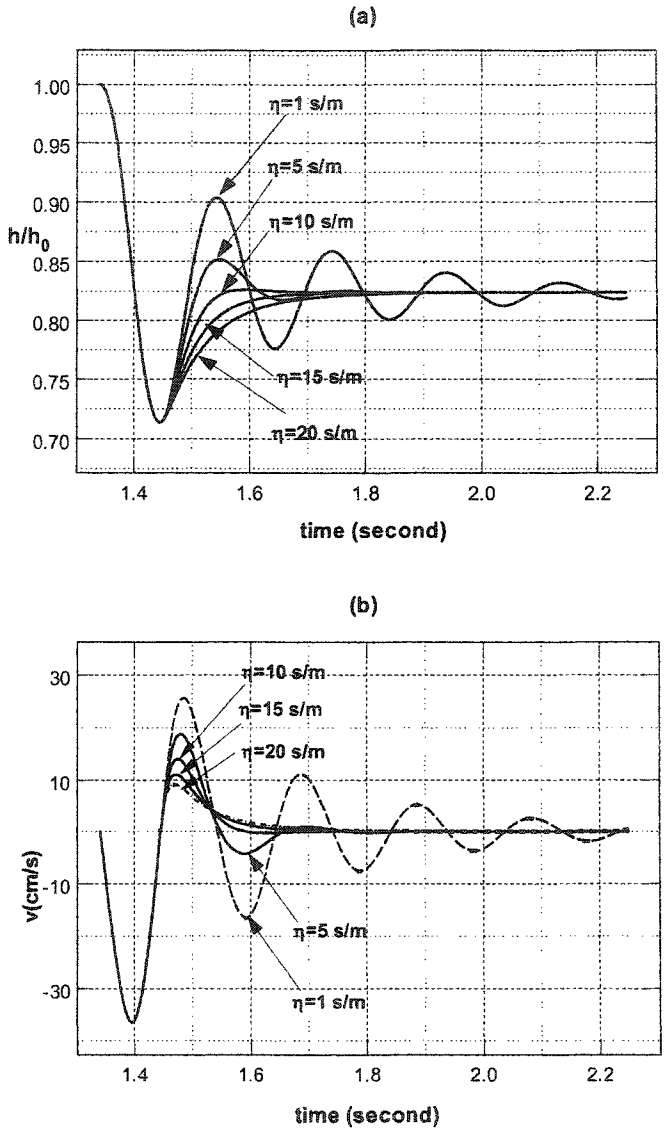

Figure 3.11 Theoretical prediction for the time-dependent (a) displacement and (b) velocity of the piston for different values of debonding coefficient η when the initial Darcy permeability K_0 =1.7×10^{-8} m^2, the initial porosity ϕ_0 = 0.8, the initial thickness h_0 = 8.29 cm, h_f/h_0 = 0.83, load =10 kg.

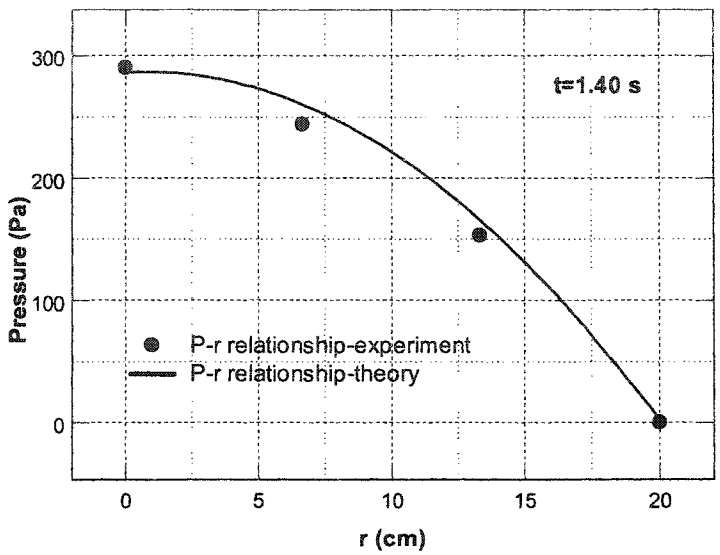

Figure 3.12 Theoretical predictions for the radial pressure distribution beneath the piston surface and its comparison with the experimental data at t = 1.40 s, when the peak value of pressure is achieved. The initial Darcy permeability of snow is K_0 = 1.7×10^{-8} m^2, the initial porosity $\phi_0 = 0.8$, the initial thickness $h_0 = 8.29$ cm, $h_f/h_0 = 0.83$, load = 10 kg.

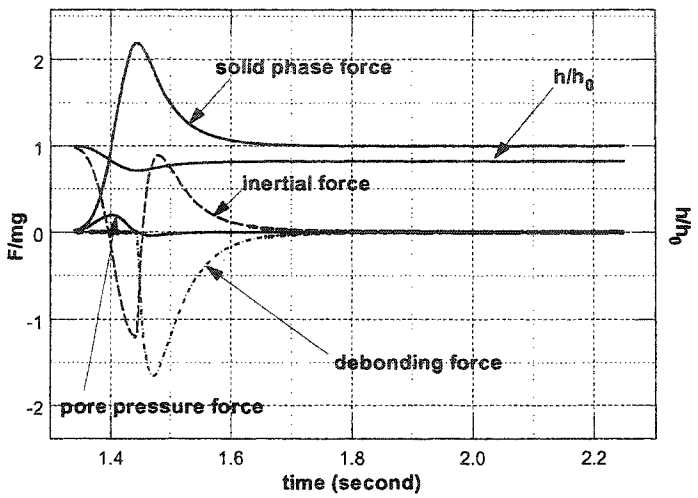

Figure 3.13 Time-dependent forces during dynamic compression of fresh snow.

Chapter 4 Lift mechanics of downhill skiing and snowboarding

4.1 Introduction

Downhill skiing or snowboarding, in its simplest form, refers to the motion of a human sliding down an inclined plane on a porous medium. The extensive classic literature treating the science of skiing and snowboarding is summarized in Lind and Sanders (1996). To our knowledge, F&W's (2000) lubrication theory for highly compressible porous media is the first attempt to predict the pore air pressure generated during downhill skiing or snowboarding. This theory shows that there is a remarkable dynamic similarity between the motion of a red blood cell (RBC) gliding at < 20 μm/s on a compressed endothelial surface layer (ESL) that lines our capillaries and a human skier or snowboarder skiing on soft snow powder even though their difference in mass is of order 10^{15}. At velocities > 20 μm/s the red blood cell rises out of the ESL and there is an intervening thin fluid lubricating layer between the ESL and the RBC membrane. F&W predict that the excess pore pressure generated by a planing surface moving on any compressible porous media scales as $\alpha^2 = h^2/K$, where h is the layer thickness and K is the Darcy permeability; and that α is of order 10^2 or larger for both red blood cells gliding on the ESL and humans skiing. Thus, the lift forces generated can be four or more orders of magnitude greater than classical lubrication theory, which explains the enhanced lift phenomenon for a human skiing or snowboarding. The enhancement in lift arises from the fact that as the matrix compresses there is a dramatic increase in the lubrication pressure because of the marked increase in the hydraulic resistance of the air as it tries to escape from the confining boundaries of the planing surface through the compressed porous layer. The

principal difference between the tightly fitting red cell in a capillary and a human skier or snowboarder is the leakage of the excess pressure at the lateral edges of the skis, as can be seen from Figure 4.1a. This leakage diminishes the maximum enhancement in the lift force by a factor W^2/L^2 where W/L is the ratio of the width to the length of the planing surface.

The fundamental insights gained from F&W theory provide the basis and starting point for the present study to understand the lift mechanics of downhill skiing and snowboarding. However, this theory has the following major limitations: (i) in the analysis by F&W, the local variations in the Darcy permeability in the compressed fiber layer are determined from solutions of the Stokes equations for the local average flow through a compressed two-dimensional fiber array. This approximate model was applied in F&W to both the ESL and fresh snow powder. In the case of snow, it was only intended to capture the essential physics of the compression process due to the wide variety of shapes and sizes of snow crystals from planar dendritic (hexagonal) to columnar within each snow classification (Arons and Colbeck, 1995); (ii) when the theory in F&W was first developed, it was intended to apply to highly compressible porous media in the limit where the structure is so compressible that the normal forces generated by the compression of the solid phase were negligible compared to the pore-pressure forces generated within the porous media. The experiments in Wu *et al.* (2004a and 2005b) suggested that this might be true for snowboarding on fine-grained less permeable (wind-packed) snow at velocities greater than 20 m/s for a snowboard length of 2 m, where the duration of the contact time of the snowboard with the snow is so short (less than 0.1 s) that the lift forces generated by the trapped air in the compressed snow layer might provide the major component of the lift force. However, for snowboarding on more permeable (fresh) snow where the medium is too porous,

or for skiing where the dominant pressure relaxation length, the width of the ski W, is too small, the air can not be efficiently trapped inside the porous media and the compressed snow crystals should support much of the load; (iii) the F&W analysis emphasizes lift generation in porous media, but does not treat the other forces and moments acting on the skier or snowboarder, which are necessary for examining the overall lift mechanics involved in downhill skiing or snowboarding; (iv) the analysis in F&W is based on a generalized Reynolds equation derived using effective medium theory (Brinkman equation). The predictions of F&W and later studies by Wu *et al.* (2005a) suggest that it can be further simplified for the case of skiing or snowboarding using Darcy's law.

In the present study, we develop a new theoretical approach which combines the lift mechanisms from both the trapped air and the solid phase (ice crystals) and treat these limitations. The pore air pressure distribution beneath the planing surface is based on a consolidation theory where the local change of Darcy permeability due to the compression of the snow layer is obtained from the Shimizu's classical empirical relationship (1970). The local resistance force from the solid phase (ice crystals) is based on the static experiments of Wu *et al.* (2005b). We then perform a force and moment balance acting on the skier or snowboarder for different snow types and different planing surfaces (ski or snowboard).

Because of the wide variety of sizes and shapes of ice crystals, theoretical models used to predict the permeability of snow have had only limited success, (see summary in Jordan *et al.*, 1999). However, there are semi-empirical or empirical relationships to predicate the snow permeability. The most widely used formula for relating permeability to crystal size and snow density is the empirical expression of Shimizu (1970):

$$K = 0.077 \exp(-0.0078\rho_s) d^2. \tag{4.1}$$

Here ρ_s is the density of snow and d the mean diameter of the snow particles. After scaling the experimental data as a function of the crystal diameter d, Jordan *et al.* (1999) demonstrated that the porosity dependence of K follows Shimizu's equation given by (4.1) rather closely.

In section 4.2.1, we shall first employ Shimizu's equation given by (4.1) to predict the local change of Darcy permeability K as a function of compression. In section 4.2.2 we will use a consolidation theory to predict the pore air pressure distribution beneath a ski or snowboard surface. In section 4.2.3 we will consider the lift force from the solid phase, and in sections 4.2.4 and 4.2.5 the force and moment balance, respectively. The results of the theoretical model are presented in section 4.3. Finally, in section 4.4 we conclude the chapter with a discussion of the limitations of the present model.

4.2 Formulation

4.2.1 Darcy permeability of snow

In general, as a fresh snow layer is compressed by a planar surface, the density of the snow layer changes due to the motion of the upper boundary. In the present analysis we assume that a fresh snow layer of the depth h_0 either rests on the ground or over a previously packed snow base whose permeability is much smaller than the new snow layer. If one assumes that the new snow layer is uniformly compacted in the vertical direction, whereas in the horizontal plane there is no crystal movement, the deformation-dependent average snow density, $\rho_s(h)$, where h is the local instantaneous height of the new snow layer, is expressed as

$$\frac{\rho_s(h)}{\rho_{s0}} = \frac{h_0}{h}, \tag{4.2}$$

if the new snow layer has an initial uniform density ρ_{s0} at its initial height h_0,. If the mean diameter of the ice crystal, d, remains the same and the initial Darcy permeability of snow is K_0, one obtains from (4.1) and (4.2),

$$K = 0.077 \exp\left[\frac{h_0}{h} \ln \frac{K_0}{0.077 d^2}\right] d^2. \tag{4.3}$$

In the current application shown in Figure 4.1b, one assumes the bottom surface of a ski or snowboard is planar and there is no lateral tilt or edging. Thus, the local thickness, h, of the fresh snow layer beneath the planing surface is a linear function of x:

$$h = h_2 - \tan\gamma \cdot (L - x), \tag{4.4}$$

where h_2 is the thickness of the snow layer at the leading edge and γ is tilt angle of the ski or snowboard. The slope of the ski relative to the ground or snow base is given by

$$\tan\gamma = \frac{k-1}{L} \cdot \frac{h_2}{k}, \tag{4.5}$$

where $k = h_2/h_1$ is the compression ratio. Substituting (4.4) and (4.5) into equation (4.3), we have

$$K = 0.077 \exp\left[\frac{1}{1 - \left(1 - \frac{1}{k}\right) \cdot \left(1 - \frac{x}{L}\right)} \ln \frac{K_2}{0.077 d^2}\right] d^2, \tag{4.6}$$

where K_2 is the Darcy permeability of the snow beneath the leading edge of the planing surface which can be determined from equation (4.3) for given values of undeformed Darcy permeability, K_0, undeformed snow layer thickness, h_0, and the value of h_2, as shown in Figure 4.1b.

To illustrate how K varies with position and the compression ratio, one has plotted in Figure 4.2 the variation of K from leading to trailing edge for different compression ratios, k. In this calculation the snow layer at the leading edge is undeformed, $h_2 = h_0 = 10$ cm (typical value in the snow compaction measurements by Wu *et al.* (2005b), the diameter of the snowflake d is 0.001 m and the permeability of the snow beneath the leading edge of the planing surface, $K_2 = K_0 = 1.7 \times 10^{-8}$ m^2 (typical value of fresh snow, Wu *et al.* (2005b)). One observed in Figure 4.2 a monotonic variation of Darcy permeability K because of compression. One expects that the large decrease in K from leading to trailing edge will produce a pronounced asymmetry in the pressure loadings and an increase in the maximum pressure and the resulting integrated lift force at the higher values of k.

4.2.2 Pore-pressure

4.2.2.1 Governing equations

In F&W, the authors considered a two-dimensional rigid boundary moving arbitrarily with velocity $U = (U_x, U_y, U_z)$ over a fiber layer as shown in Figure 4.1a. Effective medium theory based on the Brinkman (1947) equation

$$\mu\left(\nabla^2 - \frac{1}{K}\right)\vec{u} = \nabla P \tag{4.7}$$

was used to describe the flow in the fiber layer, where μ is the air viscosity. For large $\alpha = h/\sqrt{K}$, F&W predict that a one-dimensional plug flow develops at all locations, that there is a thin fiber boundary layer at the upper and lower surfaces and there is little motion over most of the matrix except near boundaries and as one approaches the leading and trailing edges (see Figure 10 in F&W). For a 10 cm-thick snow layer, α is in the order of 10^3. It is clear that the x velocity component u satisfies Darcy's

law and the profile approaches that of a uniform plug flow outside the thin fiber interaction layers adjacent to the bottom of the ski or the ground. Thus,

$$u = -\frac{K}{\mu}\frac{\partial P}{\partial x}. \tag{4.8}$$

Since the length of a ski or snowboard is much larger than its width, velocities will be much larger in the transverse y, z plane than in the x direction except at the upper boundary where there is a very thin fiber interaction boundary layer due to the motion of the ski or snowboard. Wu *et al.* (2005a) have proposed that the flow in the transverse plane can be viewed, to a first approximation, as a stagnation-point flow in a porous medium. The key insight that a similarity solution might exist for the flow in the transverse direction was gleaned from the solutions for the pressure field beneath a snowboard shown in Figure 13 of F&W. One observes that the transverse pressure profiles are parabolic at any axial location, the same as one finds for a classical two-dimensional stagnation-point flow. This suggested that at least in the limit $h^2/K >> 1$, Brinkman stagnation-point flows might separate in the same manner as classical stagnation-point flows, where the vertical velocity at the upper boundary is equivalent to the incoming flow in the classical 2-D stagnation point boundary layer. Wu *et al.* (2005a) have obtained non-linear exact and asymptotic solutions to a stagnation point flow in a porous medium, which show the transition in behavior that occurs between the classical solutions of Hiemenz (1911) and Homann (1936) for the two-dimensional and axisymmetric stagnation-point boundary layers and the local expansion of the Brinkman solution for the flow past a cylinder or sphere in the stagnation regions as the Darcy permeability is decreased. In this analysis, a new fundamental dimensionless parameter $\beta = \upsilon/KA$ emerges, where υ is the kinematic viscosity and A is the characteristic velocity gradient imposed by the external flow. In

the case of skiing or snowboarding, $A= -U_z(x,y,h)/h$. Here the vertical velocity of the upper boundary $U_z(x, y, h)$ in the general case is given by

$$U_z(x,y,h) = U_x \frac{\partial h}{\partial x} + U_y \frac{\partial h}{\partial y}, \tag{4.9}$$

where $h(x, y)$ is the local gap height and U_x, U_y the velocity of the ski or snowboard in the x, y directions. Thus,

$$A = -\frac{U_z(x,y,h)}{h} = \frac{U_x}{h}\frac{\partial h}{\partial x} + \frac{U_y}{h}\frac{\partial h}{\partial y}. \tag{4.10}$$

The structure of a new type of boundary layer is observed in the analysis that evolves as β varies from zero, the classical limit of the Hiemenz and Homann solutions, to $\beta >>1$, the classical Brinkman limit where inertial effects are negligible. These solutions show that for the case of skiing or snowboarding where $\beta >> 1$, the viscous boundary layer is vanishingly thin and one is left with an outer flow for the velocity field which is given by

$$v = -\frac{K}{\mu}\frac{\partial P}{\partial y}, \tag{4.11}$$

$$w = -Az. \tag{4.12}$$

The v velocity profile is a uniform plug profile in the y direction which increases linearly with distance y from the centerline of the ski or snowboard, while the downward velocity w decreases linearly with z.

Substituting (4.8), (4.11) and (4.12) into the continuity equation,

$$\frac{\partial u}{\partial x} + \frac{\partial v}{\partial y} + \frac{\partial w}{\partial z} = 0, \tag{4.13}$$

we obtain,

$$\nabla^2 P = -\frac{\mu}{K} A - \frac{1}{K} \nabla P \cdot \nabla K. \tag{4.14}$$

Equation (4.14) is the new simplified governing equation for the pore pressure in skiing or snowboarding. The two terms on the right hand side have a simple interpretation. The first term proportional to A is the forcing due to the angle of attack and the lateral edging of the ski or snowboard. The second term arises from the variation in permeability due to the compression of the snow. Both the first and the second term include lateral tilt or edging which is reflected in the partial derivative with respect to y. If both terms vanish one obtains the potential equation for Darcy flow without any forcing.

4.2.2.2 No lateral tilt or edging

In the present study, we shall only examine the simple case where there is no lateral tilt to the ski or snowboard, $h = h(x)$, $K = K(x)$ and $A = (U/h)dh/dx$, where $U = U_x$. For this case, (4.14) simplifies to

$$\frac{\partial^2 P}{\partial x^2}+\frac{\partial^2 P}{\partial y^2}=-\frac{\mu A}{K}-\frac{1}{K}\frac{\partial P}{\partial x}\frac{dK}{dx}. \tag{4.15}$$

From the analysis in Wu *et al.* (2005a) and Figure 13 in F&W, we know that the pressure distribution in the y direction is parabolic. Thus, one assumes a parabolic pressure profile in the cross sectional plane of a ski or snowboard,

$$P(x,y)=E(x)y^2+F(x)y+P_c(x), \tag{4.16}$$

where $E(x)$, $F(x)$ are unknown functions and $P_c(x)$ is the centerline pressure corresponding to the cross section at the location x. From symmetry, it is evident that $F(x) = 0$ and equation (4.16) can be written as:

$$P(x,y)=E(x)y^2+P_c(x). \tag{4.17}$$

$E(x)$ is determined by applying a simplified boundary condition $P\big|_{y=\pm W/2}=P_0$ at the lateral edges of the ski or snowboard,

$$E(x)=\left[P_0-P_c(x)\right]\frac{4}{W^2}. \tag{4.18}$$

P_0 is very close to the atmospheric pressure since the porosity of the compressed snow changes abruptly at the lateral edges where the compression ends and the hydrodynamic resistance falls precipitously. This approximation greatly simplifies the analysis.

Substituting equations (4.17) and (4.18) into the generalized governing equation (4.15), one obtains

$$\frac{d^2P_c(x)}{dx^2}+\frac{1}{K(x)}\frac{dK(x)}{dx}\frac{dP_c(x)}{dx}-\frac{8}{W^2}\left[P_c(x)-P_0\right]+\frac{\mu A(x)}{K(x)}=0. \tag{4.19}$$

It is desirable to introduce the following dimensionless variables:

$$p'=\frac{P-P_0}{P_0},\quad p_c'=\frac{P_c-P_0}{P_0},\quad x'=\frac{x}{L},\quad y'=\frac{y}{W/2},\quad h'=\frac{h}{h_2},\quad K'=\frac{K}{K_2}.$$

(4.20a, b, c, d, e, f)

Substituting (4.20b, c, e, f) into equation (4.19), we obtain a dimensionless equation for $p_c'(x')$:

$$\frac{d^2p_c'(x')}{dx'^2}+\frac{1}{K'(x')}\frac{dK'(x')}{dx'}\frac{dp_c'(x')}{dx'}-\frac{8}{\varepsilon}p_c'(x')+\frac{\theta_L}{K'(x')h'(x')}=0, \tag{4.21}$$

where

$$\varepsilon=(\frac{W}{L})^2,\quad \theta_L=\frac{\mu}{P_0}(\frac{U}{h_2}\frac{dh}{dx})\frac{L^2}{K_2}. \tag{4.22}$$

At the leading and trailing edge the snow the pressure is close to the atmospheric pressure:

$$p_c'(0)=p_c'(1)=0. \tag{4.23}$$

Equation (4.21) subject to the boundary conditions (4.23) is a non-linear, two-point boundary-value problem which contains two dimensionless parameters, ε and θ_L.

ε denotes the ratio of the square of two characteristic pressure relaxation lengths in the y and x direction. In general, due to the large leakage of air that occurs at the lateral edges, the primary pressure relaxation occurs at these lateral boundaries. One expects a decrease in ε will decrease the pore pressure beneath the planing surface because of the increased lateral air drainage. This is in consistent with the predictions in F&W, where, for $L/W >>1$, the solutions of the generalized Reynolds equation (2-23) in F&W for an elongated planform, such as a ski, differ greatly from the solutions of equation (2-25) in F&W when $L^2/W^2 >> 1$, since the second term in (2-23) is $O(L^2/W^2)$ larger than the first. θ_L in (4.21) is a combination of two dimensionless parameters, $\mu A\big|_{x=L} / P_0$ and L^2/K_2. A scales with the vertical compression velocity of the planing surface. For a given tilt angle, either an increase in the forward velocity U or a decrease in the snow layer thickness at the leading edge h_2 will increase the value of A. It is clear that, this increase of A will increase the pore pressure since a faster compression generates a higher pore air pressure. The inverse of K is a measure of the resistance that the air encounters as it flows through the porous media. One expects that as K_2 decreases the maximum pore pressure will increase since the air will encounter an increased resistance when escaping.

4.2.2.3 $\varepsilon << 1$ (ski)

Equation (4.21) subject to the boundary conditions (4.23) can be solved numerically. However, for $\varepsilon << 1$ a simple asymptotic solution can be obtained that is a good approximation for skiing. For a ski, L = 2 m, W = 0.1 m and $\varepsilon = 2.5\times10^{-3}$. Inspection of (4.21) reveals that:

$$\frac{d^2 p_c'(x')}{dx'^2} \sim \mathrm{O}(1), \quad \frac{1}{K'(x')}\frac{dK'(x')}{dx'}\frac{dp_c'(x')}{dx'} \sim \mathrm{O}(1), \quad \frac{8}{\varepsilon} p_c'(x') \sim \mathrm{O}(800).$$

(4.24a, b, c)

One can rewrite (4.21) as

$$\varepsilon \frac{d^2 p_c'(x')}{dx'^2} + \varepsilon \frac{1}{K'(x')}\frac{dK'(x')}{dx'}\frac{dp_c'(x')}{dx'} - 8p_c'(x') + \frac{\theta_W}{K'(x')h'(x')} = 0, \tag{4.25}$$

where $\theta_W = \left(\mu A|_{x=L} / P_0\right)\cdot\left(W^2 / K_2\right)$. In (4.25) the small dimensionless parameter ε multiplies both the highest derivative term $d^2 p_c'(x')/dx'^2$ and the non-linear term $(1/K'(x'))(dK'(x')/dx')(dp_c'(x')/dx')$. Equation (4.25) is readily solved using singular perturbation methods.

The outer solution of (4.25) is obtained by neglecting the first two terms on the right hand side,

$$p_c'(x')_{outer} = \frac{\theta_W}{8K'(x')h'(x')}. \tag{4.26}$$

Near the trailing edge, $x' = 0$, one expects a sharp increase of pressure in a narrow region of thickness $\mathrm{O}(\varepsilon^{1/2}L)$. Both $K'(x')$ and $dK'(x')/dx'$ remain nearly constant (see Figure 4.2) within this layer and can be approximated by their values at $x' = 0$. Introducing $\sigma = x'/\sqrt{\varepsilon}$, we obtain the inner solution at $x' = 0$ by requiring $\lim_{x'\to 0} p_c'(x')_{outer} = \lim_{\sigma\to\infty} p_c'(\sigma)_{inner,x'=0}$:

$$p_c'(\sigma)_{inner,x'=0} = \frac{\theta_W}{8K'h'|_{x'=0}} - \frac{\theta_W}{8K'h'|_{x'=0}} \exp\left(\frac{-\sqrt{\varepsilon\left(\frac{1}{K'(x')}\frac{dK'(x')}{dx'}\right)_{x'=0}^2 + 32} - \sqrt{\varepsilon}\left(\frac{1}{K'(x')}\frac{dK'(x')}{dx'}\right)_{x'=0}}{2}\sigma \right). \tag{4.27}$$

Similarly, at the leading edge, one introduces $\zeta = (1-x')/\sqrt{\varepsilon}$ to stretch the pressure boundary layer and obtains the inner solution at $x'=1$

$$p_c'(\zeta)_{inner,x'=1} = \frac{\theta_W}{8K'h'\big|_{x'=1}} - \frac{\theta_W}{8K'h'\big|_{x'=1}} \exp\left(\frac{-\sqrt{\varepsilon\left(\frac{1}{K'(x')}\frac{dK'(x')}{dx'}\right)_{x'=1}^2 + 32} + \sqrt{\varepsilon}\left(\frac{1}{K'(x')}\frac{dK'(x')}{dx'}\right)_{x'=1}}{2}\zeta \right). \tag{4.28}$$

Thus the composite solution for the centerline pressure distribution beneath a ski surface is given by

$$p_c'(x')_{composite} = \frac{\theta_W}{8K'(x')h'(x')} - \frac{\theta_W}{8K'h'\big|_{x'=0}} \exp\left(\frac{-\sqrt{\left(\frac{1}{K'(x')}\frac{dK'(x')}{dx'}\right)_{x'=0}^2 + \frac{32}{\varepsilon}} - \left(\frac{1}{K'(x')}\frac{dK'(x')}{dx'}\right)_{x'=0}}{2}x' \right)$$
$$- \frac{\theta_W}{8K'h'\big|_{x'=1}} \exp\left(\frac{-\sqrt{\left(\frac{1}{K'(x')}\frac{dK'(x')}{dx'}\right)_{x'=1}^2 + \frac{32}{\varepsilon}} + \left(\frac{1}{K'(x')}\frac{dK'(x')}{dx'}\right)_{x'=1}}{2}(1-x') \right). \tag{4.29}$$

Once $p_c'(x')$ in (4.21) or (4.29) is determined, one can readily find the two dimensional pressure distributions beneath a snowboard or ski surface by applying (4. 19, 20, 22):

$$p'(x',y') = \left(1-y'^2\right) p_c'(x'). \tag{4.30}$$

The average dimensionless pressure generated by the trapped air inside the compressed snow layer is obtained by integrating (4.30) over the entire surface. This leads to:

$$P_{ava}' = \iint_{ski\ or\ snowboard} p'(x',y')dx'dy' = \frac{2}{3}\int_0^1 p_c'(x')dx'. \qquad (4.31)$$

4.2.3 Lift force from solid phase

The solid phase (ice crystals) lift force is obtained by measuring the quasi-steady force generated when the snow is subject to incrementally increasing compressive forces using the porous cylinder-piston apparatus in Wu, et al (2005b). This solid phase force is given approximately by an empirical relation of the form:

$$\frac{F_{solid}}{F_{\max}} = f\left(\frac{\Delta h}{\Delta h_{\max}}\right) = 0.02396 + 0.4061\left(\frac{\Delta h}{\Delta h_{\max}}\right) + 0.5548\left(\frac{\Delta h}{\Delta h_{\max}}\right)^2, \qquad (4.32)$$

where F_{solid} is the force exerted by the ice crystal phase, Δh is the instantaneous deformation of the snow layer, $\Delta h_{\max}$ is the final displacement of the piston when the full load $F_{\max}$ is supported solely by the ice crystals. In these static experiments, the loading area of the piston cancels out and (4.32) reduces to:

$$\frac{P_{solid}}{P_{\max}} = f(\frac{\Delta h}{\Delta h_{\max}}), \qquad (4.33)$$

In the current study, we shall use (4.33) to predict the pressure from the solid phase during skiing or snowboarding. Consider the case where there is no lateral tilt or edging. The centerline sketch of a ski or snowboard is shown in Figure 4.1b. At any location x, the snow is compressed uniformly and the local pressure from the ice grains is given by (4.33), where $P_{\max} = P_{mg} = mg\cos\alpha_h/LW$, $\Delta h = h_0 - h(x)$, $\Delta h_{max} = h_0 - h_{min}$ and h_{min} corresponds to the thickness of the snow layer where maximum

compression is achieved. P_{mg} is the ice crystal pressure when the pore air pressure vanishes. In Figure 4.3, the skier descends directly down the fall line and the angle of the inclined slope is α_h. Note that for snowboarding, m is the mass of the snowboarder with his/her equipment, while for skiing it is half of this total mass. Equation (4.33) can be written as

$$\frac{P_{solid}(x)}{P_{mg}} = f\left(\frac{1-\frac{h(x)}{h_0}}{1-\frac{h_{\min}}{h_0}}\right). \tag{4.34}$$

The maximum deformation that would be achieved for a given patch of snow corresponds to a density as high as $\rho_{smax} = 0.875\times10^3\ kg/m^3$ (Mellor, 1977; Wu et al., 2005b). Thus, the minimum snow porosity $\phi_{min} = 1-\rho_{smax}/\rho_i = 0.06$, where the ice density, $\rho_i = 0.931\ g/cm^3$. If the undeformed porosity of the snow layer is ϕ_0, $h_{min}/h_0 = (1-\phi_0+\phi_{min})/1 = 1.06-\phi_0$. If one defines $p_s'(x') = P_{solid}(x)/P_0$, one substitutes (4.4) and (4.5) into (4.34) and obtains

$$p_s'(x') = \frac{P_{solid}(x)}{P_0} = f\left(\frac{1-\lambda+\lambda\left(1-\frac{1}{k}\right)x'}{\phi_0-0.06}\right)\frac{P_{mg}}{P_0}. \tag{4.35}$$

where $\lambda = h_2/h_0$. If we define the average pressure generated by the solid phase (ice crystals) as $P_{avs}' = \left((1/L)\int_0^L P_{solid}(x)dx\right)/P_0$, we have

$$P_{avs}' = \frac{P_{mg}}{P_0}\int_0^1 p_s'(x')dx' = \frac{P_{mg}}{P_0}\int_0^1 f\left(\frac{1-\lambda+\lambda\left(1-\frac{1}{k}\right)x'}{\phi_0-0.06}\right)dx'. \tag{4.36}$$

4.2.4 Force balance

To begin discussion of the force balance, we first look at the representative forces acting on a skier gliding on an inclined snow slope. As shown in Figure 4.3, we wish to take moments about the skier's center of mass (CM) including his/her equipment. The weight **mg** may be resolved into two forces, $\mathbf{F}_S$ parallel to the slope, and $\mathbf{F}_N$ normal to the slope. The lift force, which refers to the total reaction force of the snow in the skiing community, Perla and Glenne (1981), is in the present analysis the sum of the distributed forces due to the pore air pressure, $\mathbf{N}_a$, and the ice crystals' reaction force acting on the bottom of the ski, $\mathbf{N}_s$. The skier gliding down the slope has a snow friction force $\mathbf{F}_f$ and a wind resistance or aerodynamic drag force $\mathbf{F}_D$, which are directed up the slope. An aerodynamic lift force $\mathbf{F}_L$ is also present. When a skier has achieved terminal velocity, there is no acceleration and, thus, there is no inertial force, so all the forces as well as the torques shown must sum to zero. In this figure, the forces are shown at the points at which they act. The gravitational force acts at the center of mass. The aerodynamic drag ($\mathbf{F}_D$) acts at the effective center of the frontal area, in line with the center of mass in this case; the snow friction force $\mathbf{F}_f$ acts along the contact area where the ski meets the slope, which is greatly reduced by the presence of μm thick fluid films that form beneath the ski due to frictional heating (Colbeck, 1994). The small tilt angle γ between the bottom surface of the ski or snowboard with the inclined slope is not shown in this figure.

For the normal force balance we require that

$$mg\cos\alpha_h = N_a + N_s, \tag{4.37a}$$

where

$$N_a = \int_0^L \int_{-W/2}^{W/2} (P - P_0)\, dxdy, \quad N_s = \int_0^L P_{solid}(x) W dx, \tag{4.37b, c}$$

and α_h is the angle of the inclined slope. Here we neglect the aerodynamic lift force $\mathbf{F}_L$ since it is small compared with N_a and N_s, Perla and Glenne (1981).

Equation (4.37a) can also be written in the form of an average pressure by dividing each term by $L \cdot W$. If one defines the total dimensionless average pressure arising from both the trapped air and the solid phase as $P_{av}' = \left(P + P_{solid} - P_0\right)/P_0 = P_{ava}' + P_{avs}'$, and the total dimensionless loading pressure exerted by the skier or snowboarder as $P_{avload}' = P_{mg}/P_0$, equation (4.37a) reduces to

$$P_{avload}' = P_{av}' = P_{ava}' + P_{avs}'. \tag{4.38}$$

or equivalently $1 = f_{air} + f_{solid}$, where $f_{air} = P_{ava}'/P_{avload}'$ and $f_{solid} = P_{avs}'/P_{avload}'$.

4.2.5 Moment balance

For the skier or snowboarder moving down the slope with a steady motion, the sum of all torques about the center of mass must be zero. In the case shown in Figure 4.3, the gravitational force (mg), the aerodynamic drag ($\mathbf{F_D}$) and the aerodynamic lift force ($\mathbf{F_L}$) act through the center of mass. Thus, we have

$$N_a(x_c - x_a) + F_f l_c = N_s(x_s - x_c), \tag{4.39}$$

where l_c is the normal distance of the center of gravity from the ski surface, x_c, x_a and x_s are the x coordinates of the center of gravity, center of pore pressure force and center of solid lift force, respectively. Eqn. (4.39) can also be written as

$$x_c' = f_{solid}x_s' + f_{air}x_a' - F_f'l_c', \tag{4.40}$$

where $x_c' = x_c/L$, $x_a' = x_a/L$, $x_s' = x_s/L$, $x_c' = x_c/L$, $l_c' = l_c/L$ and $F_f' = F_f/\text{mgcos}\alpha_h$. The dimensionless x coordinate of the center of pore pressure force, x_a' can be obtained from a moment balance about the trailing edge ($x = 0$)

$$x_a' = \frac{\int_0^L \int_{-W/2}^{W/2} x\left(P - P_0\right)dxdy}{L\int_0^L \int_{-W/2}^{W/2}\left(P - P_0\right)dxdy} = \frac{\int_0^1 x'p_c'(x')dx'}{\int_0^1 p_c'(x')dx'}. \tag{4.41}$$

Similarly, the location of the center of lift force from the solid phase, x_s' is expressed as

$$x_s' = \frac{\int_0^L xP_{solid}(x)Wdx}{L\int_0^L P_{solid}(x)Wdx} = \frac{\int_0^L x'p_s'(x')dx'}{\int_0^L p_s'(x')dx'}. \tag{4.42}$$

The snow frictional force exerted on the ski or snowboard, $\mathbf{F_f}$, is independent of velocity and may be expressed as $F_f = \eta N_s$, where η is the coefficient of friction.

In the current application, we have assumed that the aerodynamic drag $\mathbf{F_D}$ acts at the effective center of the frontal area, in line with the center of mass. Thus, we do not take into account the contribution of $\mathbf{F_D}$ in the moment balance about CM. This is a reasonable assumption because if $\mathbf{F_D}$ deviates from the center of mass, this deviation is much smaller than l_c; on the other hand, the friction coefficient, $\eta < 0.05$. Thus, $\mathbf{F_D}$ is of the same order as $\mathbf{F_f}$ (Lind and Sander, 1996), and $\mathbf{F_D}$'s contribution in the moment balance is negligible.

When a skier or snowboarder glides down a slope at velocity U, over an undeformed snow layer of thickness h_0 and Darcy permeability K_0, the location of the skier's center of mass (CM) is relatively fixed. Thus, one has to adjust the tilt angle γ (or the compression ratio from the leading to trailing edge, $k=h_2/h_1$) as well as the compression ratio at the leading edge, $\lambda = h_2/h_0$, to satisfy the force and moment balance equations, (4.38) and (4.39), respectively.

4.3 Results and discussion

The lift distribution between the trapped air and the ice crystals strongly depends on the geometry of the planing surface, W/L, the speed of the skier or snowboarder, U, and the permeability and compression properties of the snow layer, K_0 and ϕ_0. This is reflected in (4.21) where the pore air pressure generated as the

planing surface glides over the compressed snow layer depends on two dimensionless parameters, ε and θ_L. In this section we shall examine how the lift mechanism depends on these parameters. We shall first look at the case of snowboarding where $L/W = 4.3$ or $\varepsilon = (1/4.3)^2 = 0.054$, a typical value for a 1.16 m long snowboard (see Table 3.5 in Lind and Sanders (1996)). In the case of skiing we use as representative values L =1.7 m, L/W =17 or $\varepsilon = (1/17)^2 = 0.0035$, Lind and Sanders (1996). We consider two typical snow types, wind-packed and fresh snow, and assume the thickness of the fresh undeformed snow layer, h_0 = 10 cm. The mass of the snowboarder with his or her equipment is 80 kg; the angle of the inclined slope α_h = 15°. As mentioned before, the location of the skier's center of mass (CM) is relatively fixed. In our calculations we assume x_c'= 0.45 for snowboarding and x_c'= 0.40 for skiing. The normal distance of the center of gravity from the ski or snowboard surface, l_c = 1 m for snowboarding, and l_c = 80 cm for skiing (Perta and Glenne, 1981). We choose the coefficient of sliding friction, $\eta = 0.04$ (Lind and Sanders, 1996).

4.3.1 Snowboarding

4.3.1.1 Wind-packed snow ($K_0 = 5.0 \times 10^{-10}$ m^2, ϕ_0 =0.6, d = 0.42 mm)

For snowboarding on wind-packed snow with undeformed Darcy permeability $K_0 = 5.0 \times 10^{-10}$ m^2 and undeformed porosity $\phi_0 = 0.6$ (Wu *et al.*, 2005b), we have numerically solved (4.21) subject to boundary conditions (4.23) to obtain the centerline pore pressure distribution beneath a snowboard surface. The results are shown in Figure 4.4a and the values for U, λ, k, x_a', x_s', f_{air} and f_{solid} are summarized in the table below the figure. Here the tilt angle γ (or the compression ratio, $k = h_2/h_1$) as well as the compression ratio at the leading edge, $\lambda = h_2/h_0$ are determined to

satisfy the force and moment balance equations, (4.38) and (4.39), respectively. The dash-dotted line is the prediction of the model when (λ, k) is obtained by requiring that the entire load be supported by the pore air pressure only (f_{air} = 1). It is compared with the case where the lift forces arise from both the trapped air and the solid phase (f_{solid} = 46%) for U = 20 m/s. As can be seen from the table the compression at the leading and trailing edge is significantly reduced and the slope the the snowboard k increased when the solid phase is considered ($h_2/h_0 = \lambda\big|_{f_{air}=0} = 0.58, h_1/h_0 = \lambda/k\big|_{f_{air}=0} = 0.55$, while $h_2/h_0\big|_{f_{air}=46\%} = 0.70, h_1/h_0\big|_{f_{air}=46\%} = 0.65$). It is evident from Figure 4.4a that approximately 50% of the total lift force is generated by the trapped air when one snowboards on a fine-grained, wind-packed snow layer at relatively high speed (U>10 m/s); an increase in velocity leads to an increase in the trapped air's contribution to the total lift and a decrease in the compression of the snow layer (for U = 10 m/s, f_{air} = 43%, h_2/h_0 = 0.65, h_1/h_0=0.60; while for U=20 m/s, f_{air} = 54%, h_2/h_0 = 0.70, h_1/h_0=0.65). We attribute this behavior to the fact that as one increases his/her velocity, the contact time of the planing surface with the snow layer decreases, the air which is trapped inside snow has less time to escape before the pore pressure decays and thus, one only needs a smaller compression to generate the required lift force.

The dimensionless pressure from the solid phase (ice crystals) defined in (4.35), are shown in Figure 4.4b. It is clear from this figure that the solid phase pressure increases nearly linearly from the leading (x'=1) to the trailing edge (x'=0) where maximum compression is achieved; as the velocity increases, f_{air} increases, and, thus the ice crystal's contribution to the total lift decreases.

The predictions shown in Figure 4.4 qualitatively agree with the experimental measurements in Wu *et al.* (2004a and 2005b) for the compression of wind-packed

snow, in their porous walled pistion-cylinder apparatus. Theses experiments suggest that for snowboarding on fine-grained less permeable (wind-packed) snow at velocities greater than 10 m/s, the lift forces generated by the trapped air in the compressed snow layer should provide a significant fraction of the total lift.

4.3.1.2 Fresh snow ($K_0 = 1.7 \times 10^{-8}$ m^2, $\phi_0 = 0.8$, d = 1.0 mm)

Because the Darcy permeability of fresh snow is roughly 34 times larger than the wind-packed snow, air can not be trapped efficiently. At a given speed (e.g. U = 20 m/s), one needs a much larger compression of the fresh snow layer and a larger contribution from the solid phase to generate the required lift, see Figure 5. Figure 5a shows the centerline pore pressure distribution beneath a snowboard surface for the two different snow types. It is clear from this figure that, the trapped air's contribution to the total lift is much larger in the less permeable wind-packed snow than in the highly permeable fresh snow ($f_{air}\big|_{wind-packed\ snow} = 54\%$, $f_{air}\big|_{fresh\ snow} = 18\%$). The values of h/h_0 at both the leading and trailing edge decrease by roughly a factor of two (for fresh snow, h_2/h_0 = 0.38, h_1/h_0=0.31; while for wind-packed snow, h_2/h_0 = 0.70, h_1/h_0=0.65). The maximum compression ratio that can be achieved for a given type of snow is obtained from the expression: $h_1/h_0\big|_{\min} = 1 - \phi_0 + \phi_{\min}$. For fresh snow $h_1/h_0\big|_{\min} = 0.26$, for wind-packed snow $h_1/h_0\big|_{\min} = 0.46$.

Figure 4.5b shows the corresponding solid phase pressure beneath the snowboard surface. Since the trapped air inside fresh snow is not nearly sufficient to support the weight of the snowboarder with his/her equipment, the lift force from the ice crystals carries much of the load ($f_{solid}\big|_{fresh\ snow} = 82\%$). This is in sharp contrast with the case of wind-packed snow where $f_{solid}\big|_{wind-packed\ snow} = 46\%$ at the same

velocity. This behavior was previously predicted in Wu *et al.* (2005b) where the rexation of the pore pressure in the piston-cylinder apparatus was too rapic to support the full weight of the piston when it was dropped from rest.

4.3.2 Skiing

The primary difference in the lift mechanics of snowboarding and skiing is due to the dimensionless parameter ε. The width of a ski is 1/3 of a snowboard and ε for a ski is roughly 1/16 that for a snowboard. Thus, solutions of (4.21) for a long slender planing surface (ski) differ greatly from those for snowboarding. In general, due to the large increase in the pore pressure relaxation at the lateral edges, the required snow compression is larger in skiing than in snowboarding. In Figure 4.6a, we have compared the centerline pore pressure distribution beneath a ski and snowboard for wind-packed snow for a velocity of 20 m/s. As shown in this figure, although the required compression at the leading edge is almost the same, the tilt angle γ of the planing surface (or the compression ratio from the leading to trailing edge, $k = h_2/h_1$) is much larger in skiing than in snowboarding ($k\big|_{skiing} = 1.315,\ k\big|_{snowboarding} = 1.072$), and thus, the snow layer at the trailing edge of the ski is compressed more ($h_1/h_0\big|_{skiing} = 0.54,\ h_1/h_0\big|_{snowboarding} = 0.65$). 42% of the total lift force is generated by the trapped air for skiing on wind-packed snow, which is less than that for snowboarding where f_{air} = 54%. The difference in f_{air} is not great considering the large difference in ε and the pore pressure profiles shown in Figure 4.6a., The skier's center of gravity is closer to the trailing edge ($x_c'\big|_{skiing} = 0.4,\ x_c'\big|_{snowboarding} = 0.45$), and one needs to increase the tilt angle γ to satisfy

the moment balance equation (4.39). By doing so, the center of pore air pressure shifts towards the trailing edge enhancing the pore pressure's contribution to the total lift and compensates in part for the pressure leakage at the lateral edges.

In Figure 4.6b we plot the corresponding solid phase pressure, which clearly demonstrates the significant contribution of the solid phase to the total lift in the case of skiing. Furthermore, due to the larger value of $k=h_2/h_1$, one observes a steeper increase in the local solid phase pressure from the leading to trailing edge for skiing.

Having obtained the centerline pore pressure distribution, we can plot two dimensional pore pressure distributions beneath a snowboard or ski surface using (4.30). The results are shown in Figures 4.7 (a) for snowboarding and (b) for skiing, where the snow is wind-packed, h_0 = 10 cm and U = 20 m/s. This figure shows the effect of the dimensionless parameter, ε. One also notes the parabolic pore pressure distribution in the transverse plane of a ski or snowboard. For skiing, due to the large tilt angle and prevailing continuous drainage in the lateral direction, the pore air pressure increases sharply to its peak value near the trailing edge and then decays rapidly to atmospheric pressure, in contrast to that observed for snowboarding where the axial pressure relaxation at the trailing edge is much more gradual.

4.4 Concluding remarks

In this chapter, we have developed a new theoretical analysis of the lift forces generated during downhill skiing or snowboarding, which incorporates the lift contribution from both the transiently trapped air and the compressed ice crystals. This study is an extension of the classical lubrication theory for highly compressible porous media developed in F&W. The results presented herein agree with the more qualitative predictions in Wu *et al.* (2004a and 2005b) where the pore pressures

generated in snow were measured for the first time using a porous-cylinder-piston apparatus.

The pore air pressure distribution was obtained using a consolidation theory based on Darcy's law where the local change of Darcy permeability of snow was estimated using Shimizu's classical empirical relationship (1970). In our analysis we have neglected the motion of solid particles in the horizontal (x, y) plane and have assumed that the snow is compressed uniformly in the vertical direction. This assumption is appropriate for straight downhill skiing since one leaves a relatively clean track of compressed snow and the motion of the escaping snow at the lateral edges of the skis or snowboard is small compared to that of the escaping air. However, during edging and rapid turning maneuvers one has to consider the motion of the snow powder, and in particular its momentum, in determining the lateral forces, because under these conditions the snowboard or skis also act as a snowplow. The assumption of uniform vertical compression implies that the Darcy permeability K is primarily a function of x. This is reasonable since most skiing conditions involve a fresh snow layer on a packed base, which consists of re-crystallized snow having a permeability that is 20-30 times smaller than fresh snow powder (Jordan, 1999) and the snow with much lower permeability acts as an impermeable base.

The lift force generated by the solid phase (ice crystals) was obtained from the experiments in Wu *et al.* (2005b). These experiments neglect the shear forces produced in the ice crystal structure at the lateral edges of the skis or snowboard. However, studies examining the deformation of the snow at the edge of a compression surface suggest that this force is small compared to the main compression force exerted by the snow directly beneath the planing surface (Shoop and Alger, 1998).

The great enhancement in lift generated by a planing surface as it glides over a soft porous media is a new concept. The application to human skiing or snowboarding was first suggested in F&W. In a more recent study, the authors have applied this idea in the design of a future generation train that can glide on a soft porous track whose mechanical properties are similar to goose down in pillows (Wu *et al.*, 2004a). The key insight in the latter application is that one can greatly enhance the lift and reduce the drag due to friction in the solid phase if the lateral loss of pore pressure at the side walls of the track could be eliminated. If this could be achieved the authors predicted that it would be possible to support a 50 ton train car moving on a porous material with permeability properties that do not differ greatly from fresh snow at velocities > than approximately 10 m/s.

(a)

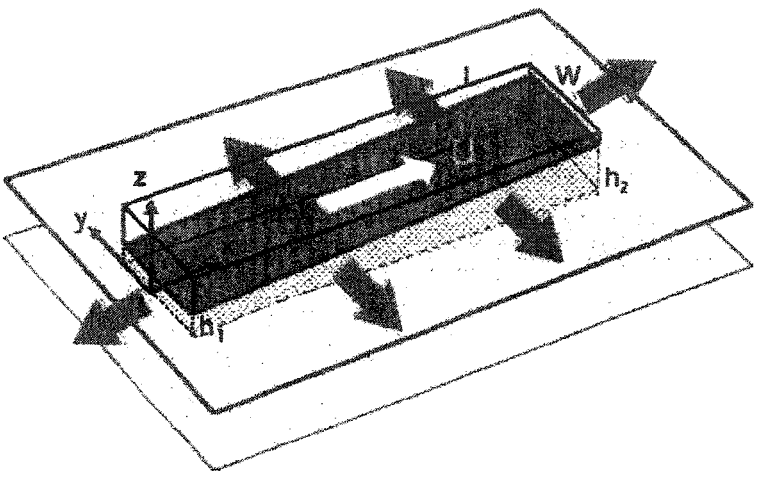

(b)

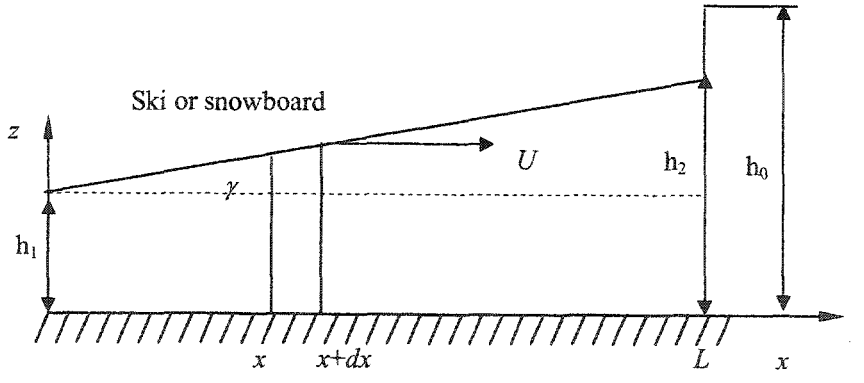

Figure 4.1 (a). Schematic illustration of a snowboard or ski compressing a layer of snow powder. (with permission of F&W). (b). Centerline schematic illustration of a snowboard or ski compressing a snow layer.

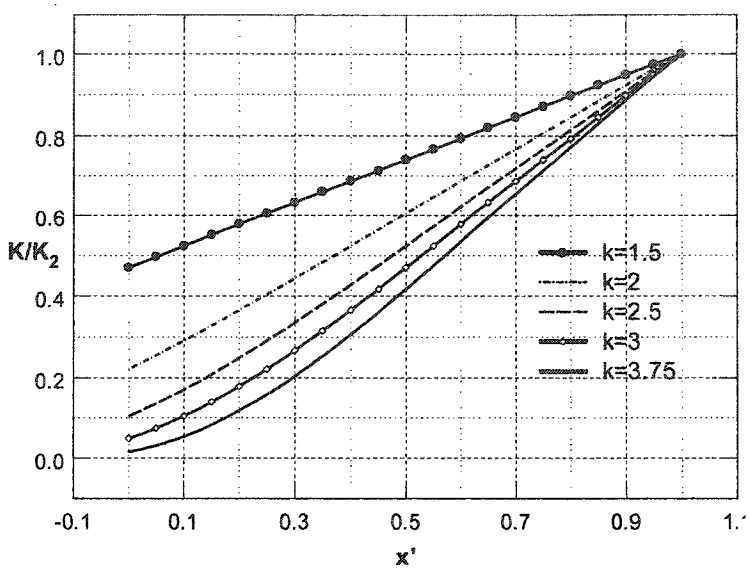

Figure 4.2 Spatial variation of K from leading to trailing edge for different compression ratios, k. The snow layer at the leading edge is undeformed, $h_2 = h_0 = 10$ cm, the diameter of the snow crystal, $d = 0.001$ m and the permeability of the snow beneath the leading edge of the planing surface, $K_2 = K_0 = 1.7 \times 10^{-8}$ m^2 (typical value for fresh snow, Wu *et al.* (2005b).

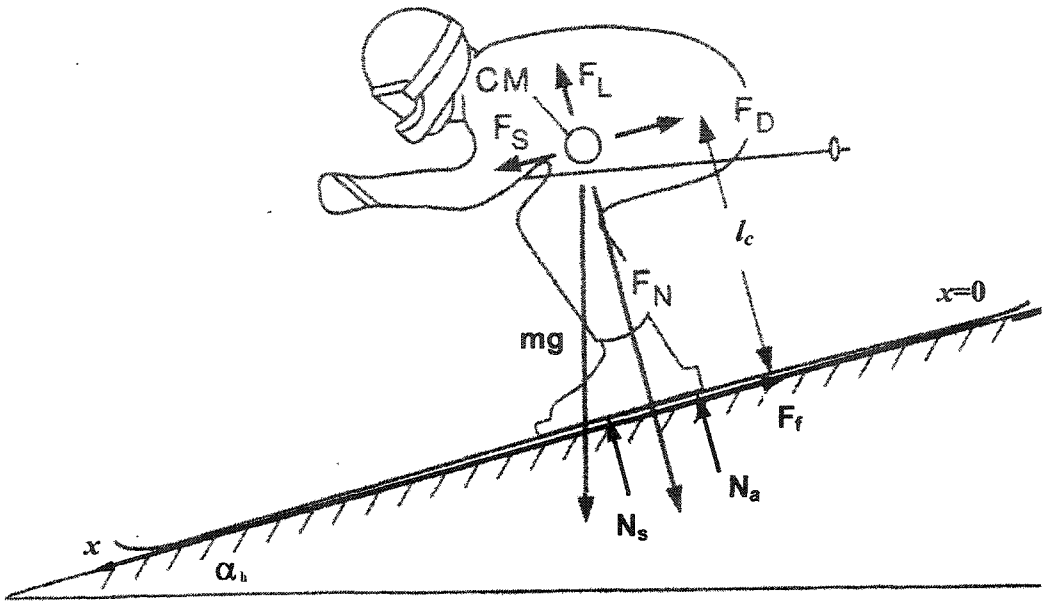

Figure 4.3 A skier descends directly down the fall line. The various forces that act upon the skier in this situation are shown. The weight **mg** is resolved into two forces, $\mathbf{F_S}$ parallel to the slope, and $\mathbf{F_N}$ normal to the slope. $\mathbf{N_a}$ is the lifting force due to the pore air pressure; $\mathbf{N_s}$ is the ice crystals' lifting force. $\mathbf{F_f}$ is the snow friction force; $\mathbf{F_D}$ is the wind resistance or aerodynamic drag force which are directed up the slope. An aerodynamic lift force $\mathbf{F_L}$ is also present. All of the forces are shown at the points at which they act.

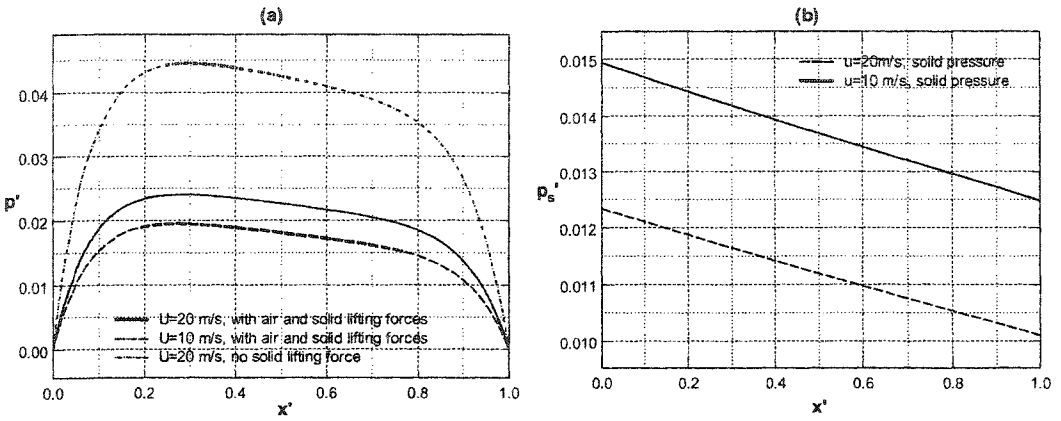

	U (m/s)	λ	k	x_a'	x_s'	f_{air}	f_{solid}
model without solid lift force	20	0.58	1.052	0.479		1	0
model with solid and air lift forces	20	0.7	1.072	0.475	0.483	54%	46%
model with solid and air lift forces	10	0.65	1.078	0.471	0.485	43%	57%

Figure 4.4 (a) Centerline pore pressure (b) solid phase lift pressure distribution beneath a snowboard surface as one glides over 10 cm thick wind-packed snow layer (K_0 =5.0 × 10^{-10} m^2, initial porosity, ϕ_0 = 0.6, the diameter of the snowflake, d = 0.42 mm). The mass of the snowboarder with his/her equipment, m = 80 kg, the angle of the inclined slope, α_h = 15°. The width of the snowboard, W = 0.27 m, the length of the snowboard, L =1.16 m. The results for U, λ, k, x_a', x_s', f_{air} and f_{solid} are listed in the table below the figure.

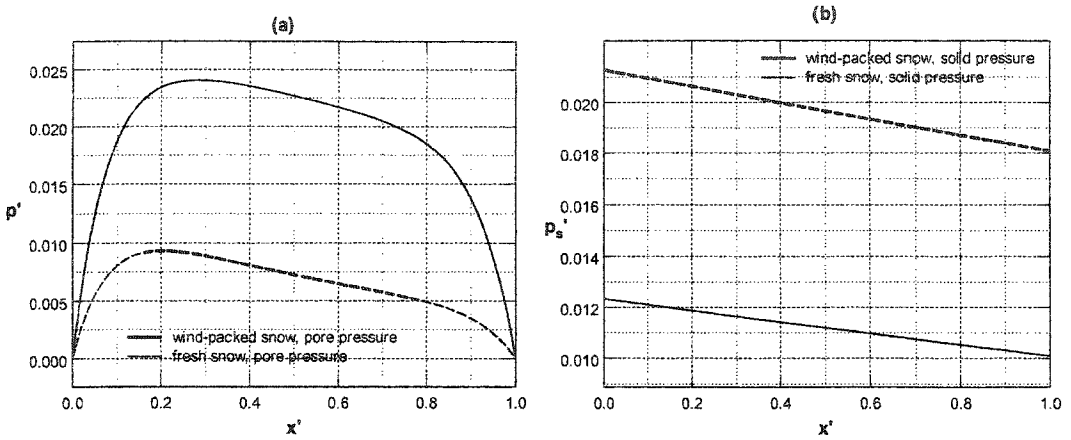

	U (m/s)	λ	k	x_a'	x_s'	f_{air}	f_{solid}
wind-packed snow, snowboard	20	0.70	1.072	0.475	0.483	54%	46%
fresh snow, snowboard	20	0.38	1.230	0.432	0.486	18%	82%

Figure 4.5 (a) Centerline pore pressure (b) solid phase lift pressure distribution beneath a snowboard for two different snow types, wind-packed ($K_0 = 5.0\times10^{-10}$ m^2, $\phi_0 = 0.6$, $d = 0.42$ mm) and fresh snow powder ($K_0 = 1.7\times10^{-8}$ m^2, $\phi_0 = 0.8$, $d = 1.0$ mm). The speed of the snowboarder is chosen as 20 m/s. The mass of the snowboarder with his/her equipment, m = 80 kg, the angle of the inclined slope, α_h = 15°. The width of the snowboard, $W = 0.27$ m, the length of the snowboard, L =1.16 m. The results for U, λ, k, x_a', x_s', f_{air} and f_{solid} are summarized in the table below the figure.

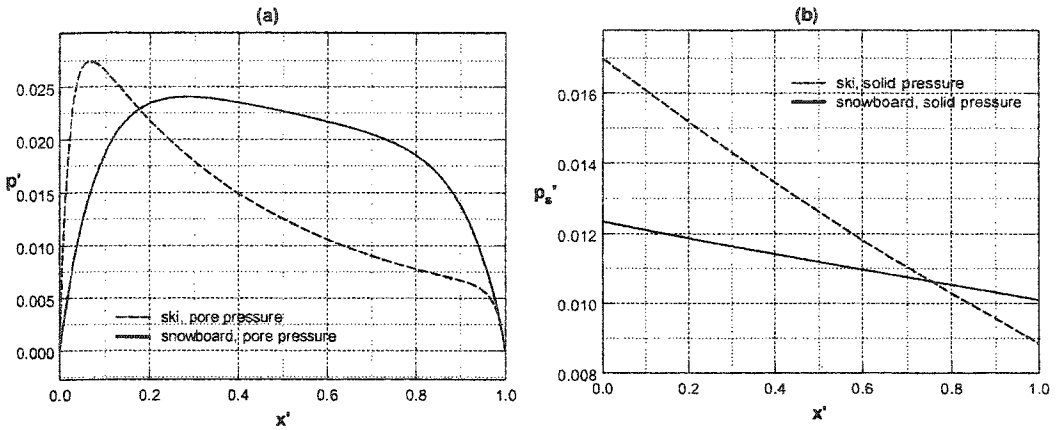

	U (m/s)	λ	k	x_a'	x_s'	f_{air}	f_{solid}
snowboard, wind-packed snow	20	0.70	1.072	0.475	0.483	54%	46%
ski, wind-packed snow	20	0.71	1.315	0.370	0.447	42%	58%

Figure 4.6 (a) Centerline pore pressure (b) solid phase lift pressure distribution beneath a ski or snowboard surface. The speed of the skier, U= 20 m/s, the snow is wind-packed (K_0 =5.0 × 10^{-10} m^2, ϕ_0 = 0.6, d = 0.42 mm) with undeformed thickness, h_0 = 0.1 m. The mass of the skier or nowboarder with his/her equipment, m = 80 kg, the angle of the inclined slope, α_h = 15°. The width of the snowboard, W = 0.27 m, the length of the snowboard, L =1.16 m, the width of the ski, W = 0.10 m, the length of the ski, L = 1.7 m. The results for U, λ, k, x_a', x_s', f_{air} and f_{solid} are summarized in the table below the figure.

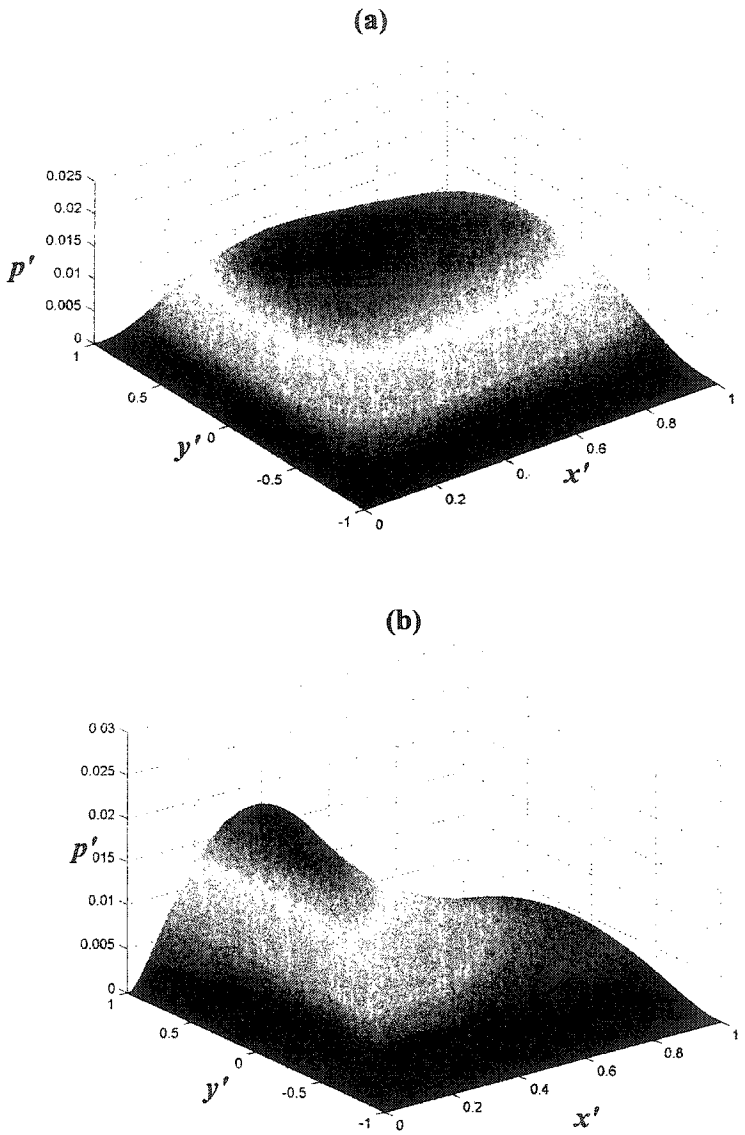

FIGURE 4.7 Theoretical prediction of two-dimensional pressure distribution beneath a (a) snowboard (L =1.16 m, W = 0.27 m) (b) ski (L =1.7 m, W = 0.10 m) surface as one glides over a 10 cm thick wind-packed snow at 20 m/s.

Chapter 5 From red cells to snowboarding to a new concept for a train track

Biological scientists have wondered, since the motion of red cells was first observed in capillaries, how the highly flexible red cell can move with so little friction in tightly fitting microvessels. In 1996, Vink and Duling conclusively demonstrated *in vivo* that our microvessels are lined with a uniform highly compressible endothelial surface layer (ESL), a glycocalyx of glycoproteins and proteoglycans which varies in thickness from 150 nm in frog mesentery capillaries (Squire *et al.*, 2001) to 400 nm in hamster cremaster microvessels (Vink and Duling, 1996). At velocities > 20 μm/s the red cells appeared to glide above the ESL and there was a narrow intervening fluid gap. However, at velocities < 20 μm/s the red cells entered the ESL and when motion was arrested the red cells crushed the glycocalyx and filled nearly the entire lumen of the capillary. In F&W, a generalized lubrication theory is developed to describe the pressure and lift forces generated during this motion. This theory, which applies to one or two-dimensional planar lifting surfaces, shows that the principal difference between a red cell squeezing through a tightly fitting capillary and a human snowboarding is the substantial loss of pore pressure that occurs due to leakage at the lateral edges of the snowboard. The analysis in F&W shows that the behavior is governed by three dimensionless groups, a dimensionless permeability parameter, $\alpha = h/K^{1/2}$, where h is the thickness of the porous layer and K is its Darcy permeability, the slope λ of the planning surface and its length to width ratio L/W. For $\alpha >> 1$, the lift forces increase as α^2 for all λ. The dramatic increase in lift for large α is due to the fact that the fluid is transiently trapped within the soft porous material and cannot escape on the time scale of the motion.

It is well known that sliding friction in skiing on snow is greatly reduced by the presence of μm thick fluid films that form beneath the ski due to frictional heating (Colbeck, 1994). This film greatly reduces friction drag in cross-country skiing much like the thin fluid film that exists between the red cell membrane and the edge of the ESL when the red cell is moving at velocities > 20 μm/s. At velocities < 20 μm/s, the basic mechanism by which the red cell is able to reduce its drag once it enters the glycocalyx is described in Weinbaum *et al.* (2003), where it is shown that the normal force required to compress the core proteins in the glycocalyx is two orders of magnitude smaller than the lift force due to the fluid draining pressure. Since sliding friction over the solid phase is proportional to this force, frictional drag is greatly reduced.

Whereas it would be very difficult to measure the excess pore pressure that develops during red cell motion, an equivalent experiment can be easily performed for snow. To our knowledge, no one has ever attempted to measure the draining pressure that builds up in snow on a time scale characteristic of skiing or snowboarding. There is an extensive literature on the behavior of snow during uniaxial compression (Mellor, 1977; Shapiro *et al.*, 1997), but these studies examine the compression of snow and its creeping behavior on time scales much longer than that of interest herein. In Figure 3.1, we show a novel piston cylinder apparatus with rigimesh sidewalls that will filter snow crystals whose size is greater than 0.120 mm. The mesh is a sintered arrangement of screens with negligible airflow resistance. The piston and a probe mounted on the bottom plate are instrumented with high-frequency, sub-miniature pressure transducers fabricated by Kulite Semiconductor Products. These transducers are able to measure millisecond variations in dynamic pore pressure on the underside of the piston and on the centerline of the cylinder when a weighted piston is dropped

from rest. The diameter of the piston, D_{piston} = 40 cm, is chosen to be representative of the dynamic response that one would encounter while snowboarding. The electrical output is collected with an Iotech 488/8 data acquisition system and finally transferred to a computer to be recorded.

A balance of forces acting on the piston in Figure 3.1 requires that

$$m\frac{d^2h}{dt^2} = -mg + F_{air} + F_{solid}, \tag{5.1}$$

where m is the mass of the piston, h is its instantaneous height, F_{solid} is the force exerted by the solid phase and F_{air} is the integral of the pore air pressure at the piston surface,

$$F_{air}(t) = \int_0^R 2\pi r P(r,h,t)dr. \tag{5.2}$$

The instantaneous flow in the device is approximately described by a quasi-steady axisymmetric flow that satisfies Darcy's law (5.3a) and the continuity equation (5.3b) (Bear, 1972):

$$\mathbf{q} = -\frac{K}{\mu}\nabla P, \quad \nabla\cdot(\rho\mathbf{q}) + \frac{\partial(\rho\varphi)}{\partial t} = 0, \tag{5.3a, b}$$

where μ and ρ are the viscosity and density of the air, respectively, $\mathbf{q}$ is the specific flux vector, and ϕ is the porosity. For axisymmetry and ρ = constant Eqns. (5.3a, b) can be combined to yield a Poisson equation:

$$\frac{1}{r}\frac{\partial}{\partial r}\left(r\frac{\partial P}{\partial r}\right) + \frac{\partial^2 P}{\partial z^2} + \frac{\mu}{K}\frac{h_0(\phi_0 - 1)}{h^2}\frac{dh}{dt} = 0, \tag{5.4}$$

where h_0 and ϕ_0 are the initial thickness and initial porosity of the porous layer, respectively. K is a function of compression and is given by Shimizu's empirical relationship (Shimizu, 1970), $K = 0.077\exp(-0.0078\rho_s)d^2$, where d is the mean diameter of the snow particle and ρ_s is the snow density. The solution of Eqn. (5.4)

satisfying the boundary conditions, $q_z\big|_{z=0}=0, q_z\Big|_{z=h}=\frac{dh}{dt}, \frac{\partial P}{\partial r}\big|_{r=0}=0, P\big|_{r=R}=0,$ is given by

$$P(r,z,t)=\left[\sum_{k=1}^{\infty}\frac{-\frac{\mu}{K}\int_0^R rJ_0(\lambda_k r)dr}{\sinh(\lambda_k h)\lambda_k\int_0^R rJ_0{}^2(\lambda_k r)dr}J_0(\lambda_k r)\cosh\lambda_k z+\frac{\mu(R^2-r^2)}{4K}\frac{h_0(\phi_0-1)}{h^2}\right]\frac{dh}{dt}, \tag{5.5}$$

where λ_k are roots of $J_0(\lambda_k R)=0$. Substituting Eqn. (5.5) into (5.2), one can readily obtain F_{air} (t).

In (5.1), F_{solid} is determined by an independent quasi-static experiment, in which one starts with a light-weight piston, which is typically 1/10 the weight of the heavy piston used in the dynamic experiment, and incremental weights of comparable magnitude are added till one achieves the weight of the piston used in the dynamic experiment. In this experiment, the air in the pores can slowly escape without elevating the pore pressure, in contrast to the dynamic experiments in which the air is temporarily trapped before it escapes. After each incremental weight is added, the compression Δh of the snow layer is measured. This provides an empirical expression for F_{solid}:

$$\frac{F_{solid}}{F_{\max}}=f(\frac{\Delta h}{\Delta h_{\max}}), \tag{5.6}$$

where $F_{\max}= mg$ and $\Delta h_{\max}$ is the final displacement of the piston when the full load mg is applied. Eqn. (5.6) is non-linear for both snow and a material with the properties of goose down, which are considered shortly. When $\Delta h/\Delta h_{\max} < 0.3$, the force exerted by the solid phase is small, whereas when $\Delta h/\Delta h_{\max}$ approaches unity the excess pore pressure has been drained and the solid phase supports the entire load.

Using (5.2), (5.5) and (5.6), one can integrate Eqn. (5.1) subject to initial conditions, $h|_{t=0}=h_0, \frac{dh}{dt}|_{t=0}=0,$ numerically. The solution for $h(t)$ is then substituted into (5.5) to determine the pore pressure distribution.

In Figure 3.5 we have plotted the results for the time dependent variation of the pore pressure at the location of the central pressure transducer on the underside of the piston after it is released from rest. Natural wind-packed soft snow, with an ambient temperature of -10^{o}C was used in this experiment. One observes a rapid rise in pore pressure and then a decay that occurs on a time scale of roughly 0.8 s. The characteristic time to drain the air can be gleaned from a simple drainage model, $t_c = \mu\pi R^2/(8P_cK)$, where $P_c = mg/\pi R^2$. In the current application, one finds that $t_c \approx$ 1 s for $K = 5.0\times10^{-10}$ m^2 and m = 5.9 kg. Since the length of time that a 1.5 m snowboard would be in contact with a given patch of snow if it was travelling at 10 m/s would be 0.15 s, it is clear from the figure that after 0.15 s the excess pore pressure has only started to relax and much of the weight of the snowboarder would be supported by the air that is still trapped in the partially compressed snow layer. The solid curves in Figure 3.5 are our theoretical model predictions for the time dependent decay of the excess pore pressure. One notes that there is one value of the initial Darcy permeability K_0, 5.0×10^{-10} m^2, which provides a best fit to the experimental data.

The behavior just described suggests that it might be possible to support very heavy loads on very soft porous materials, provided the time of passage of the planing surface is small compared to the time that it would take for the confined air or fluid to drain from the porous media beneath it. The calculations in F&W show that the air trapped in snow can easily support the weight of a 70 kg snowboarder when $K_0 < 10^{-8}$

m^2. For a snowboard whose surface area is 0.5 m^2, the pore pressure required is approximately 1/75 of an atmosphere or 1.4 kPa. The slope λ of the snowboard will depend on its velocity U. The feasibility of supporting a 50 ton high speed train car whose planform is 25 m long (L = 25 m) and 2 m wide (W = 2 m) can be gleaned from the fact that the average excess pore pressure required will be 9.8 kPa, or only seven times that of the snow board. This is easily realizable for a porous material whose permeability is of order 10^{-8} m^2 or smaller, provided the loss of pressure through lateral leakage is eliminated. Furthermore, if the deformation of the solid phase is small, that is $\Delta h/\Delta h_{max} << 1$, the load bearing force of the solid phase will be small, and sliding friction greatly reduced. We shall now show that a synthetic material with the mechanical properties of goose down is ideal for these purposes. This material has the additional important advantage that after compression it has a weak restorative force in contrast to snow, which has no elastic recoil.

To measure the dynamic compression properties of goose down, we have used the same porous cylinder apparatus shown in Figure 3.1. These results, which are analogous to those just described for wind-packed snow, are shown in Figure 5.1. One observes again that there is one value of K, 1.6 $\times 10^{-8}$ m^2, which provides a best fit of the experimental data. The principal difference between the curves in Figures 3.5 and 5.1 is that there is no extended relaxation phase for the goose down since the dimensions of the piston are too small and the value of K too large for the excess pore pressure to support most of the piston weight. The maximum pore pressure is only 400 Pa, about half of that needed. However, if $t_c = \mu\pi R^2/(8P_cK)$, the diameter of the piston were 25 m (the length of a train car) and the time to travel this distance 3 s (velocity only 8.3 m/s), the maximum pore pressure would increase to 50 kPa. These

scaling arguments predict that a planform of 25 m length and 2m width would have a maximum possible lift of approximately 250 metric tons for K of order 10^{-8} m^2.

In Figure 5.2, we show a schematic of our proposed lift enhanced, goose down filled train track. The top surface on which the planform glides is a highly flexible porous sheet through which the pore pressure in the porous medium is transmitted. To prevent lateral leakage of pressure the sidewalls of the track are made of an impermeable membrane that is supported by rigid sidewalls. The only significant leakage of pressure occurs at the front and back ends of the planform where the pressure is that of the ambient air. At low speeds, when the velocity of the train car is not sufficient for its weight to be supported by the trapped air in its long slender rectangular shaped goose down pillow, one resorts to wheels. Once the speed has increased to a value sufficient to support the car, the wheels are raised.

The performance of our enhanced lift 50 ton train car is plotted in Figure 5.3, where the track height h_2 at the leading edge is 10 cm. These theoretical predictions are based on the solution of the generalized Reynolds equation (2.25) in F&W, which, in the large α limit, reduces to

$$\frac{d}{dx}\left(-\frac{1}{\alpha^{*2}}\frac{dp}{dx}h\right)=\frac{dh}{dx}, \tag{5.7}$$

where $p = P/\left(\mu LU/h_2^{\,2}\right)$. For each U, the ratio $k = h_2/h_1$ of the leading to trailing edge heights, is determined so as to support the train car weight. K in our experiments in Figure 5.1 is based on goose down from inexpensive pillows with larger more porous feathers. One observes that even for this coarser goose down, where K = 1.6×10^{-8} m^2, h_2/h_1 will be < 1.4 and the slope $\lambda = \tan\beta < 0.001$ if the car velocity is > 10 m/s. Moreover, the performance curves are highly non-linear and at high speeds in excess of 35 m/s there is less than a 10 percent compaction of the track at the trailing

edge. For such small compactions our static compression experiments show that the lift force generated by the solid phase will be < 2% of the lift force due to the pore pressure.

The force diagram in Figure 5.4 provides an overview of the global force balance on the moving train car. In this figure U is the velocity of the train car; N_a and N_s are the normal forces due to air and goose down, respectively; T is the force due to solid sliding friction, $T = \eta \cdot N_s$ where η is the sliding friction coefficient; D is the aerodynamic drag, $D = C_D A \rho U^2/2$; and the mass of the train is m. Using this model we estimate that for U = 50 m/s and $\eta = 0.15$, the force due to sliding friction will be about 1/5 of the aerodynamic drag on a streamlined train car and the pore pressure lift force more than 300 times greater than the sliding friction force and 50 times the total drag. The total drag includes T, D, and the planform drag $(N_a+N_s)\sin\beta$ due to the very small tilt angle β of the planing surface. $N_s\sin\beta$ is negligible and $N_a\sin\beta$ is only 8% of T. Sliding friction can never approach rolling friction where the friction coefficient is only 0.001. However, our objective is simply to reduce sliding friction to a level where it is small compared to other drag forces. With proper design, the new train car should be able negotiate turns with remarkable ease and little sidewall friction. Both sides of the car planform could be arched inwards (concave) to turn in either direction on a curved track of adequate turning radius, unless the planform is able to deform in its own plane. Sidewall friction can be nearly entirely eliminated by having retractable horizontal wheels in the sidewalls near the front and back edges of the planform. These wheels will resist the appreciable centripetal forces that will occur during high-speed turns, and the track must be banked accordingly.

The use of soft porous materials to produce planar lifting surfaces with dramatically enhanced lift and greatly reduced drag is a new concept in lubrication

theory. The application to snowboarding and the design of a futuristic train track were chosen for their novelty, but the basic concepts could have important application in the design of soft porous bearings with greatly increased lubrication pressures and long life. Whereas goose down is an expensive, impractical material, there are many synthetic fiber fill materials with comparable mechanical properties.

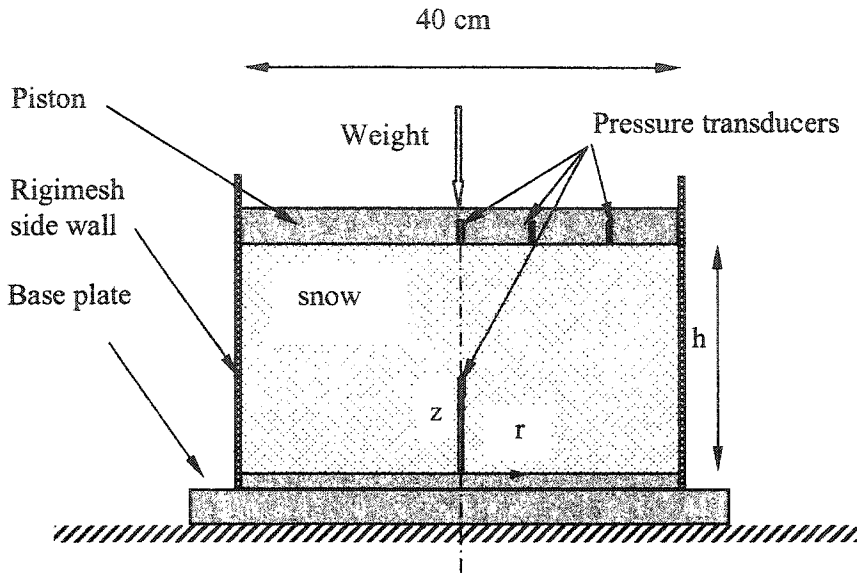

Figure 3.1 Schematic of dynamic snow compression apparatus

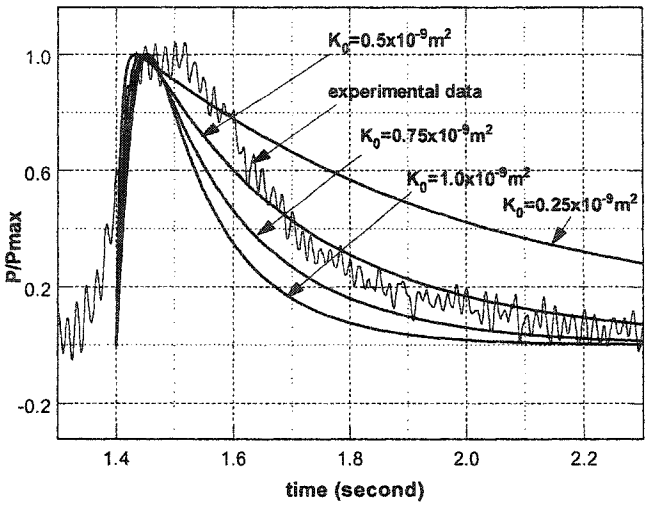

Figure 3.5 Comparison between the theoretical predictions of the time-dependent pressure and the experimental data for various values of the initial Darcy permeability K_0. The test sample was wind-packed snow with initial thickness, h_0 = 11.43 cm, h_f/h_0 = 0.78, applied mass m = 5.9 kg, P_{max} = 744 Pa.

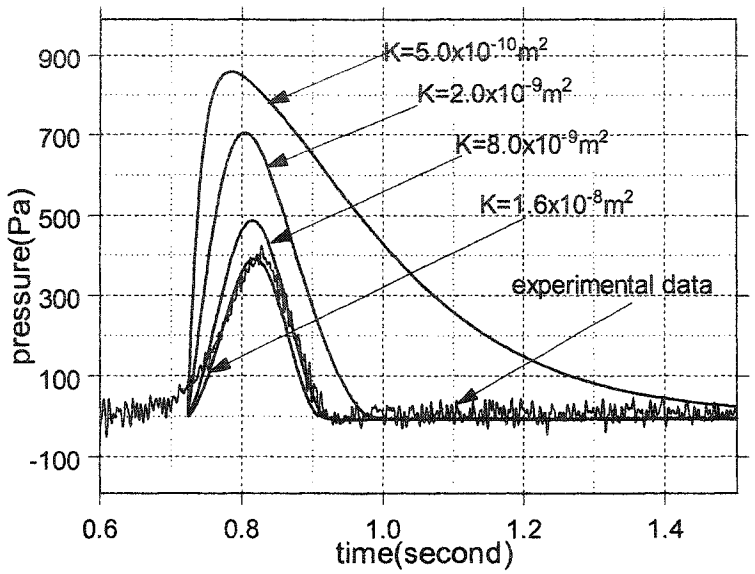

Figure 5.1 Time-dependent pressure at the center of the piston and its comparison with the predictions of Eqn. (5.5) during dynamic compression experiments with goose down, m = 6.4 kg, h_0 = 12.77 cm, $\Delta h_{max}/h_0$ = 0.35, Pmax = 400 Pa.

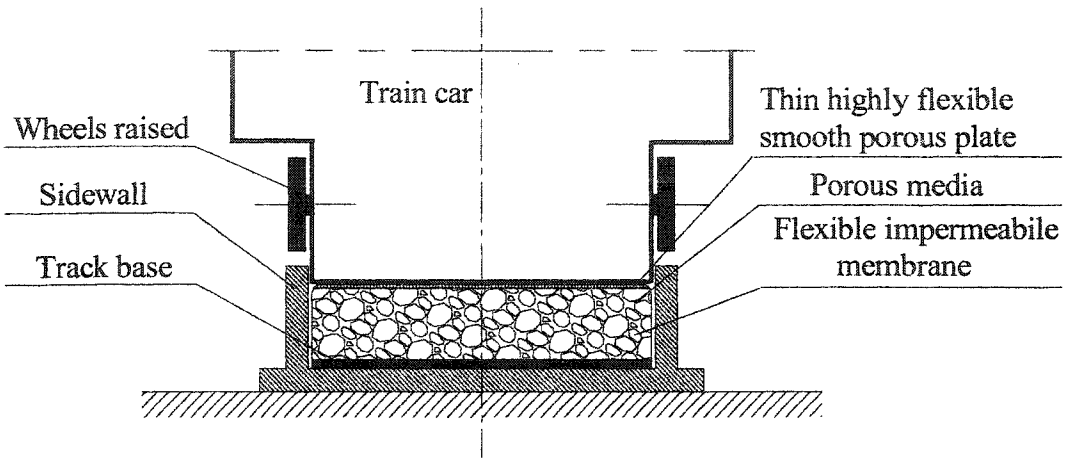

Figure 5.2 Sketch of the new train model in the transverse plane (not to scale).

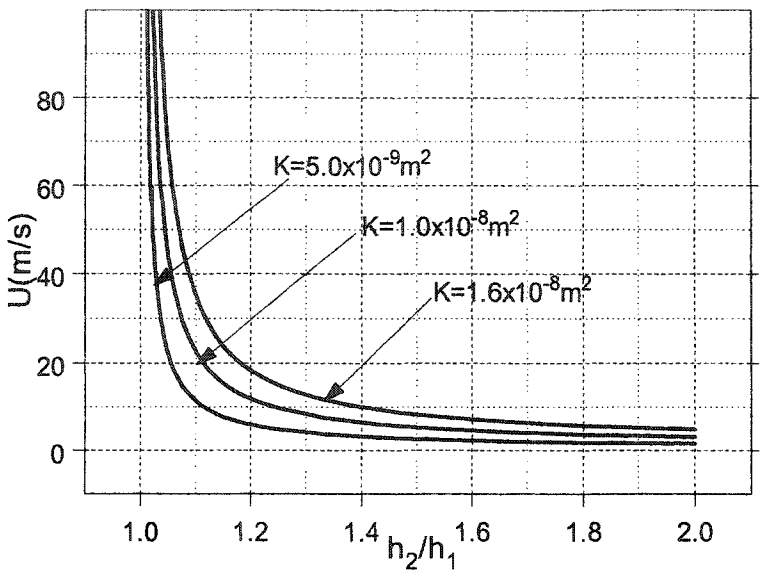

Figure 5.3 The velocity U required to support a train car of 50 metric tons gliding on a porous track as a function of h_2/h_1 for various K. Note that for U > 35 m/s, h_2/h_1 < 1.1. L = 25 m, W = 2 m, and h_2 = 0.10 m.

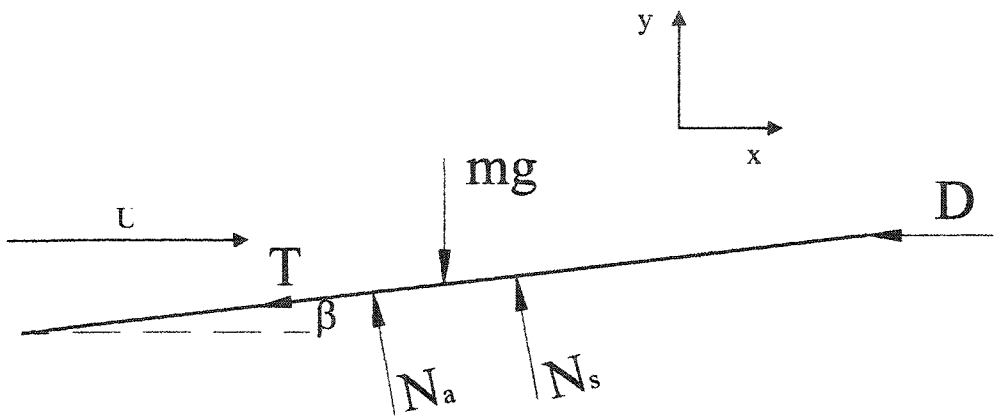

Figure 5.4 Forces on train car. Here U is its velocity; Na and Ns are the normal forces due to air and goose down, respectively; T is the force due to solid sliding friction; and D is the aerodynamic drag.

Chapter 6 Concluding Remarks

The series of studies on lift generation in porous media developed by F&W, Weinbaum *et al* (2003) and Wu *et al.* (2004a, 2004b, 2005a, 2005b and 2005c), have demonstrated theoretically and experimentally the possibility of generating lift forces on soft porous media which vastly exceed those currently available in traditional lubricating films and also dramatically reducing the drag due to sliding friction. These concepts deduced from the motion of red cells in capillaries, are applied in this dissertation to the examination of the inertial effect of the escaping air in the transverse plane of a ski or snowboard; the investigation of the dynamic compression of highly compressible porous media with application to snow compaction; the development of a realistic theoretical model for the lift mechanics of downhill skiing or snowboarding; and the design of a future generation high speed train-track which can support gliding vehicles weighing 50 or more metric tons with extremely low sliding friction gliding on a porous media with mechanical properties akin to goose down.

The fundamental concepts of lift generation in porous media are as follows:

(1) As quantitatively predicted in F&W, lubricating layers formed of soft porous media are able to transiently support planing surfaces with lubricating pressures that increase in magnitude as the square of the dimensionless Brinkman parameter, $\alpha = h/K^{1/2}$, where K is the Darcy permeability and h is the layer thickness. In the case of a red cell moving over an endothelial glycocalyx or a snowboarder gliding over fresh snow powder this parameter is of the order of 100 or greater and, thus, the lift force that can be generated in the absence of lateral leakage is four or more orders of magnitude greater than a lubricating film without the soft porous matrix being present.

(2) A red cell moving in a tightly fitting capillary is far more efficient in producing lift than a human snowboarding since the maximum lift that can be generated falls off as the square of the length to width ratio, $(L/W)^2$, due to lateral leakage at the edges of the snowboard. This is why we use a highly flexible impermeable membrance as the side wall of the pillow-base in our train-track model to avoid lateral pressure loss, Wu et al. (2004a, 2004b).

(3) As quantitatively predicted for the red cell in Weinbaum *et al.* (2003), if the elastic restoring force of the solid phase is small, then sliding friction will be greatly reduced since this frictional force is proportional to the contact force of the fibers in the solid phase. In our train-track model, we try to trap the air inside the porous track so the air provides most of the lift; thus, the sliding friction is greatly reduced, Wu et al. (2004a, 2004b).

(4) Flow in the transverse plane of a ski or snowboard can be viewd, to a first approximation, as a stagnation point flow in a porous media. In the analysis of Chapter 2 (Wu et al., 2005a), a new fundamental dimensionless parameter emerges, $\beta = \upsilon/KA$, where A is the characteristic velocity gradient imposed by the external flow, υ is the kinematic viscosity and K, the Darcy permeability. We have shown that there is a maximum value of β, roughly $\beta = 5$, below which inertial forces need to be considered. For skiing or snowboarding, $\beta >> 5$ and thus the inertial effects are negligible.

(5) The pore pressure generation inside porous media and its relaxation strongly depends on the permeability of the porous media and the characteristic pressure relaxation distance. As predicted in Chapter 3 (Wu et al. 2005b), the characteristic pressure drainage time inside the porous cylinder-piston apparatus is $t_c = \mu\pi R^2/(8P_cK)$, where $P_c = mg/\pi R^2$. The experimental and theoretical study in

Wu et al. (2004a, 2005b) for dynamic compression of highly compressible porous media with application to snow compaction has provided a verification of F&W theory and has laid the foundation for understanding the detailed dynamic response of soft porous layers to rapid deformation.

(6) The new theoretical model for lift mechanics of downhill skiing or snowboarding developed in Chapter 4 (Wu et al, 2005c), combines the lift mechanisms from both the trapped air and the solid phase (ice crystals) and treats the limitations of F&W theory. This new theoretical approach can be applied to other planing surfaces gliding over a porous layer.

(7) The future generation train track model developed in Chapter 5 (Wu et al., 2004a, 2004b) is the outgrowth of the series of studies described herein on lift generation in porous media. The key insight in this study is that one can greatly enhance the lift and reduce the drag due to friction in the solid phase if the lateral loss of pore pressure at the side walls of the track could be eliminated.

For future study, we propose to design and fabricate novel planing surfaces in our laboratory scale train-track model which will seek to maximize the lift and minimize sliding friction drag. We will first examine the mechanical properties of synthetic polyester fiber fill materials that are currently used in pillows as a durable low cost substitute for goose down and examine how these properties vary as a function of compression. Having chosen a suitable synthetic material, we will next explore different designs for the interface between the top of the porous track and the bottom surface of the train. Two basic designs have been chosen for each surface. A schematic of the two designs for our proposed lift enhanced porous track are shown in Figure 6.1. The porous material will be placed within a flexible container of rectangular cross section with impermeable side walls. This pillow-like structure will

have part of its top surface exposed so that the excess pore pressure generated acts on the bottom of the sliding train. To prevent lateral leakage of pressure the side walls of the track are made of a highly flexible impermeable membrane which is supported by rigid side walls. The only significant leakage of pressure occurs at the front and back ends of the planform where the pressure is that of the ambient air.

Currently, two designs are being considered for the top surface of the model track. The first design, shown in Figure 6.1a, has a porous screen with 1cm wide side rails with more rigid cross struts for lateral support. The screen holds the porous material in place while the pressure drop across it is negligible. In the second design shown in Figure 6.1b, a highly flexible perforated Teflon sheet will rest on top of the track cushion. This configuration most probably will allow for a reduced kinetic friction, a decreased loss of pore pressure at the sliding interface and a large reduction in the frictional force, T_{air}, which arises from the air that is dragged through the medium in the interaction layer near the top surface of the track if it is exposed to the gliding planform (A simple approximate expression for this interface resistance can be derived using effective medium theory, $T_{air} = \mu UA/\left(\sqrt{K}\tanh\left(h/\sqrt{K}\right)\right)$. The train car will be a rectangular wooden box, see Figure 6.2, with pressure transducers and other instrumentation capable of moving with speeds in the range of 5 to 20 m/s. The lower surface of the train or planform will be a polished metal or smooth Teflon sheet to minimize sliding friction and avoid pressure leakage. Its leading edge will be bent upwards in the same way that skis are bent. Two designs are also under consideration for the undersurface of the train car. In the design 1 the undersurface will be flat and planar and in design 2, shown in Figure 6.2, a 1 mm deep recessed cavity will be built allowing the excess pore pressure to be distributed more uniformly along the underside of the planform. This latter configuration will allow the train car to function

much like a hover craft where the lifting pressure is provided by the escaping air in the deforming track. Our proposed laboratory scale train-track model will be fully instrumented to measure the transient pore pressure in the soft porous track, the slope of the sliding surface as a function of its velocity and the forces and accelerations on the train. This proposed research work will be the first step in evaluating, identifying and documenting the potentially favorable and possibly extremely rewarding benefits of the largely unknown characteristics of dynamic compression of soft porous media.

For the dynamic compaction experiments with highly compressible porous media, we propose to refine the measurement of the time dependent pore pressure response of initially unpacked porous media to instantaneous loading. The prototype porous cylinder-piston apparatus shown in Chapter 3, in which our dynamic compression experiments were performed, will be further refined by applying an accelerometer on top of the piston surface. This will enable us to measure the displacement and acceleration of the piston as a function of time. Knowing the inertial forces applied on the piston, one could readily determine the effective damping of the solid phase of the porous media using the analysis in Chapter 3. With this information, all of the forces contributing to the dynamic compression process can be determined.

So far, the variation of the Darcy permeability of snow as a function of compression has been based on Shimizu's empirical relationship (1970). In collaboration with Dr. Mary R. Albert at CRREL, we propose to perform more exact and detailed measurements on different porous materials including snow to determine the values of the Darcy permeability. With the input of these measurements into our consolidation model, we will be able to further our understanding of the dynamic response of highly compressible porous media under rapid compaction.

In Chapter 4, we have developed a new theoretical approach to describe the lift mechanics of downhill skiing or snowboarding. To verify this theory, we propose to perform an experimental study on the pressure generation beneath a ski or snowboard. This will include the instrumentation of a ski or a snowboard with pressure transducers and accelerometers, whose electrical output signals will be filtered, amplified, digitized and stored in situ, i.e. within the moving ski or snowbard as one glides down a slope at a certain speed. This will avoid the dragging of cables and wires needed to transfer data between the moving object and a stationary data acquisition station. The results will be compared with the theoretical model developed in Chapter 4.

The use of soft porous materials to produce planar lifting surfaces with dramatically enhanced lift and greatly reduced drag is a new concept in lubrication theory. The application to skiing or snowboarding and the design of a futuristic train track were chosen for their novelty, but the basic concepts could have important applications in the design of soft porous bearings with greatly increased lubrication pressures and long life. Another application of the present study is the development of a new type of journal bearing. Industrial machinery with high horsepower and high loads, such as steam turbines, centrifugal compressors, pumps and motors, utilize journal bearings as rotor supports. One of the basic purposes of a bearing is to provide a nearly frictionless environment to support and guide a rotating shaft. Using insights gained from the analysis of the motion of red cells in tightly fitting capillaries, we propose to develop a theoretical and experimental approach for examining the behavior of soft porous media journal bearings with significantly enhanced lubrication pressures and hence longer life.

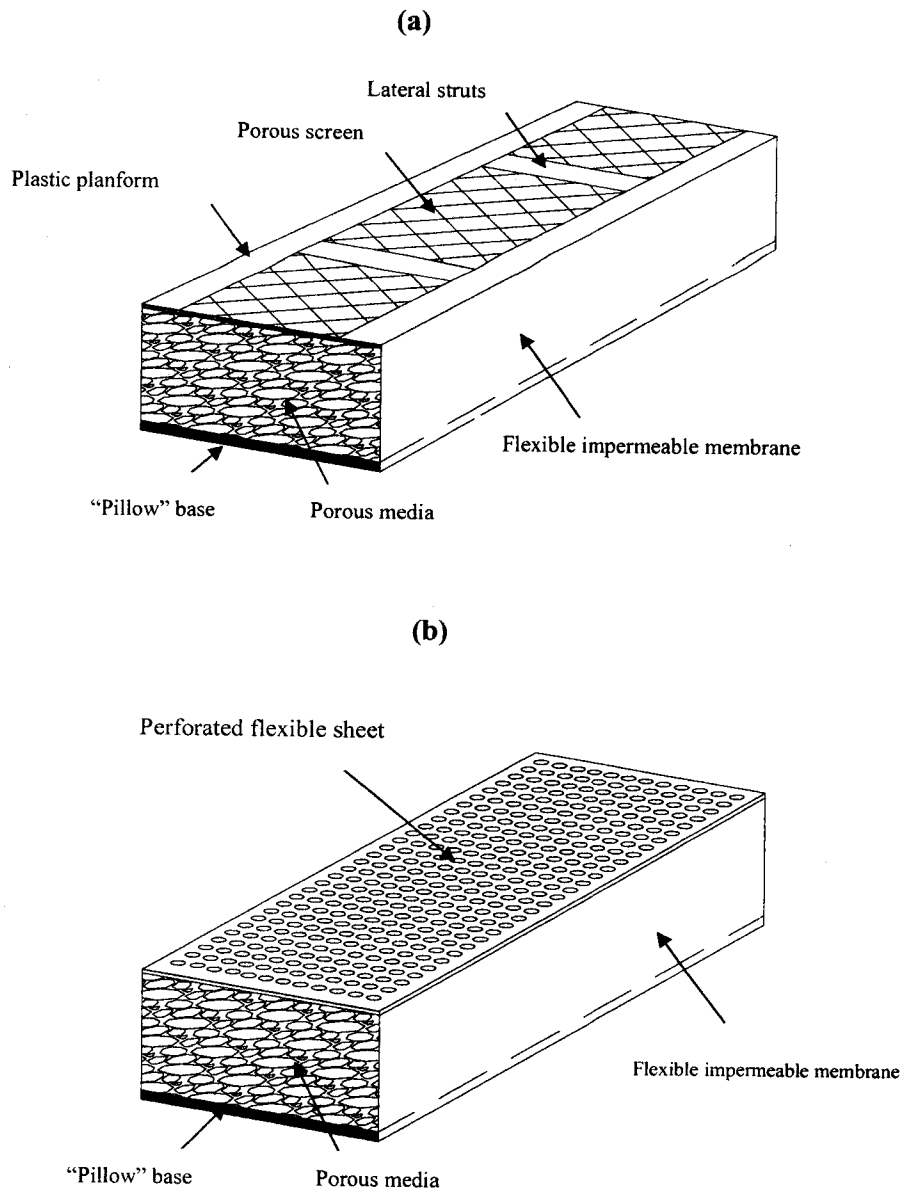

Figure 6.1 Schematic of track design (a) 1 and (b) 2

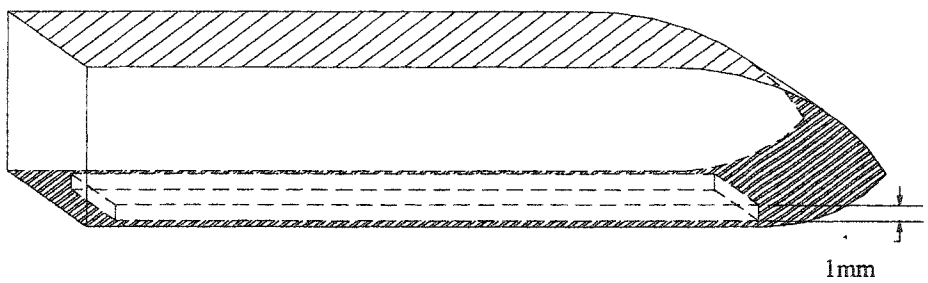

Figure 6.2 Schematic of train car showing design 2 with 1 mm recessed cavity (not to scale).

Bibliography

1. Adamson, R. H. & Clough, G. 1992 Plasma proteins modify the endothelial cell glycocalyx of frog mesenteric microvessels. *J. Physiol. (Lond.)* **445**, 473-486.

2. Adamson, R. H., Lenz, J. F., Zhang, X., Adamson, G. N., Weinbaum, S. & Curry, F. E. 2004 Oncotic pressure opposing filtration across non-fenestrated rat microvessels. *J. Physiol.* **557.3**, 889-907.

3. Albert, D. G. 1993 A comparison between wave propagation in water-saturated and air-saturated porous materials. *J. Appl. Phys.* **73 (1)**, 28-36

4. Albert, M. R., Grannas, A. M., Bottenheim, J., Shepson, P. B. & Perron, F. E. 2002 Processes and properties of snow-air transfer in the high Arctic with application to interstitial ozone at Alert, Canada. *Atmospheric Environment* **36**, 2779-2787.

5. Albert, M. R. & Shultz, E. F. 2002 Snow and firn properties and air-snow transport processes at Summit, Greenland. *Atmospheric Environment* **36**, 2789-2797.

6. Albert, M. R., Shultz, E. F. & Perron, F. E. 2000 Snow and firn permeability at Siple Dome, Antarctica. *Annals of Glaciology* **31**, 353-356.

7. Ambach, W., Mayr, B. 1981 Ski gliding and water film. *Cold Regions Science and Technology*, **5**, 59-65.

8. Arons, E. M. & Colbeck, S. C. 1995 Geometry of heat and mass transfer in dry snow: a review of theory and experiment. *Reviews of Geophysics* **33**, 463-492.

9. Auer, August H. & Veal, Donald L. 1970 The dimensions of ice crystals in natural clouds. *Atmospheric Sciences* **27**, 919-926.

10. Bear, J. 1972 *Dynamics of Fluids in Porous Media*. Elsevier, New York.

11. Beavers, G. C. & Sparrow, E. M. 1969 Non-Darcy flow through fibrous porous media. *J. Appl. Mech.* **36**, 711-714.

12. Biot, M. A. 1941 General theory of three-dimensional consolidation. *J. Appl. Phys.* **12**, 155-164.

13. Biot, M. A. & Willis, D. G. 1957 The elastic coefficients of the theory of consolidation. *J. Appl. Mech.* **24**, 594-601.

14. Brinkmann, H.C. 1947 A calculation of the viscous force exerted by a flowing fluid in a dense swarm of particles. *Appl. Sci. Res.* A **1**, 27.

15. Colbeck, Samuel C. & Warren, G. C. 1991 The thermal response of downhill skis. *Journal of Glaciology* **37(126)**, 228-235.

16. Colbeck, Samuel C., 1992, Review of the processes that control snow friction. *U. S. Army Cold Regions Research and Engineering Laboratory, Monograph* April, 40p.

17. Colbeck, Samuel C. 1994a A review of the friction of snow skis. *Journal of Sports Sciences* **12**, 285-295.

18. Colbeck, Samuel C. 1994b Bottom temperatures of skating ski on snow. *Medicine and Science in sports and exercise* **26(2)**, 258-262.

19. Colbeck, Samuel C. 1995 Electrical charging of skis gliding on snow. *Medicine and Science in sports and exercise* **27(1)**, 136-141.

20. Colbeck, Samuel C. 1996 Capillary bonding of wet surfaces. *Surface and Coating Technology* **81**, 209-214.

21. Curry, F. E. 1986 Determinants of capillary permeability: a review of mechanisms based on single capillary studies in the frog. *Circ. Res.* **59**, 367-380.

22. Damiano, E. R. 1998 The effect of the endothelial-cell glycocalyx on the motion of red blood cells through capillaries. *Microvascular Res.*, **55(1)**, 77-91.

23. Dupuit, J. 1863 *Théoriques et pratiques sur le mouvement des eaux.* Dunod. Paris.

24. Durlofsky, L. & Brady, J. F. 1987 Analysis of the Brinkman equation as a model for flow in porous media. *Phys. Fluids* **30**, 3329.

25. Duva, J. M. & Crow, P. D. 1994 Analysis of consolidation of reinforced materials by power-law creep. *Mech. Mater.* **17 (1)**, 25-32.

26. Fassnacht, S. R., Soulis, E. D. & Kouwen, N. 1999a Shape characteristics of freshly fallen snowflakes and their short-term changes. *Interactions Between the Cryosphere, Climate and Greenhouse Gases (Proceedings of IUGG99 symposium HS2, Birmingham, July 1999)*. IAHS Publ. no. **256**, 111-122.

27. Fassnacht, S. R., Innes, J., Kouwen, N. & Soulis, E. D. 1999b The specific surface area of fresh dendritic snow crystals. *56th Eastern snow conference* Fredericton, New Brunswick, Canada.

28. Feng, J., Ganatos, P. & Weinbaum, S. 1998 Motions of a sphere near planar confining boundaries in a Brinkman medium. *J. Fluid Mech.* **375**, 261-292.

29. Feng, J. & Weinbaum, S. 2000 Lubrication theory in highly compressible porous media: the mechanics of skiing, from red cells to humans. *J. Fluid Mech.* **422**, 282-317.

30. Feng, J., & Weinbaum, S. 2001 Flow through an orifice in a fibrous medium with application to fenestral pores in biological tissue. *Chemical Engineering Science* **56**, 5255-5268.

31. Forchheimer, P. 1901 Wasserbewegung durch Boden. *VDIZ.* **45,** 1782-1788.

32. Gagliardini, O. & Meyssonnier, J. 1997 Flow simulation of a firn-covered cold glacier. *Annals of Glaciology.***24**, 242-248.

33. Gagliardini, O. & Meyssonnier, J. 1999 Analytical derivations for the behavior and fabric evolution of a linear orthotropic ice polycrystal. *Journal of Geophysical Research* **104**, 17,797-17,809.

34. Giver, R.C. & Altobelli, S. A. 1994 A determination of the effective viscosity for the Brinkman-Forchheimer flow model. *J. Fluid Mech.* **258**, 355-370.

35. Guo, P., Weinstein, A. M., & Weinbaum, S. 2000 A hydrodynamic mechanosensory hypothesis for brush border microvilli. *Am J Physiol Renal Physiol.* **Oct; 279(4)**, F698-712.

36. Henry, C. B. & Duling, B. R. 1999 Permeation of the luminal capillary glycocalyx is determined by hyaluronan. *Am. J. Physiol.* **277**, 508-514.

37. Hiemenz, K. 1911 Die Grenzschicht an einem in den gleichförmigen Flüessigkeitsstrom eingetauchten geraden Kreiszylinder. *Dingl. Polytechn. J.* **326,** 321.

38. Hill, Reghan J., Koch, Donald L. & Ladd Anthony J.C., 2001, "The first effects of fluid inertia on flows in ordered and random arrays of spheres", *J. Fluid Mech.* **448**, 213-241.

39. Hill, Reghan J. & Koch, Donald L. 2002 Moderate-Reynolds-number flow in a wall-bounded porous medium. *J. Fluid Mech.* **453**, 315-344.

40. Homann, F. 1936 Der Einfluss grosser Zähigkeit bei der Strömung um den Zylinder und um die Kugel. *Z. Angew. Math. Mech.*, **16** and *Forsch. Gebiete Ingenieurow.* 7(1936) 1; English transl. The Effect of High Viscosity on the Flow around a Cylinder and around a Sphere. *NACA* TM 1334, Washington, D.C. 1952.

41. Howells, I.D. 1974 Drag due to the motion of a Newtonian fluid through a sparse random array of small fixed rigid objects. *J. Fluid Mech.* **64**, 449-475.

42. Howells, I. D. 1998 Drag on fixed beds of fibres in slow flow. *J. Fluid Mech.* **355**, 163-192.

43. Hu, X. & Weinbaum, S. 1999 A new view of Starling's hypothesis at the microstructural level. *Microvascular Res.***58**, 281-304.

44. Hu, X., Adamson, R.H., Liu, B., Curry, F.E., Weinbaum, S. 2000 Starling forces that oppose filtration after tissue oncotic pressure is increased. *Am J. Physiol. Heart Circ. Physiol.* **279**, 1724-1736.

45. Ingham, D. B. & Pop, I. 1998, 2002 *Transport Phenomena in Porous Media.* Oxford, Pergamon.

46. Johnson, J. B. 1982 On the application of Biot's theory to acoustic wave propagation in snow. *Cold Regions Science and Technology*. **6**, 49-60

47. Johnson, Jerome B. 1991 Simple model of shock-wave attenuation in snow. *Journal of Glaciology* **37(127)**, 303-312.

48. Jordan, Rachel E., Hardy, Janet P., Perron, Frank E., Jr & Fisk, David J. 1999 Air permeability and capillary rise as measures of the pore structure of snow: an experimental and theoretical study. *Hydrol. Process*. **13**, 1733-1753.

49. Joseph, D. D., Nield, D. A. & Papanicolaou, G. 1982 Nonlinear equation governing flow in a saturated porous medium. *Water Resources Researc*h. **18(4)**, 1049-1052.

50. Lind, D. & Sanders, S. P. 1996 *The Physics of Skiing –Skiing at The Triple Point*, Woodbury, New York.

51. Luft, J. H. 1966 Fine structure of capillary and endocapillary layer as revealed by ruthenium red. *Microcirc Symp Fed Proc*. **25**, 1773-1783.

52. Lundgren, T. S. 1972 Slow flow through stationary random beds and suspensions of spheres. *J. Fluid Mech*. **51**, 273-299.

53. Macdonald, I. F., Ei-Sayed, M. S., Mow, K. & Dullien, F. A. L. 1979 Flow through porous media: The Ergun equation revisited. *Ind. Chem. Fundam*. **18**, 199-208.

54. Mei, C. C., & Auriault, L. 1991 The effect of weak inertia on flow through a porous medium. *J. Fluid Mech*. **222**, 647-663.

55. Mellor, M. 1964 Properties of snow. *USA Cold Regions Research and Engineering Laboratory, Monograph* **III-A1**.

56. Mellor, M. 1977 Engineering properties of snow. *Journal of Glaciology* **19(81)**, 15-66.

57. Michel, C.C. 1997 Starling: The formulation of his hypothesis of microvascular fluid exchange and its significance after 100 years. *Experimental Physiol*. **82**, 1-30.

58. Nield, D. A., & Bejan, A. (1999). *Convection in porous Media (2nd edition)*. Springer, New York.

59. Ono, A. 1970 Growth mode of ice crystals in natural clouds. *Journal of Atmospheric Sciences* **27**, 649-658.

60. Pang, Z. & Tarbell, J. M. 2003 In vitro study of starling's hypothesis in a cultured monolayer of bovine aortic endothelial cells. *Journal of Vascular Research* **40**, 351-358.

61. Perla, R. & Glenne, B. 1981 "Skiing" in *Handbook of Snow*, edited by Gray, D. M. and Male, D. H., Pergamon, Toronto.

62. Petrenko, V. F. & Whitworth, R. W. 1994 Structure of ordinary ice 1h, II, Defects in ice, Volume 2: Dislocations and plane defects. *U. S. Army Cold Reg. Res. Eng. Lab., Spec. Rep.*, **94(12)**, 1-24.

63. Rott, N. 1955/1956, Unsteady viscous flow in the vicinity of a stagnation point. *Quart. Appl. Math.***13**, 444-451.

64. Saffman, P. G. 1971 On the boundary condition at the surface of porous media. *Stud. Appl. Math.* **1(2)**, 93-101.

65. Sangani, A. S. & Acrivos, A. 1982 Slow flow past periodic arrays of cylinders with application to heat transfer. *Intl. J. Multiphase Flow* **8**, 193-206.

66. Schwartz, J., & Probstein, R. F. 1969 Experimental study of slurry separators for use in desalination. *Desalination* **6**, 239-266.

67. Secomb, T. W., Hsu, R. & Pries, A. R. 1998 A model for red blood cell motion in glycocalyx-lined capillaries. *Am J Physiol.*, **274**, H1016-H1022

68. Shapiro, Lewis H., Johnson, Jerome B., Sturm, Matthew & Blaisdell, G. L. 1997 Snow mechanics Review of the state of knowledge and applications. *USA Cold Regions Research and Engineering Laboratory, Research Report* **97-3**.

69. Shimizu, H. 1970 Air permeability of deposited snow. Institute of Low Temperature Science: Sappora, Japan: Contribution No.**1053**. English Translation.

70. Shoop, S. & Alger, R. 1998 Snow deformation beneath a vertically loaded plate formation of pressure bulb with limited lateral displacement. *International conference on Cold Regions Engineering*, 9th, Duluth, MN, Sep. 27-30, 1998.

71. Squire, J. M., Chew, M., Nneji, G., Neal, C., Barry, J., & Michel C. 2001 Quasi-periodic substructure in the microvessel endothelial glycocalyx: a possible explanation for molecular filtering?. *J Struct Biol.* Dec, **136(3)** 239-255.

72. Starling, E. H., 1896 On the absorption of fluids from the convective tissue spaces. *J. Physiol.* **19**, 312-326.

73. Tada, Shigeru, & Tarbell, John M. 2002 Flow through internal elastic lamina affects shear stress on smooth muscle cells (3D simulations). *Am J Physiol Heart Circ Physiol.* **282**, H576-H584

74. Tam, C. K. W. 1969 The drag on a cloud of spherical particles in low Reynolds number flow. *J. Fluid Mech.* **38**, 537-546.

75. Terzaghi, K. 1943 *Theoretical soil Mechanics*. Wiley, New York.

76. Thi, M. M., Tarbell, J. M., Weinbaum, S. & Spray, D. C. 2004 The role of the glycocalyx in reorganization of the actin cytoskeleton under fluid shear stress: A "bumper-car" model. *Proceedings of National Academy of Sciences.* **101(47)**, 16483-164885.

77. Tsay, R. & Weinbaum, S. 1991 Viscous flow in a channel with periodic cross-bridging fibres: exact solutions and Brinkman approximation. *J. Fluid Mech.* **226**, 125-148.

78. Vafai, K. 2000 *Handbook of Porous Media.* Marcel Dekker, New York.

79. Vink, H. & Duling B. R. 1996 Identification of distinct luminal domains for macromolecules, erythrocytes, and leukocytes within mammalian capillaries. *Circulation Res.* **79**, 581-589.

80. Vink, H., Duling B. R. & Spaan, J. A. E. 1999 *FASEB J.* **13**, A11(abstr.).

81. Wakahama, G. & Sato, A. 1977 Propagation of a plastic wave in snow. *Journal of Glaciology* **19(81)**, 175-183.

82. Wang, W. & Parker, K. H. 1995 The effect of deformable porous surface layers on the motion of a sphere in a narrow cylindrical tube. *J. Fluid Mech.* **283**, 287-305.

83. Weinbaum, S. 1998 1997 Whitaker Distinguished Lecture: models to solve mysteries in biomechanics at the cellular level; a new view of fiber matrix layers. *Ann. Biomedical Eng.* **26**, 1-17.

84. Weinbaum, S. Zhang, X., Han, Y., Vink, H., & Cowin, S.C. 2003, Mechanotransduction and flow across the endothelial glycocalyx. *Proceedings of National Academy of Sciences.* **100(13)**, 7988-7995.

85. Wu, Q., Andreopoulos, Y. & Weinbaum, S. 2004a From red cells to snowboarding: A new concept for a train track. *Physical Review letters* **93(19)**, 194501.

86. Wu, Q., Andreopoulos, Y. & Weinbaum, S. 2004b Lessons learned from the exquisite design of the endothelial surface glycocalyx and their amazing application. *Design and Nature II.* 329-338. WIT press.

87. Wu, Q., Weinbaum, S. & Andreopoulos, Y. 2005a Stagnation point flow in a porous medium. *Chemical Engineering Sciences* **60**, 123-134.

88. Wu, Q., Andreopoulos, Y., Xanthos, S. & Weinbaum, S. 2005b Dynamic compression of highly compressible porous media with application to snow compaction. *Journal of Fluid Mechanics* (accepted for publication).

89. Wu, Q., Igci, Y., Andreopoulos, Y. & Weinbaum, S. 2005c Lift mechanics of downhill skiing and snowboarding. *Journal of Fluid Mechanics* (to be submitted).

90. Yong, R. N. & Fukue, M. 1977 Performance of snow under confined compression. *Journal of Terramechanics*. **14(2)**, 59-82.